Hypersonic Simulations and Analysis of Transition to Turbulence on BoLT-2

A DISSERTATION
SUBMITTED TO THE FACULTY OF THE GRADUATE SCHOOL
OF THE UNIVERSITY OF MINNESOTA
BY

Zachary Michael Johnston

IN PARTIAL FULFILLMENT OF THE REQUIREMENTS
FOR THE DEGREE OF
DOCTOR OF PHILOSOPHY

Graham V. Candler, Adviser

November 2022

Acknowledgements

This work was supported by the Hypersonic Vehicle Simulation Institute (HVSI), the Collaborative Center for Aerospace Sciences (CCAS) and the Air Force Office of Scientific Research (AFOSR) under award number FA9550-21-1-0106. The views and conclusions contained herein are those of the author and should not be interpreted as necessarily representing the official policies or endorsements, either expressed or implied, of the AFOSR or the U.S Government.

I would like to acknowledge John Thome for sharing his experiences regarding simulating the BoLT flowfield and helping me overcome the steep learning curve to perform high fidelity simulations using US3D and discussions related to numerical methods. Also, for sharing a few of his own ideas and subroutines to help me towards reaching my research goals. Many of the results and details discussed in this thesis were sparked from conversations we shared.

Thanks to Dr. Anthony Knutson for his insight related to modifying user subroutines and plugins within the US3D framework. Additionally, for sharing his knowledge with simulating the BoLT flowfield, using adaptive mesh refinement, and discussing ideas related to simulating compressible flow problems to gain a better understanding of the numerical methods introduced in this thesis.

Thanks to Dr. John Reinert for sharing his knowledge related to accessing specific variables within US3D and mentoring that involved applying useful coding practices during my time at the University of Minnesota and during my internship at Johns Hopkins Applied Physics Laboratory.

Thanks to Dr. Joseph Brock for helping me become familiar with mesh generation using Link3D when I first joined the hypersonics lab at the University of Minnesota.

Additionally, for sharing his experience and knowledge related to simulating capsule wake problems using the Free-Flight CFD plugin within US3D during my internship at NASA Ames Research Center.

Thanks to Dr. Heath Johnson for his insight utilizing US3D and sharing advanced user built-in functionality.

Thanks to Dr. Maziar Hemati for invaluable discussions regarding modal analysis techniques along with the interpretation and application when applied to fluid flow data.

Lastly, a special thanks to Dr. Graham Candler for trusting in me throughout my graduate school journey, and providing me with the opportunity to work on a research project that I grew to become passionate about.

Dedication

For my family.

Abstract

The study of laminar to turbulent boundary layer transition has been a flow phenomenon of research for many decades. Recently, there has been interest in understanding how transition occurs for hypersonic boundary layers of increasingly complex geometries. Therefore, the Air Force Research Laboratory/Air Force Office of Scientific Research (AFRL/AFOSR) introduced the Boundary Layer Turbulence (BoLT-2) flight experiment to help in the understanding and prediction of boundary layer transition to turbulence at high-speeds by collecting data in flight. The BoLT-2 research geometry allows for the existence of multiple instabilities to coexist and potentially interact thus leading to transition. This allows for the opportunity to assess current stability analysis tools and numerical methods to help improve prediction of thermal loading under flight conditions. In support of this task, the objective of this dissertation is to quantify transition mechanisms contributing to nonlinear breakdown using a forced DNS approach. Modal analysis techniques are applied to simulation datasets to extract pertinent information associated with dominant instabilities contributing to breakdown. This is meant to help in the understanding of the underlying flow physics contributing to breakdown on BoLT-2. Comparisons are made with experiments conducted in the Mach 6 Quiet Tunnel (M6QT) at Texas A & M University and show excellent agreement. Furthermore, flight conditions are investigated to identify instabilities that are potentially present at flight conditions. This is meant to help with the interpretation of flight data once it becomes available to the research community. The numerical methodology of the DNS approach presented in this dissertation is one that can be used to predict transition and help towards the development of multi-dimensional stability analysis methods for transition prediction.

Contents

List of Tables

List of Figures

Chapter 1

Introduction

1.0.1 Hypersonic Vehicle Design Challenges

High speed vehicles for aerospace applications have become increasingly popular in recent years. The demand for hypersonic aerospace applications comes from the desire to send and/or return vehicles to orbit, faster means of atmospheric travel, and rapid military response. Hypersonic vehicles (i.e. air-breathing hypersonic aircraft, rocket-based launch vehicles, boost-glide vehicles, re-entry capsules, ballistic missiles, etc.) face difficult design challenges. A few of the design constraints may include optimizing reliability, re-usability, costs, and functionality for the desired application. More importantly, the start of a feasible design requires the need for accurate physics-based models and high-fidelity numerical methods to predict the operation of hypersonic flight vehicles since a balance between aerodynamics and aeroheating dictates proper functionality. Although the hypersonic flow regime is often reported to occur for vehicles flying at a freestream Mach number of about five, the hypersonic flow regime is governed by the physical flow phenomena which may exist at slightly lower Mach numbers. A few examples of the flow phenomena at hypersonic conditions for different design problems are shown in Figure 1.1. The schematics illustrate that the hypersonic flow around vehicles at different operating conditions are characterized by compressible flow phenomena which may include but are not

limited to [1, 2]: shock waves, boundary layer transition, shock-shock interactions, shock-boundary layer interactions, chemical kinetics, thermal non-equilibrium effects, vibrational and/or electronic excitation, surface catalysis, or ablation which causes surface recession. Regardless of the application, surface heating is a fundamental problem that constrains hypersonic vehicle design and can have varying amounts of effects induced by the physical phenomena present.

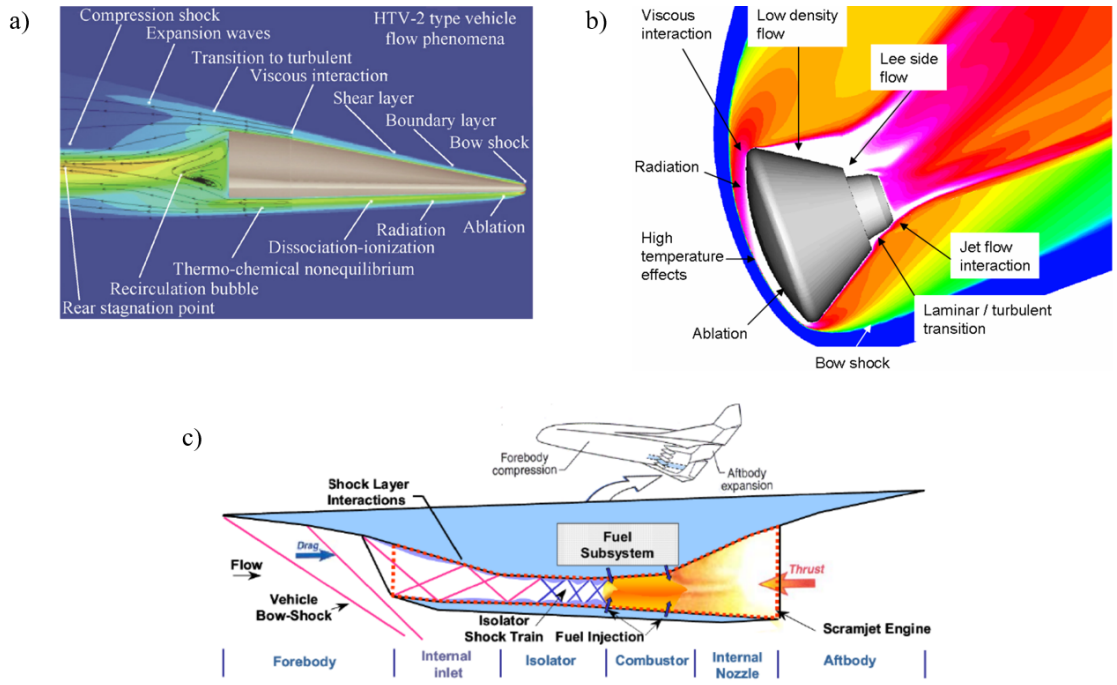

Figure 1.1: Hypersonic flow phenomena of: a) Boost-Glide Vehicle (BGV) operating at a single condition along the glide phase of the trajectory [3], b) atmospheric entry capsule [4], and c) scramjet engine and intake port structure [5].

In order to handle the large surface heat loads, a suitable Thermal Protection System (TPS) is required. The peak heat transfer rates are often governed by the flow characteristics of the boundary layer - the region at which large viscous stresses augment the flow state close to the vehicle. This requires an understanding of the underlying flow physics in high speed compressible boundary layers in order to properly model and obtain accurate heating predictions in the presence of boundary layer tran-

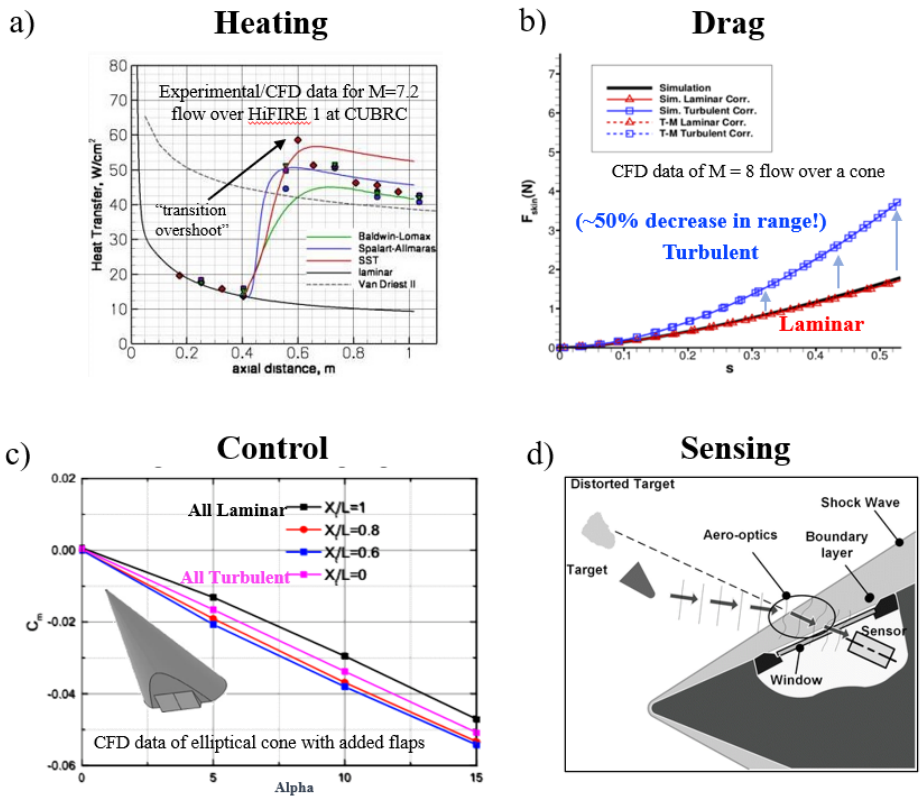

Figure 1.2: Impacts of boundary layer transition on hypersonic vehicle design parameters.

sition. Even though flow transition has been studied for many decades, it continues to be a flow phenomenon that has not been fully understood making it a difficult task to properly simulate using computational fluid dynamics (CFD). This is due to the fact that transition mechanisms can support and amplify external disturbances leading to laminar-turbulent transition in many different ways. This can have a direct impact on surface skin friction and aerodynamic heating thus affecting hypersonic vehicle performance. For some flow configurations, turbulent heat transfer rates can reach triple to almost an order of magnitude greater thermal loading than laminar heat transfer rates. Figure 1.2a) shows a surface heating comparison of a straight cone geometry at Mach 7.2. By comparison, experimental data and solutions obtained

with turbulence models using CFD show over a 3 times higher increase in turbulent heat transfer rates compared to the laminar heat transfer rate estimate. Therefore, boundary layer transition studies are often motivated by optimizing thermal protection systems and obtaining accurate heat transfer rates. Furthermore, vehicle skin friction can drastically increase in the event that a boundary layer transitions. This is shown in Figure 1.2b) which illustrates increased drag of a cone configuration at Mach 8. The increased drag can cause as much as a 50% reduction in range due to drag forces obtained from simulation. As a consequence, this can make it difficult to maneuver a vehicle along a desired trajectory due to uncertainty in control effectiveness and have a large impact on vehicle dynamics as seen in Figure 1.2c). This example illustrates drastic differences in pitching moment coefficients versus flap deflection angle due to maneuvering. The changes in pitch moment are a result of the flap angle having a transitional boundary layer.

Another problem that a boundary layer may cause is when the surrounding flowfield fluctuations can lead to strong variations in light refraction. This can make it difficult for tracking vehicles at which the vehicle position may appear distorted. Therefore, it is important for designers to be able to properly model and predict when and where the boundary layer may transition in flight, along with the physical understanding at various operating conditions. This can be directly related to the trajectory which must be optimized for efficiency. In the case that aerodynamic forces are used to slow the vehicle upon re-entry, it is essential that safe thermal stresses are maintained below the peak heating of the TPS. Examples of variable peak heating at different flight conditions have been observed from past space shuttle flights where surface temperature histories show laminar-turbulent heating at different points in the trajectory [6, 7]. Therefore, the optimization and design of hypersonic vehicles has to balance aerothermal and aerodynamic needs, and the state of the boundary layer is typically one aspect which governs the design process. This motivates the cur-

rent work which involves developing a Direct Numerical Simulation (DNS) approach that can be used to address the performance of current stability analysis tools used in practice. Also, the methodology can be used to help develop physics-based modeling approaches for a wide variety of problems and verify the applications to realistic flow configurations.

1.0.2 Introduction to Boundary Layer Transition of High Speed Flows

Boundary layer transition at hypersonic speeds is a complicated total process, and continues to be a major unresolved problem in fluid mechanics and engineering despite many decades of dedicated research. The phenomenon of laminar to turbulent transition at high speeds is illustrated in Figure 1.3 showing a ballistic cone travelling at Mach 4. Physically, the disturbance environment dictates the spatial location of

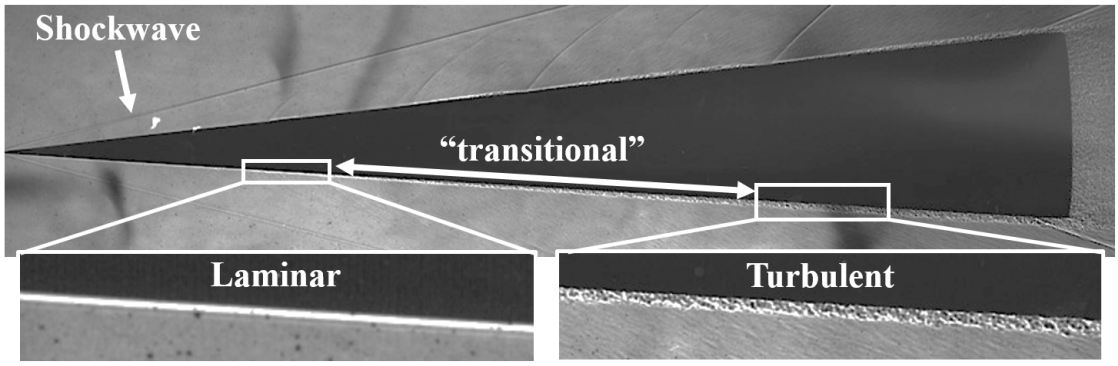

Figure 1.3: Laminar-turbulent transition on ballistic slender cone at Mach 4 [8].

the early stages of transition. The disturbance environment in ground test facilities is often unknown which results in having low confidence for predicting transition that is representative of flight. Therefore, it is essential that analysis techniques are developed to provide a physical understanding of transition processes to account for experimental uncertainties in estimating transition onset. Numerically, this requires

that simulation techniques and realistic boundary conditions are applied to make accurate predictions for flight. Typically, the transition process is often modeled by analyzing growth of perturbations relative to a laminar flow state for quantifying disturbance amplification. In the past, transition prediction and analysis has focused on identifying boundary layer instabilities and quantifying local disturbance amplification for canonical geometries (e.g. flat plates, wedges, and cones). These studies have provided a fundamental understanding of transition mechanisms in hypersonic boundary layers. This is valuable for academic research since the problems are generally more manageable in terms of grid sizes, data collection, simulation modeling, and analysis techniques. Additionally, the problems can be easily reproduced and compared between academic researchers thus allowing numerical methodologies to be verified. However, many tools developed based on simple, canonical test cases under ideal flow conditions do not always scale when applied to actual design problems. Also, the general framework is sometimes no longer useful when applied to realistic flight geometries and/or flow conditions which is the claimed end goal of many researchers performing transition studies. This is due to the fact that most boundary layer stability analysis typically assumes two-dimensional or at most axi-symmetric flow configurations which is not always the case for realistic flight configurations. Furthermore, vehicles that are actually flown inherently experience three-dimensional flow effects such as a dispersion in pitch, yaw, and roll. In addition to this, the transition process is inherently nonlinear. This means that the flow state can evolve to the point where assumptions made by traditional stability analysis tools are no longer valid. As a result, recent boundary layer transition flight experiments have been carried out to address predictive capabilities with current boundary layer stability analysis tools.

Over the past decade, the Air Force Office of Scientific Research (AFOSR) have been performing a series of hypersonic flight experiments to quantify flight data for in-

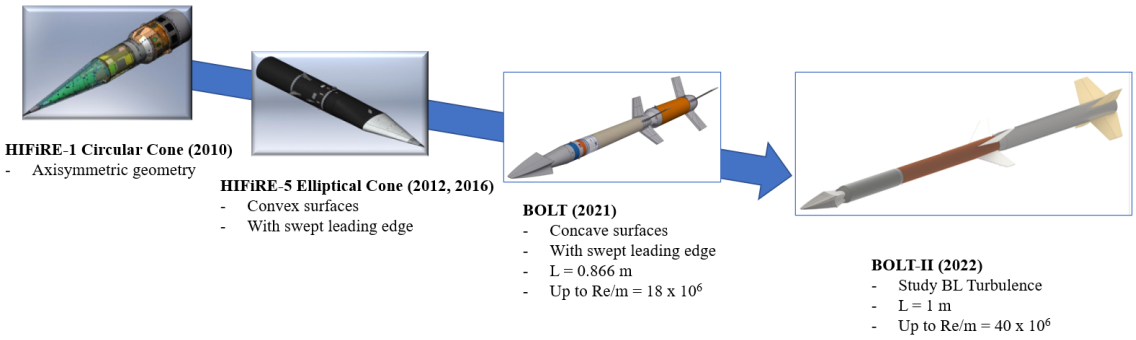

Figure 1.4: Air Force Office of Scientific Research (AFOSR) hypersonic boundary layer transition flight experiments.

creasingly complex nose cone geometries of sounding rockets for high speed boundary layer transition studies. The first flight experiment was the HIFiRE-1 flight experiment which contained an axi-symmetric blunt cone shape and was flown in 2010. The second was the HIFiRE-5 flight experiment that was flown in 2012 & 2016, and contained a 2:1 elliptic cone with convex surfaces. The third flight experiment was the Boundary Layer Turbulence (BoLT) flight experiment [9] involving a nose cone geometry characterized by highly swept leading edges joined by concave surfaces. The most recent experiment is the Boundary Layer Turbulence (BoLT-2) flight experiment which is an extension of the original BoLT geometry to promote the study of boundary layer turbulence. Therefore, the purpose of this work is to characterize three-dimensional boundary layer instabilities and secondary flow behavior of the BoLT-2 boundary layer through the stages of nonlinear breakdown. Also, to elucidate on the need to assess current simulation and analysis techniques on more realistic flow configurations for accurate transition and turbulence predictions. This is achieved by simulating the flow state and quantifying heat transfer rates imposed by the boundary layer instabilities which is essential for obtaining accurate aerothermal heating estimates.

1.0.3 BoLT-2 Experimental Overview

The Boundary-Layer Transition (BoLT) flight experiment has proven to be successful in testing and developing stability analysis tools using numerical simulation [10, 11] and comparisons are consistent with experimental ground test measurements [12, 13]. Therefore, the Boundary Layer Turbulence (BoLT-2) flight experiment is the next hypersonic flight experiment and was flown in March of 2022. The research geometry of interest is referred to as BoLT-2 and is a nose cone of the sounding rocket. The goal of the sounding rocket flight test is to collect measurements to characterize boundary layer transition and turbulent flow quantities at hypersonic flight conditions of the BoLT-2 research geometry. This is meant to help further test, develop, and verify stability analysis tools through boundary layer breakdown using state-of-the-art computational analyses and ground tests to study transition to turbulence. The geometry contains four swept edges that are meant to isolate regions for individual research studies including natural transition on the primary (top) surface and boundary layer trips on the secondary (bottom) surface [14].

The motivation of the Boundary Layer Turbulence (BoLT-2) flight experiment comes from the desire to improve flight predictions for hypersonic vehicles by documenting surface quantifies of a fully turbulent boundary layer at flight conditions. The purpose of this is to use the flight data for improving transition prediction and turbulence modeling. The objective of the BoLT-2 flight experiment is to make measurements in flight and add to the experimental database by collecting surface quantities induced by the off-surface flow structures. Therefore, this presents an opportunity to assess and develop numerical analysis tools to understand how the thermal transport is altered by nonlinear flow behavior. A comparison to data collection will address quantifying time-varying and non-uniform boundary conditions since flight times extend for a longer duration than most ground test facilities.

In this work, multiple versions of the BoLT-2 geometry introduced by [15] are

considered. The geometries of interest are the a 25% subscale version of the original 1.5 m (1.477 m) BoLT-2 geometry and the full scale flight geometry which has a length of 1.0 m. The simulation data is compared with experimental measurements collected in the Mach 6 Quiet Tunnel (M6QT) at Texas A&M University. Due to scaling and freestream conditions, the Reynolds numbers from of the tunnel are low compared to when transition is expected to occur in flight. For this reason, the flight geometry was originally the 1.477 m length but was truncated to 1 m for flight in order to satisfy flight stability of the rocket configuration. A scaled version of the long BoLT-2 geometry is where the majority of the measurements were taken in the M6QT due to the difficulty in observing transition to turbulence for the model sizes that can fit within the tunnel. Nonetheless, invaluable experimental measurements were made which can be used for comparison to simulation for analysis for verification of the numerical approach. More importantly, the low noise environmental of quiet wind tunnels provides a better representation of atmospheric flight than conventional wind tunnels. This is essential since transition is significantly affected by the forcing function and initial disturbance amplitude for accurate transition prediction. Results from Kostak-Teplicek [15] have provided useful insight into the state of the boundary layer with the help of high resolution infrared thermography of the wall temperature. Furthermore, high frequency pressure transducer measurements on the surface were used to identify frequencies which are amplified by instabilities. The idea is that the higher amplitude surface perturbations have frequencies attributed to boundary layer instabilities. Since the flow state is three-dimensional, a poor choice of spatial location may not record frequencies induced by relevant boundary layer instabilities. Because of this, non-intrusive measurement techniques were used to measure flow quantities off the wall including mass flux and velocity fluctuations. This is meant to confirm the existence of flowfield fluctuations induced by instabilities contributing to boundary layer breakdown which are observed in numerical simulations as well. This

is important for verification since multiple types of unstable boundary layer modes exist, and it should not be assumed that transition is a result of a single unstable mode.

Genesis of the BoLT-2 Geometry

The intent of the BoLT-2 experiment was inspired by the BoLT experiment derived from the original BoLT geometry. The first BoLT concept was generated by the University of Minnesota (UMN) team in late 2016 in collaboration with a government-led team including researchers from AFOSR, AFRL, CUBRC, Purdue University, Texas A&M University, NASA Langley, and Johns Hopkins Applied Physics Laboratory. The initial concepts proved to have a significant amount of flow separation and shock boundary layer interaction phenomena which contributed to extreme heating. This included serious concerns related to manufacturing and unsteady aerodynamic loading. The BoLT geometry concepts are depicted in Figure 1.5.

Further modifications were made by the University of Minnesota (UMN) team to address a few of the underlying issues. While doing so, the Air Force Research Laboratory (AFRL) developed a competing geometry to help fulfill design objectives. Nonetheless, the same issues constraining the UMN concepts were present on the AFRL concept. The team collaborated and resorted to combining two competing concepts by incorporating concave surfaces with a cylindrical leading edge nose tip. The UMN team produced preliminary CFD calculations to ensure desirable features were present for the 5th concept but the geometry did not meet the size or payload requirements for the sounding rocket. Therefore, the geometry was elongated in the axial direction to 0.866 m; the same length as the HIFiRE-5 research geometry. The key geometry features included a cylindrical nose tip (5 mm) with four swept leading edges joined by concave surfaces. The surfaces of interest were the upper and lower concave surfaces. Also, note that the side surfaces (often referred to as the "gutter")

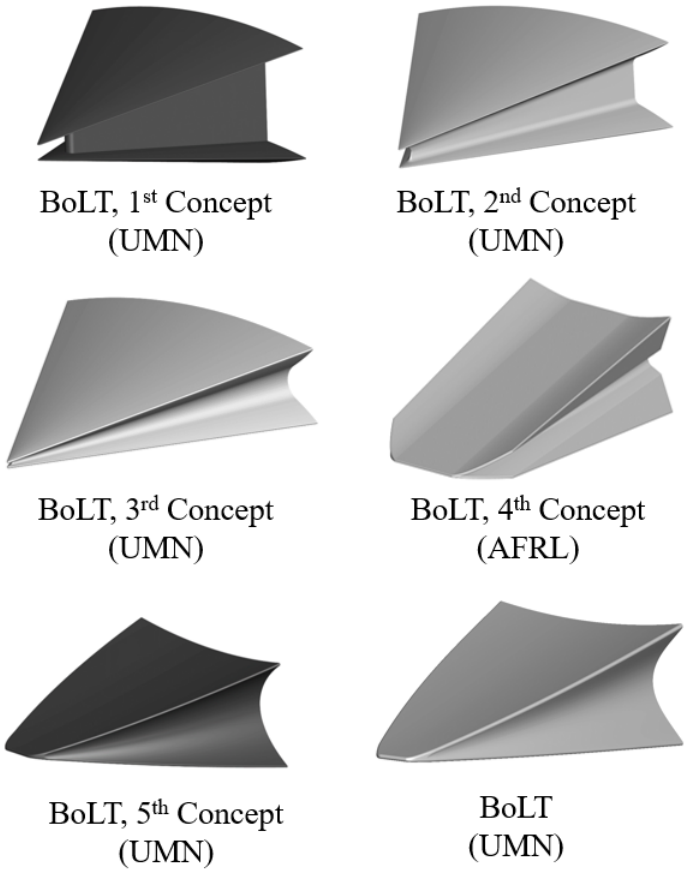

Figure 1.5: BoLT geometry concepts.

were designed to isolate flow from the swept leading edges within a low-pressure regions to channel flow away from the surfaces that are of interest. The intent is so the flow is isolated to prevent contamination of transition from different sides of the geometry.

The BoLT-2 geometry was developed by Texas A&M University (TAMU) and the concepts are shown in 1.6. The BoLT-2 geometry is identical to BoLT up to 0.866 m at which the surface slope and curvature is preserved. The original intent was meant to promote turbulent flow with an extended geometry while reaching much higher unit Reynolds number conditions in flight. Due to the low-pressure region in the gutter in combination with the extended geometry, a strong spanwise pressure

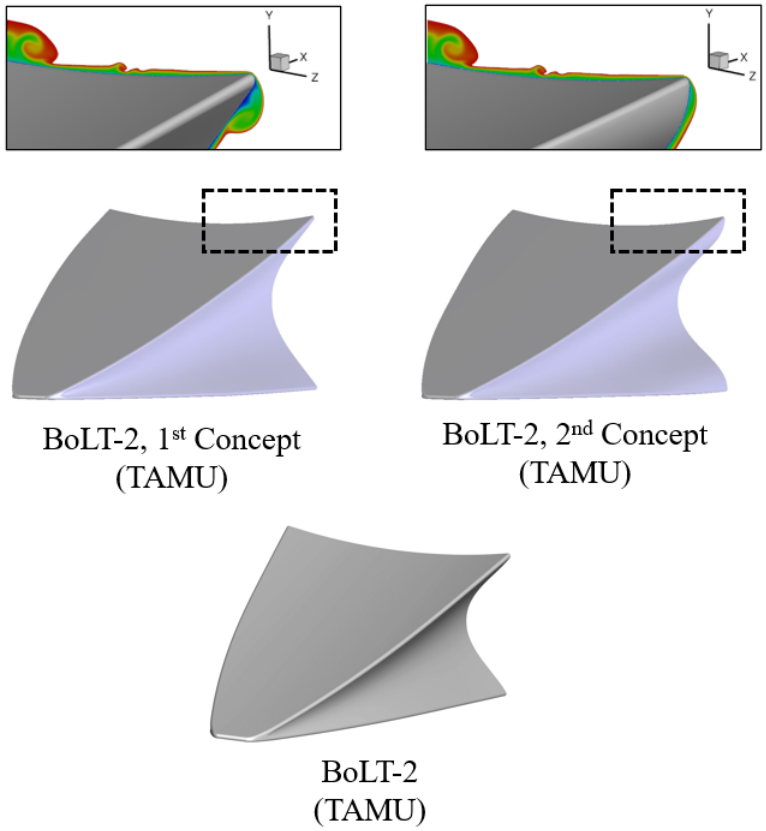

Figure 1.6: BoLT-2 geometry concepts.

gradient channels near wall streamlines to pass over the swept leading edge close to the back of the geometry. This then produced a small region of separation due to an adverse pressure gradient in the boundary layer. To address this, the next concept included a less drastic curvature near the swept edge of the gutter surface to help eliminate the separation bubble. Even though this was resolved, surface streamlines still pass over the swept leading edge due to the low-pressure region in the gutter. This can make it difficult for obtaining stable solutions in later chapters of this work. Furthermore, a drastic geometric expansion near the back of the research geometry can lead to flow separation and unsteady flow structures past the end of the research geometry as well. Nevertheless, the geometry was truncated to 1 m for the finalized

flight geometry to satisfy flight stability of the sounding rocket, and the so called fairing (geometric expansion) was deemed sufficient by the BoLT-2 team to minimize flow separation. This ensures that the boundary layer remains wall bounded in critical regions of the flowfield during flight.

1.1 Scope of the Present Work

The objective of this work is to further develop a general numerical methodology framework to study transition mechanisms for three-dimensional boundary layer transition through nonlinear breakdown to turbulence. This is motivated by the need to understand the relevant flow physics leading up to the nonlinear transition regime which has not been well characterized and to gain an understanding of potential transition processes seen in practice. The primary research configuration of interest is the Boundary Layer Turbulence (BoLT-2) geometry in order to help improve the understanding of the underlying flow physics contributing to elevated surface heating by simulating through the nonlinear transition regime. This is motivated by the fact that elevated heating is observed on the surface taking the form of streaks when viewing the surface heat flux from experiments of Figure 1.7. At higher Reynolds number conditions, the onset of transitional surface heating was observed [15].

The numerical studies in this work are achieved by performing Direct Numerical Simulation (DNS) and introducing external disturbances to the DNS solution in order to excite boundary layer instabilities. A numerical methodology is introduced within the existing finite-volume solver, US3D, and guidelines for obtaining accurate, high-fidelity solutions are established. Verification of the results are conducted by making comparisons to measurements obtained from wind tunnel experiments performed at the Mach 6 Quiet Tunnel at Texas A&M University. Modal analysis tools are used to extract pertinent information from simulation datasets to identify domi-

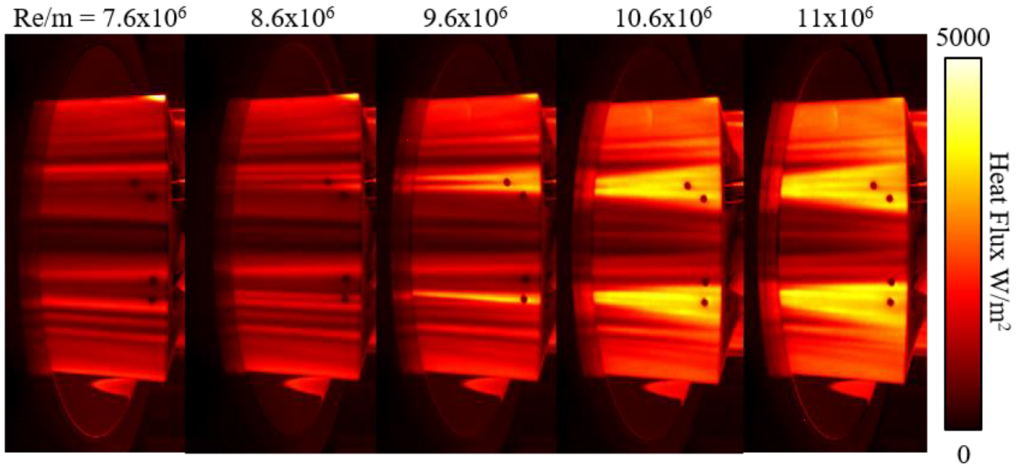

Figure 1.7: Infrared Thermography reveals elevated heat transfer rates at localized regions for a 25% subscale configuration of the BoLT-2 research geometry from Kostak-Teplicek [15]. View is of the top, back portion of the geometry and flow is from left to right with increasing freestream unit Reynolds.

nant modes in the BoLT-2 boundary layer. The modes are representative of relevant boundary layer instabilities that contribute to breakdown resulting in higher surface heating. This is necessary for understanding the underlying flow physics that are contributing to elevated heat transfer rates for vehicles travelling in the hypersonic flow regime. Furthermore, this provides a general framework capable of simulating the entire transition process up to a fully turbulent boundary layer state if the proper grid resolution is achieved to resolve the relevant length scales needed to capture a majority of the disturbance energy. Modal analysis techniques which consider a disturbance energy norm are used to quantify local fluctuations taking the form of dominant modes associated with boundary layer instabilities.

The remaining Chapters are summarized as follows: Chapter 1 introduces a brief literature review to introduce the pathways of boundary layer transition along with an overview of relevant boundary layer transition mechanisms which have been widely studied in the past. Chapter 2 presents the governing equations and numerical methods used in this work. The importance of high-order, low-dissipation methods for

simulating the transition process is discussed for problems with shock waves. Chapter 3 reviews environmental disturbance sources that are likely to cause transition and the numerical approaches used in this work for studying boundary layer instabilities are covered. Chapter 4 and 5 investigates the transition process for BoLT-2 under various flow conditions to identify which instabilities are contributing to breakdown in experiments. Finally, the transition process for the flight configuration at a flight condition identified to show evidence of transition based on flight data is investigated to understand how the transition process scales from ground test conditions to flight conditions.

1.2 Instability and Transition

1.2.1 Laminar to Turbulent Transition Processes

The pathways of boundary layer transition are often cited and categorized by the diagram as introduced by Morkovin [16]. Assuming that a boundary layer has a stable mean flow state, the laminar steady-state numerical solution is referred to as the baseflow or basic flow state. In simulation, the flow state can be obtained by solving for an approximate solution to the Navier-Stokes Equations. The ideal flow state that is obtained numerically can be physically unstable. However, the discrete solution may appear stable to do numerical dampening and absence of environmental disturbances. In actuality, the flow state is not ideal and transition is typically initiated by perturbations generated from some type of environmental source which can take the form of wind tunnel noise, freestream turbulence, particulates, surface roughness, or other. The process at which perturbations generated by environmental sources that then interact with a flowfield is referred to as receptivity. The linearized Euler equations for compressible flow have been shown to categorize several types of

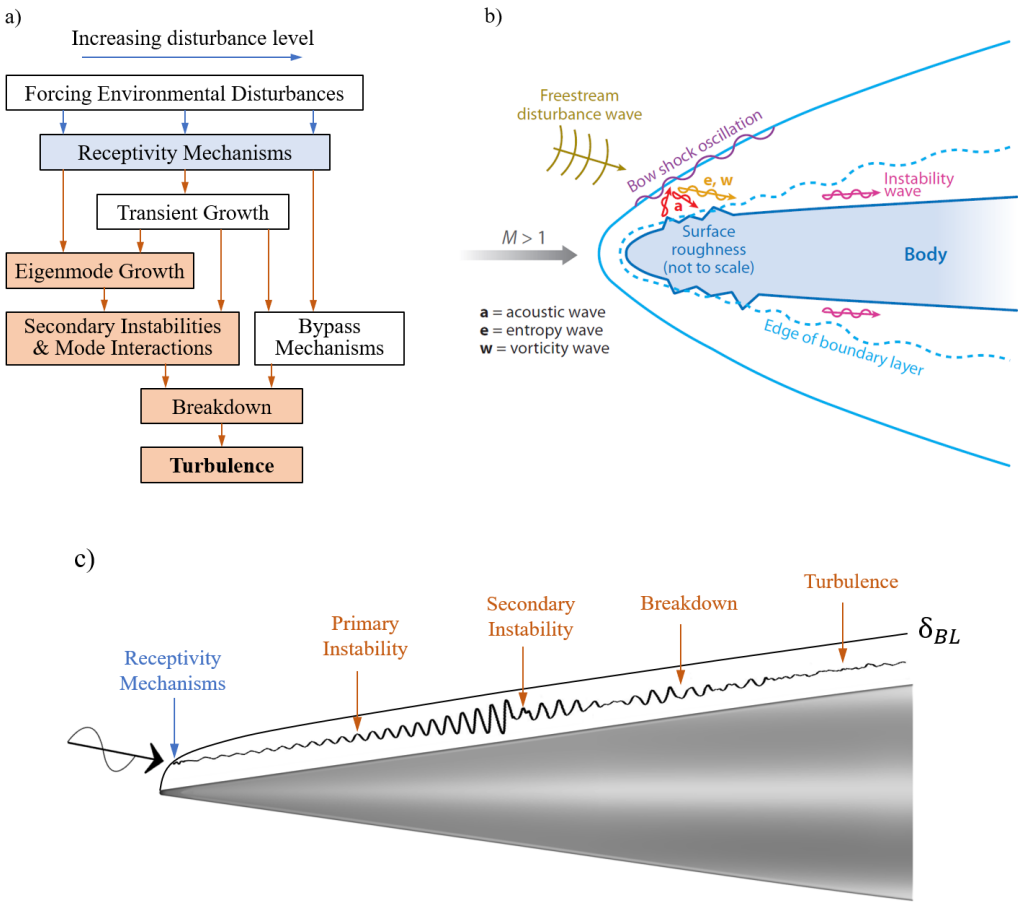

Figure 1.8: a) Pathways of Transition adapted from Morkovin [16]. b) Receptivity mechanisms induced by freestream disturbances and roughness [17]. c) Stages of boundary layer transition adapted from Hader and Fasel [18].

receptivity components of freestream waves taking the form of acoustic, entropic, and vortical components [19]. The acoustic waves are pressure perturbations which travel at the local speed of sound, entropic waves are density/temperature perturbations traveling with wave speeds equivalent to the local convection velocity, and vortical waves representing perturbations in velocity components. The flowfield disturbances can then "force" the flow by interacting with the meanflow and absorb energy from the meanflow. These involve nonlinear processes that cause local fluctuations to grow in amplitude through eigen-modes induced by local flow gradients that can support

a particular type of transition mechanism characterized by the boundary layer flow state. The definition of nonlinearity within the boundary in this work refers to when disturbances become sufficiently large in amplitude at which the disturbances interact with the meanflow. Once the disturbances absorb enough energy from the meanflow, secondary instability growth or the interactions of multiple boundary layer instabilities can contribute to exponential disturbance energy growth. This can lead to breakdown to small-scale coherent structures producing spatio-temporal fluctuations seen by local flow quantities - commonly referred to as turbulence. Therefore, the amplification process takes the form of eigen-modes resulting from modal or non-modal (transient) growth transition mechanisms. If the environmental disturbance source produces very large flowfield fluctuations, the large perturbations can lead to a bypass of the transition process thus tripping the boundary layer to a turbulent state. Therefore, this implies that the initial disturbance amplitude is a major contributing factor for the pathway a boundary layer may transition and is dictated by the type of instabilities which support propagating waves specific to the instability.

1.2.2 Compressible Boundary Layer Transition Mechanisms

Mack's First-Mode and Second-Mode Instabilities

Several types of instabilities can contribute to transition by means of amplifying disturbance quantities leading to transition within a hypersonic boundary layer. Two types of instability mechanisms were identified by Mack [20] in two-dimensional boundary layers using linear stability theory (LST) and are commonly referred to as first- and second-modes. The first- and second-modes can become important to the transition process by absorbing energy from the mean flow and have been study extensively within experiments and simulations. The first-mode is a viscous instability of a compressible boundary layer taking the form of streamwise unstable waves,

analogous to Tollmien-Schlichting waves for incompressible flow. The second-mode is an inviscid instability where the boundary layer acts as an acoustic wave guide such that the instability is tuned to the local boundary layer properties causing a reflection of acoustic waves between the wall and the relative sonic line [21]. Resulting from this are acoustic waves which become visible near the boundary layer edge that radiate from the boundary layer and diffuse into the meanflow further away from the wall. For hypersonic flows, second-mode is typically found to be more unstable over first-mode in compressible boundary layers [21]. Work by Li et al. [22] demonstrated for high-speed boundary layer flows that three-dimensional secondary instabilities can arise and lead to nonlinear evolution of second-mode waves for cone configurations.

Stationary and Travelling Crossflow Instabilities

With the extension to three-dimensional space, additional transition mechanisms can exist within a high speed, compressible boundary layer. One of these instabilities is the so called crossflow instability. This is produced by a crossflow velocity component, and occurs when the boundary layer velocity profile contains an inflection point. This is contributed by misalignment of the inviscid velocity vector and spanwise pressure gradient resulting in varying momentum and pressure gradients near the wall [23]. It is possible for the inflection point to become inviscidly unstable leading to transition and has two types of eigen-modes. One type is a stationary-mode resulting from steady forcing near the inflection point taking the form of stationary crossflow instabilities. This instability is a result of steady forcing and to not to be confused with steady crossflow vortices. Crossflow instabilities have been observed for a number of configurations in the past such as for a cone at an angle of attack [24], a yawed cone [25], the HIFiRE-5 2:1 elliptic cone [26], and BoLT [11]. For BoLT, Thome et al. [10] showed the stationary crossflow mode can become a dominant transition mechanism due to its sensitivity to roughness. For longer geometries under specific conditions,

crossflow can cause the development of steady streamwise vortices capable of supporting vortical instabilities. Furthermore, [27] showed that roughness on the HIFiRE-5 geometry can lead to the formation of coexisting vortical structures, referred to as vortex doubling. The other eigen-mode of crossflow is a temporal mode commonly referred to as travelling crossflow instability which has an associated wave angle and phase speed. Stationary crossflow instabilities are more likely to be a dominant instability where the freestream environment contains low noise levels. Meanwhile, travelling crossflow instabilities tend to dominant in the presence of broadband, large amplitude freestream environments.

The interaction of disturbances with developing vortex structures in a region favoring crossflow have been shown to initiate breakdown on a 25% subscale, 1.5 meter BoLT-2 geometry and will be introduced in later Chapters. Furthermore, flow modulated by crossflow vortices are highly susceptible to high-frequency secondary instability modes (SIMs) present near shear layers when disturbances are introduced to vortices developing in regions of crossflow [28]. Secondary instability of crossflow has been studied in the past with Wassermann and Kloker [29] introducing a number notation and Malik et al. [30] defining a letter notation for the same secondary flow effects:

- Type-I: A high frequency mode driven by strong spanwise velocity gradients located on the upwash side of crossflow vortex.
- Type-II: A high frequency mode driven by strong streamwise velocity gradients generated by intense wall-normal gradients located at the top portion (crest) of the crossflow vortices. Recent work has shown that the secondary flow behavior can appear near the trough portion induced by similar velocity gradients as seen from Figure 1.9.
- Type-III: A low frequency mode driven by strong spanwise velocity gradients

and located on the upwash side of the crossflow vortex.

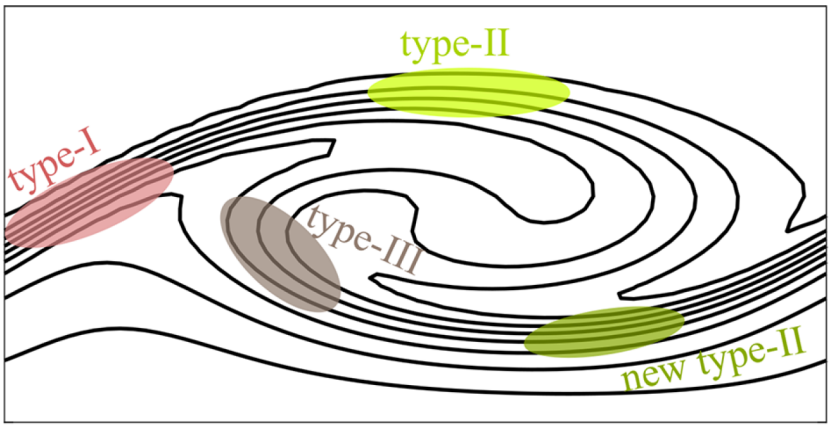

Figure 1.9: Schematic illustrating regions of secondary instability mechanisms of crossflow instability within developing vortex structures of a boundary layer reported by Chen and Xu [28]. The streamwise velocity component, u, is pointing into the page.

1.2.3 Instabilities Identified on BoLT

When boundary layers become lifted due to strong spanwise gradients, this allows the development of steady, streamwise vortex structures. This has typically been observed near the centerline for the HIFiRE-5 elliptic cone, the BoLT/BoLT-2 flight experiment geometries, and for lifting body geometries such as the Hyperonsic Transition Research Vehicle (HyTRV) [31]. At higher Reynolds numbers, the lifted boundary layer tends to roll up at which the upwash side results in a significantly thickened boundary layer thickness containing strong shear gradients capable of supporting vortical instabilities. In the case of small-scale streamwise vortices, the vortical instabilities are typically localized further away from the wall and target regions having the largest velocity gradients. The understanding of such instabilities are often quantified using a type of modal analysis tools to isolate eigen-modes associated with instabilities for stability analysis.

Many types of modal analysis techniques have been used to extract spatio-temporal information from flowfield snapshots generated by simulations. An overview of current modal analysis techniques with their applications are described in the papers by Taira et al. [32, 33]. Many of these analysis techniques are purely data-driven and typically apply modal decomposition to a dataset of a particular flow variable, or of an operator relevant to the system. One such modal analysis tool capable of extracting pertinent information from computational datasets is dynamic mode decomposition (DMD). DMD is a modal analysis tool that can extract dynamical information provided a sequence of snapshots in time.

Numerical simulations and analysis by Knutson et al. [11] using Sparsity-promoting DMD (SPDMD) [34] revealed multiple instabilities in the BoLT flowfield. These instabilities have been defined as a vortical mode near the centerline, traveling crossflow near the swept edge, and a region containing mixed-modes that are thought to correspond to an interaction between different types of coexistent instabilities. This has provided useful insight into the types of transition mechanisms contributing to linear growth of disturbances for BoLT and are consistent with subscale experimental measurements [13]. At higher Reynolds numbers, there is a development of stationary crossflow vortices located between the centerline and swept edge. The interaction of disturbances with the crossflow vortices have been shown to initiate breakdown observed on the surface of BoLT-2 and results are shown in later chapters.

1.2.4 Simulation Methodology

Now knowing the types of instabilities that we may expect to contribute to breakdown on the BoLT-2 configuration, DNS is the tool used for boundary layer stability analysis because the spatial homogeneity of this particular flowfield should not be assumed. Therefore, in theory, the DNS datasets include linear and nonlinear flow processes along with potential mode interactions since it is demonstrated that the solver is able

to simulate the effects based on supporting cases of this thesis. Furthermore, the excitation of instabilities is achieved by convecting disturbances without constraining the propagation of waves to specific paths or frequency bands which might favor particular instabilities. This requires some type of physical disturbance that must propagate through the domain and has to first be imposed as a boundary condition for simulating instabilities of the DNS. In flight and wind tunnel experiments, boundary layer instabilities arise due to some type of external forcing that can take the form of freestream disturbances that enter the boundary layer through receptivity. Since comparisons are being made to wind tunnel measurements, a forcing approach is utilized and is meant to mimic effects similar to quiet wind tunnel noise to obtain a response representative of natural transition. This provides a more representative model of a quiet wind tunnel environment by using a stochastic, broadband forcing function to allow the boundary layer to select a response representative of natural transition. This is different than what was previously used to investigate the linear stages of transition on BoLT by Knutson et al. [11] which applied a strip of stochastic momentum forcing at the wall. Since DNS is used as a numerical tool for boundary layer analysis, a high-order, low-dissipation numerical method is used and is required to accurately capturing the amplification and growth of disturbances induced by boundary layer instabilities. A similar approach is applied at flight conditions to help provide an understanding of transition in flight at which simulation data could be used for interpreting flight data once it becomes available.

Chapter 2

Numerical Method

This chapter introduces relevant numerical methods for calculating solutions with the compressible Navier-Stokes equations, address the computational challenges related to simulating the physical phenomena inherent to high speed compressible flows, and numerical methodology required to properly simulate boundary layer instabilities in three-dimensional boundary layers. This includes discussion of numerical methods for obtaining accurate, high-fidelity solutions by performing direct numerical simulation with supporting test cases.

2.1 Navier-Stokes Equations

The governing equations solved in this thesis are the Navier-Stokes equations and are valid for flows that satisfy the continuum assumption based on the local mean free path (average distance molecules travel between collisions) being sufficiently small. This is true for all problems in this thesis. Therefore, the equations that describe the

conservation of mass, momentum, and energy are:

$$\frac{\partial \rho}{\partial t} = -\frac{\partial \rho u_j}{\partial x_j} \tag{2.1}$$

$$\frac{\partial \rho u_i}{\partial t} = -\frac{\partial}{\partial x_j}(\rho u_i u_j + p\delta_{ij} - \sigma_{ij}) \tag{2.2}$$

$$\frac{\partial E}{\partial t} = -\frac{\partial}{\partial x_j}((E+p)u_j - \sigma_{ij}u_i + q_j) \tag{2.3}$$

The density is denoted as ρ and the velocity vector is u_j with respect to the three spatial directions, x_j, in the Cartesian coordinate system. Thus, the three components of velocity, u_j, where $j = 1, 2, 3$ are denoted as u, v, w.

The freestream conditions for the cases of interest investigated in this work have a relatively low total enthalpy since O_2 dissociation typically occurs around 2 MJ/kg. Because the total enthalpy remains well below this value and temperature of the gas is relatively low for all cases in this thesis, the gas does not contain a significant thermal energy increase to trigger reactions and energy relaxation at any appreciable level. Therefore, the internal energy relaxation and potential chemical reactions are insignificant in terms of the effect on the boundary layer state. Even though the gas is not in chemical and thermal equilibrium, a gas in chemical and thermal equilibrium would likely behave similarly under the conditions of this thesis. For this reason, the cases in this thesis assumes air with the equation of state for a thermally perfect gas where the pressure is calculated as, $p = \rho RT$. Temperature is calculated from the specific internal energy, $e = c_v T$. For a calorically perfect gas, the specific heat at constant pressure and volume, c_p and c_v respectively, are assumed to be constant and related by $c_p = R + c_v$. The ratio of specific heats, γ, is 1.4 and obtained from the gas constant for air, $R = 287.05$ J/(kg·K). Therefore, the speed of sound calculated as $a = \sqrt{\gamma RT}$.

Vibrational and electronic excitation is neglected since the vibrational temperature

of O_2 is about 2239 K. For most cases, vibrational excitation of O_2 begins around 800 K and becomes increasingly significant at higher temperatures. Furthermore, this depends greatly on the leading edge radius of a vehicle and varies on a case-by-case basis. Aside from this, we generally expect that vibrational excitation of oxygen occurs for flows having a freestream enthalpy over 1 MJ/kg. Nevertheless, the total energy per unit volume for the governing equations above takes into account the sum of kinetic and internal energies defined as,

$$E = \frac{1}{2}\rho u_i u_i + \rho c_v T. \tag{2.4}$$

The viscous stress tensor, σ_{ij}, is represented as shear components of velocity taking the form of a combination of first derivatives of each velocity component,

$$\sigma_{ij} = \mu\left(\frac{\partial u_i}{\partial x_j} + \frac{\partial u_j}{\partial x_i}\right) - \lambda\frac{\partial u_k}{\partial x_k}\delta_{ij}, \tag{2.5}$$

The dynamic viscosity, μ, and bulk modulus, λ, is related with Stokes' hypothesis of zero bulk viscosity by $\lambda = -\frac{2}{3}\mu$. The dynamic viscosity is assumed to be a function of only temperature using Sutherland's law,

$$\mu(T) = \mu_o\frac{T^{3/2}}{T + T_o}. \tag{2.6}$$

A reference viscosity of $\mu_o = 1.458x10^{-6}$ kg/(m·s) and reference temperature of $T_o = 110.3$K is assumed. The heat flux vector is derived from Fourier's Law of heat conduction and related by the thermal gradient,

$$q_j = -\kappa\frac{\partial T}{\partial x_j} = -(\kappa_{tr} + \kappa_{rot})\frac{\partial T}{\partial x_j}, \tag{2.7}$$

The thermal conductivities for the translational and rotational energy modes are

obtained from an Eucken relation, $\kappa_{tr} = \frac{5}{2}\mu c_v$ and $\kappa_{rot} = \mu c_v$.

2.2 Finite Volume Method

Before boundary layer instabilities can be simulated, a converged mean flow state is required. Since the governing equations are the Navier-Stokes equations which are set of nonlinear partial differential equations (PDEs), a numerical method capable of solving nonlinear hyperbolic equations is required. Historically, the most commonly used numerical methods are finite difference and finite volume methods. In recent years, higher order methods such as Discontinuous-Galerkin (DG) methods have shown potential in addressing some of the challenges encountered by finite difference and finite volume approaches. However, current DG approaches are still in the early stages of development since they are often challenging to implement and deemed to be computationally expensive. Despite these reasons, finite difference and finite volume methods have received much more attention since they are relativity more simple to implement. As a consequence, the development of a higher order method is outside the scope of this work. Therefore, a finite volume method is used where the governing equations can be rewritten in conservation law form (or divergence law form):

$$\frac{\partial U}{\partial t} + \frac{\partial F_j}{\partial x_j} = 0 \tag{2.8}$$

The vector of conservative variables and flux vector are represented by,

$$U = \begin{Bmatrix} \rho \\ \rho u \\ \rho v \\ \rho w \\ E \end{Bmatrix}, \qquad F_j = \begin{Bmatrix} \rho u_j \\ \rho u u_j + p\delta_{1j} + \sigma_{1j} \\ \rho v u_j + p\delta_{2j} + \sigma_{2j} \\ \rho w u_j + p\delta_{3j} + \sigma_{3j} \\ (E+p)u_j + \sigma_{kj}u_k - q_j \end{Bmatrix} \tag{2.9}$$

The equations written in this form are then integrated over an arbitrary control volume (V_i) with an enclosed surface or boundary faces where U_i is the average over the cell being evaluated,

$$\int_{V_i} \frac{\partial U}{\partial t}\, dV = -\int_{V_i} \frac{\partial F_j}{\partial x_j}\, dV \tag{2.10}$$

This is referred to as the weak form of the conservation equations. Gauss' divergence theorem is then applied to convert the volume integral on the right hand side into a surface integral allowing for integration over the control volume and the boundary surface.

$$V_i \frac{\partial U_i}{\partial t} = -\oint_{\partial V_i} F'_f\, dS \tag{2.11}$$

The surface normal flux, $F'_f = F_j \cdot \hat{n}$, is the component of the flux vector in the surface-normal direction which points outward with respect to the boundary. By assuming that a control volume takes the form of a computational element, the above integral expression can be represented approximately with a discrete summation of the fluxes at each element face,

$$\frac{\partial U_i}{\partial t} = -\frac{1}{V_i} \sum_{faces} F'_f S_f \tag{2.12}$$

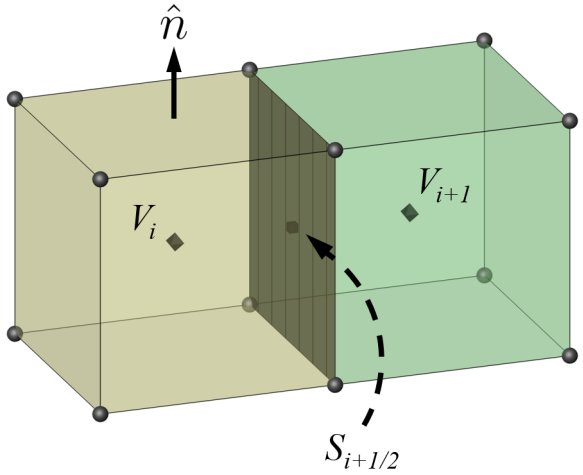

Figure 2.1: Naming convention for two neighboring, arbitrary finite volume cells corresponding to discrete three-dimensional control volumes represented as hexahedral elements. Element nodes are denoted by the grey spherical points located at the vertices of each element. The cell-centers are represented by diamonds. The element face normal is shown where the positive direction is pointed outward from the cell-center. The shared face between elements is represented by the grey shaded face and is where the flux is computed.

The subscripts i and $i+1$ of Figure 2.1 represent the cell-centers of the cell evaluated and neighboring cell for the flux at the shared face, respectively. S_f is the face area and is denoted by the half-index naming convention such that the subscript $i+1/2$ is the face center. Therefore, $F'_f = F_j \cdot \hat{n}$ represents the flux vector, F_j, at face, $S_{i+1/2}$, which is dotted with the unit normal, $\hat{n}_f$, pointing from cell i to $i+1$.

The field variables of the governing PDE's obtained from the integral form are smoother than field variables obtained when calculating approximate solutions to the weak form of the equations. Nonetheless, this allows the discrete form to handle flow discontinuities that appear in compressible flows. This can arise due to the nonlinearity of the convective terms which can allow waves to sharpen and result in the formation of shock waves. Considering this, along with the above formulation, spatial integration is performed by interpolating data stored at the cell-centers to derive a spatial flux at the face. It is important to note that the terms of the spatial fluxes are a

combination of convective and diffusive terms resulting from the governing equations. For compressible flows, this implies that the convective terms are hyperbolic in nature. This means the solutions contain wave-like properties at which the information travels along the PDE's characteristic directions. This allows for a formulation which defines an inviscid portion of the spatial flux separately from the viscous portion. The purpose of this is because the inviscid flux requires special treatment which takes into account their hyperbolic nature and nonlinearity. As for the viscous terms of the spatial flux, they behave elliptic in nature which allows for a relativity more simple and efficient implementation which will be discussed later on. Therefore, the flux vector then takes the following form where prime denotes the surface normal directions:

$$F' = F'_I + F'_V \tag{2.13}$$

Utilizing the Cartesian coordinate system, the inviscid and viscous components of the spatial flux are written as [35],

$$F'_I = \begin{Bmatrix} \rho(u\hat{n}_x + v\hat{n}_y + w\hat{n}_z) \\ \rho u(u\hat{n}_x + v\hat{n}_y + w\hat{n}_z) + p\hat{n}_x \\ \rho v(u\hat{n}_x + v\hat{n}_y + w\hat{n}_z) + p\hat{n}_y \\ \rho w(u\hat{n}_x + v\hat{n}_y + w\hat{n}_z) + p\hat{n}_z \\ (E+p)(u\hat{n}_x + v\hat{n}_y + w\hat{n}_z) \end{Bmatrix} \tag{2.14}$$

$$F'_V = \left\{ \begin{array}{r} 0 \\ \sigma_{xx}\hat{n}_x + \sigma_{xy}\hat{n}_y + \sigma_{xz}\hat{n}_z \\ \sigma_{yx}\hat{n}_x + \sigma_{yy}\hat{n}_y + \sigma_{xz}\hat{n}_z \\ \sigma_{zx}\hat{n}_x + \sigma_{zy}\hat{n}_y + \sigma_{zz}\hat{n}_z \\ (\sigma_{xx}u + \sigma_{xy}v + \sigma_{xz}w - q_x)\hat{n_x} \quad + \\ (\sigma_{yx}u + \sigma_{yy}v + \sigma_{yz}w - q_y)\hat{n_y} \quad + \\ (\sigma_{zx}u + \sigma_{zy}v + \sigma_{zz}w - q_z)\hat{n_z} \end{array} \right\} \tag{2.15}$$

2.3 Inviscid Fluxes

2.3.1 Steger-Warming Flux Vector Splitting

Steger and Warming were some of the first to introduce flux vector splitting based on the method of characteristics for the Euler equations which are known to be homogeneous with respect to the vector of conserved quantities. Solutions can be obtained where the eigenvalues of the system have wave speeds of $u + a$, u, and $u - a$ which represent the wave speeds of fast acoustic waves, convective waves, and slow acoustic waves, respectively [36]. This means that when flow is subsonic ($a > u$), waves may be allowed to travel in all directions. Whereas, when ($a < u$), information travels in a single direction.

Since the inviscid flux is hyperbolic, it is discretized using the method of characteristics such that the solution of the inviscid flux allows for a solution to wave motion with corresponding wave speeds represented by the eigenvalues of a Jacobian matrix. Additionally, this method follows a special property which states that the flux is homogeneous. For example, consider $F = F(U)$ where F is a function of a set of field variables contained in vector U. The matrix of partial derivatives, U', is λU for any

nonzero scalar, λ. If F satisfies, $F(U') = \lambda$ F(U), then F is said to be homogeneous with respect to U. This means that the property satisfies $F(\lambda U) = \lambda(FU)$ such that the Jacobian matrix, A, is $\partial F/\partial U$.

Therefore, we are assuming that the inviscid flux is homogeneous with respect to the state vector, U, allowing us to define a linearization exactly with a Jacobian matrix as,

$$F'_I = \frac{\partial F'_I}{\partial U} U = A'U \tag{2.16}$$

The partial, $\frac{\partial F'_I}{\partial U} = A'$, is the Jacobian matrix of F'_I with respect to U. The eigenvalues and eigenvectors of the flux Jacobian can be computed directly but requires many steps for implementation. Therefore, a cleaner form is desired by rewritting the elements of the Jacobian matrix in terms of the elements of U and then taking the partial derivatives. The purpose of this is because a diagonalization of the Jacobian is required with an eigen-decomposition then the derivatives are computed along characteristic directions using upwind biasing. Therefore, this is achieved by defining the conserved variables of U in terms of the primitive variables, V, such that $U = U(V)$ and $V = [\rho, u, v, w, p]^T$. Therefore, the Jacobian matrix is expressed as,

$$A' = \frac{\partial U}{\partial V}\frac{\partial V}{\partial U}\frac{\partial F'_I}{\partial V}\frac{\partial V}{\partial U} \tag{2.17}$$

where

$$\frac{\partial V}{\partial U}\frac{\partial F'_I}{\partial V} = C^{-1}\Lambda C \tag{2.18}$$

is the diagonal form of the transformed Jacobian written in terms of primitive variables. It is observed that the matrix obtained from $\frac{\partial V}{\partial U}\frac{\partial F'_I}{\partial V}$ is a similar matrix to $\frac{\partial F'_I}{\partial U}$

which both have the same eigenvalues. The reason we know this is because we choose the invertible matrix $\frac{\partial V}{\partial U}$ and its inverse to post- and pre-multiply the synthetic matrix in question. This is the definition of similar matrices. It was further observed that the synthetic matrix is easier to diagonalize. The matrix Λ is the diagonal matrix of eigenvalues, $\Lambda = \text{diag}(\lambda, \lambda^+, \lambda, \lambda, \lambda^-)$ and $\lambda = u', \lambda^+ = u' + a$, and $\lambda^- = u' - a$. Here u' is the characteristic propagation speed due to the bulk velocity and $u' \pm a$ are the characteristic acoustic wave speeds. The columns of C are the associated eigenvectors. The flux Jacobian can then be written as,

$$A' = \frac{\partial U}{\partial V} C^{-1} \Lambda C \frac{\partial V}{\partial U} = S^{-1} C^{-1} \Lambda C S \tag{2.19}$$

where $S = \partial V / \partial U$ is the transformation from conserved variables to primitive variables and $S^{-1} = \partial U / \partial V$. The matrices C and S are defined in [37]. Next, we split F'_I into components associated with the direction of the characteristics determined by the positive and negative eigenvalues of Λ.

$$F'_I = F'_{I+} + F'_{I-} = A'_+ U + A'_- U \tag{2.20}$$

This enables upwinding since the sign of the eigenvalues represents the local direction of propagation and the magnitude correspond to the linear waves of the flowfield. This is an important notion for realistic problems since slow acoustic waves are capable of having negative characteristic wave speeds within the subsonic portion of a boundary layer. This is contrary to vorticity, entropy, and fast acoustic waves, which are those that, by convention, we consider to have positive wave speeds. This is a convention for how the orientation of the "normal direction" in a flowfield is chosen such that a numerical scheme capable in simulating compressible flow problems is

successfully formulated. Therefore, the split Jacobians become,

$$A'_+ = S^{-1}C_+^{-1}CS \qquad\qquad A'_- = S^{-1}C_-^{-1}CS \tag{2.21}$$

The flux at each face can be constructed by evaluating the Jacobians with cell centered or face centered data. The original Steger-Warming flux vector split scheme used upwind biasing and data from the cell centers to evaluate the Jacobians,

$$F_{I_f}' = A'_{+i}U_i + A'_{-i+1}U_{i+1} \tag{2.22}$$

The scheme is first-order accurate since upwind data at U_i and U_{i+1} are used to compute the flux at the face, $i+1/2$. As written, a second-order accurate scheme could potentially be formulated if left and right data were used since symmetric schemes are higher order. However, because the eigenvalues in the Steger-Warming scheme choose data from only one side, a first-order scheme for cell i is obtained. Therefore, MacCormack and Candler [38] proposed a modification to the scheme by using the Jacobians evaluated at the face,

$$F_{I_f}' = A'_{+f}U_i + A'_{-f}U_{i+1} \tag{2.23}$$

where the Jacobians are computed at the face by taking the arithmatic mean of the states at the cell centers, U_i and U_{i+1},

$$A_{\pm_f}' = A'_{\pm}\left(\frac{1}{2}(U_i + U_{i+1})\right) \tag{2.24}$$

This is commonly referred to as the modified Steger-Warming flux scheme, and results in less numerical dissipation; thus is more desirable for obtaining more accurate flow calculations. In some cases, numerical stability may require more numerical

dissipation such as near flow discontinuities. An example of this would be for a high Mach number flow near strong shock waves. Therefore, the current upwind flux used in this work smoothly varies between the original Steger-Warming flux at strong shocks and reverts back to the modified Steger-Warming flux in other regions of the flow. This is achieved by evaluating the Jacobians, A'_+ and A'_-, with,

$$U_+ = w_f U_i + (1 - w_f) U_{i+1} \qquad U_- = (1 - w_f) U_i + w_f U_{i+1} \tag{2.25}$$

where $w_f \in [1/2, 1]$ is a pressure-dependent weighting function that reaches a maximum value of 1 in the presence of sharp pressure jumps and is equivalent to the original Steger-Warming flux. In other regions of the flow where the gradients remain smooth, a dissipative flux with the dissipative properties of the modified Steger-Warming flux is achieved when w_f approaches 1/2.

As mentioned by Candler et al. [37], the introduced flux formulation may work exceptionally for standard 1-D test problems but produces insufficient accuracy for realistic high Mach number flows on non-ideal grids. The scheme suffers from an accumulation of numerical error occurring when the eigenvalues of the Jacobian approach zero near stagnation regions. This can be observed for high Mach number flows with strong shocks waves where the numerical error may grow in magnitude and alter the flow physics aphysically. One such example of this is a so-called carbuncle [39] may arise in the solution and produce a large displacement of the bow shock wave near the stagnation region of a blunt leading edge. This is associated with an aphysical recirculation zone near the stagnation point. Typically, the problem is prevented by aligning the grid with the bow shock wave to reduce numerical error contributed by the flux calculation, and to limit the eigenvalues of the dissipative flux component to reduce the potential growth of numerical error. In this work, the eigenvalues are

augmented to prevent them from approaching zero using,

$$\lambda'_{\pm]} = \frac{1}{2}\left(\lambda_{\pm} \pm \sqrt{\lambda_{\pm}^2 + \epsilon^2}\right) \tag{2.26}$$

where the eigenvalue, $\lambda_{\pm}$ (either u',$u' + a$, or $u' - a$), is an element of $\Lambda_{\pm}$ and the sign depends upon whether the contribution is to Λ_+ or Λ_-. By observation, the eigenvalues become larger in the direction information propagates meaning that flux is added. The limiting value as λ approaches zero is $\epsilon = \epsilon_o a$ and ϵ_o should be chosen to be large enough to maintain the solution from becoming aphysical in stagnation regions; typically, $0.1 \leq \epsilon_o \leq 0.3$. Furthermore, this type of eigenvalue limiting must not be applied in boundary layers because it induces an artificial flux across the boundary layer [37]. The solutions obtained in the results sections of this thesis, sets ϵ_o to zero in the boundary layer, and is then increased to 0.3 outside of the boundary layer along grid lines.

2.3.2 Higher-Order Spatial Accuracy

As briefly discussed in the former section, there can be a number of issues that arise when the introduced flux scheme is used for obtaining solutions under practical high Mach number flow conditions and for non-ideal grids which are almost always used in practice. It may be enticing to use a more dissipative scheme, such as the first order accurate scheme of the last section, to obtain improved convergence for steady-state problems. However, especially for unsteady DNS calculations, this is detrimental to the resolved spatial length scales of the underlying flow physics which requires high-order spatial accuracy. When resolving gradients for transition studies, the numerical dissipation properties of the upwind Steger-Warming fluxes smooths gradients and acts as artificial viscosity. In the case of high Reynolds number flows, the artificial viscosity (numerical dissipation) may obtain an inaccurate boundary layer profile that

is representative of a much lower Reynolds numbers than what is actually simulated. Therefore, one way to extend a spatial scheme to higher order is to use the Monotonic Upstream-centered Scheme for Conservation Laws [40] (MUSCL) approach. This approach performs a higher order reconstruction of the piecewise constant data associated with a larger dataset by using a polynomial of low degree and a slope limiter taking the form of a monotonic function to preserve the order of accuracy. Therefore, higher order accuracy of the Steger-Warming scheme is achieved by increasing the stencil size of the left and right states, which are no longer assumed to be local left ($U_L = U_i$) and right ($U_R = U_{i+1}$) cell centered data, with an extrapolation to the face $(i + 1/2)$:

$$F'_{If} = A'_{+f}U_L + A'_{-f}U_R \tag{2.27}$$

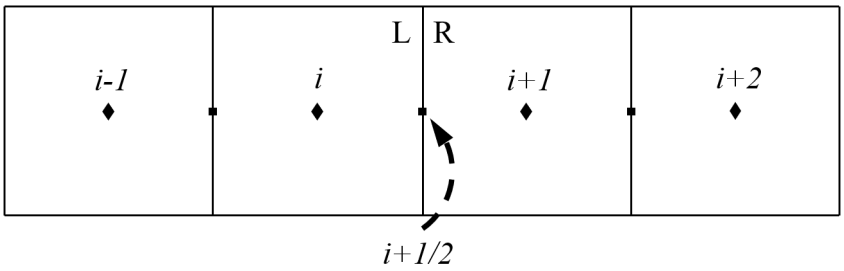

Figure 2.2: Schematic of stencil used to extrapolate to cell faces.

A higher order stencil approximates U_L and U_R using neighboring cell-centered data. For example, a second-order accurate reconstruction can be obtained on a 1-D grid using a simple extrapolation to the face at $i + 1/2$ using neighboring data [37] as seen in equation(2.28).

$$U_L = \frac{3U_i - U_{i-1}}{2} \qquad\qquad U_R = \frac{3U_{i+1} - U_{i+2}}{2} \tag{2.28}$$

It should be noted that a second-order spatial approximation of the flux from

Equation 2.27 will be attained even if a higher order reconstruction, such as a third order spatial approximation, were obtained for U_L and U_R. This is because the Jacobian matrix is evaluated with the arithmetic mean and as a consequence reduces the overall accuracy of the flux [35]. Nonetheless, the numerical flux function is not useful on its own for practical applications since aphysical overshoots and undershoots arise near strong gradients. This is because the scheme defies monotonicity making it so the Total Variation Diminishing (TVD) property is no longer satisfied. In order to handle spurious behavior, the extrema of the left and right data is limited such that no new extrema is produced to keep the flux physically meaningful. This is commonly addressed with a so called slope limiter by comparing changes in the solution and selecting a conservative value. Therefore, in this work the left and right states are,

$$U_L = U_i + \frac{1}{2}\phi(r_i)(U_{i+1} - U_i) \qquad U_R = U_{i+1} + \frac{1}{2}\phi(r_{i+1})(U_{i+2} - U_{i+1}) \tag{2.29}$$

where the slope limiter, $\phi(r)$, will detect an aphysical solution near strong gradients and modify U_L and U_R [1]. This requires that the slope limiter be a function of the smoothness parameter, r, which is a ratio of adjacent slopes to ensure the scheme satisfies monotonicity. For the left and right, the smoothness parameter is $r_i = (U_{i+1} - U_i)/(U_i - U_{i-1})$ and $r_{i+1} = (U_{i+2} - U_{i+1})/(U_{i+1} - U_i)$, respectively. Recall, the flux function reverts to the first-order accurate flux scheme in particular regions of the solution, such as near flow discontinuities. Therefore, it is important that a sufficient slope limiter is used to refrain from applying a first-order accurate scheme in regions of interest. In general, the choice of a limiter can have a significant impact on numerical behavior or affect numerical error which is directly related to the grid resolution. This can lead to different solutions for varying types of problems and so the choice of limiter can be important. Consequently, a number of limiters have been

[1] An appropriate reformulation of the MUSCL scheme is used within US3D which does not become singular.

introduced in the literature and are summarized by Lee [41]. The most commonly used limiters are the minmod, Van-Leer, and Superbee [42] since they are second-order TVD [43]. The minmod limiter, $\phi(r)$ =max[0,min$(1, r)$], is utilized in this work since it is more conservative such that it is more robust in the sense of handling strong shock waves.

2.3.3 Low-Dissipation Flux Formulation

The previous section discussed that flux limiting is applied to allow for a higher-order dissipative flux in smooth regions of the solution and revert to first-order accuracy near flow discontinuities in order to maintain numerical stability. Historically, upwind methods have been utilized for compressible flows since they are stable and capture shock waves. However, the amount of numerical dissipation associated with the second-order upwind scheme would make a DNS calculation too costly to resolve relevant wave properties and fine scale structures if one were interested in studying boundary layer transition or turbulence. Therefore, an adequate scheme must have low amounts of numerical dissipation and be nonlinearly stable; that is, they must be capable of resolving shock waves and relevant vortical structures. One way to do this is by using a non-dissipative, central scheme in combination with a numerical sensor that detects where shock waves are present to restrict the upwind scheme to particular regions as required for numerical stability.

Following Candler et al. [37], the inviscid flux of Equation 2.27 is expanded using the definitions from Equation 2.19 and re-arranging the expression as a sum of a

symmetric and upwind components gives,

$$\begin{aligned} F'_f &= (S^{-1}C^{-1}\Lambda_+ CS)U_L + (S^{-1}C^{-1}\Lambda_- CS)U_R \\ &= \left(R^{-1}\frac{\Lambda_+ + |\Lambda|}{2}R\right)U_L + \left(R^{-1}\frac{\Lambda_- + |\Lambda|}{2}R\right)U_R \\ &= (R^{-1}\Lambda R)\frac{U_L + U_R}{2} + (R^{-1}|\Lambda|R)\frac{U_L - U_R}{2} \\ &= A'\left(\frac{U_L + U_R}{2}\right) + \frac{1}{2}|A'|(U_L - U_R) \end{aligned}$$

where the first term is the symmetric, non-dissipative portion and the second term is the upwind, dissipative portion of the modified Steger-Warming flux. This now allows for the evaluation of each portion separately by replacing the symmetric portion with the non-dissipative kinetic energy consistent flux which is a central scheme using unbiased data obtained at the face [44]. To add dissipation in this work, the flux at the face uses the upwind biasing of the previously introduced dissipative flux formulation multiplied by a constant, α, computed by a shock sensor. The flux at the face then takes the following form:

$$F'_f = F'_{f,\text{central}} - \alpha\frac{1}{2}(R^{-1}|\Lambda|R)_f(U_L - U_R) \tag{2.30}$$

In theory, the symmetric portion only has dispersive error and no dissipation which is ideal for problems involving the study of wave propagation phenomena present in boundary layer transition and turbulence simulations [2]. Formally, the central scheme is second-order accurate in space. To achieve higher-order accuracy, the symmetric, non-dissipative portion uses a stencil and weights to acquire higher-order local fluxes. This requires a quality mesh (unstructured) that is smoothly varying since gradients

[2]The study of boundary layer transition phenomena requires that the amount of numerical dissipation and dispersion error present in the solution is minimized to obtain a quality solution and maintain accuracy

are used to extrapolate cell-centered data, at which interpolated data is used to construct the flux at the face. For example, consider gradient reconstruction for a grid with minimal connectivity information where cell i only has access to neighboring cells. The variables at cells $i-1$ and $i+1$ are used to construct a flux with the a larger stencil by linearly combining the neighboring cell gradients and the local solution values:

$$\phi_f = w_1(\phi_i + \phi_{i+1}) + w_2(\nabla\phi_i \cdot \Delta\mathbf{x}_{f,i} + \nabla\phi_{i+1} \cdot \Delta\mathbf{x}_{f,i+1}) \tag{2.31}$$

where $\mathbf{x}_{f,i}$ is the spacing from the cell-center (i) to the face center (f) where the direction points from i to f. The weight coefficients of w_1 and w_2 gives different modified wavenumber properties. By having access to the connectivity of a larger data set, the stencil can be extended to construct higher-order schemes. In this work, fourth-order and sixth-order gradient based interpolation can be achieved [45],

$$\phi_{i+1/2} = \frac{(\phi_i + \phi_{i+1})}{2} + \frac{(\delta\phi_i + \delta\phi_{i+1})}{3} \tag{2.32}$$

and

$$\phi_{i+1/2} = \frac{(\phi_i + \phi_{i+1})}{2} + \frac{8(\delta\phi_i + \delta\phi_{i+1})}{15} - \frac{(\delta\phi_{i-1} + \delta\phi_{i+2})}{45} \tag{2.33}$$

where $\delta\phi_i$ corresponds to the dot product of the gradient of ϕ in cell i and the vector from the cell center of i to the face center (f) at $i+1/2$. Bartkowicz [46] demonstrated that the method exhibits fourth-order and sixth-order convergence by comparing the error versus the number of grid points for a 1-D domain when convecting a density pulse. Additionally, the importance of using a non-dissipative flux versus the second-order TVD MUSCL scheme is exploited where the density gradients diffuse from the exact solution. Also, Subbareddy demonstrated that the sixth-order fluxes resolve the

relevant energy spectrum needed to acquire statistic flow quantities for a turbulent flat plate boundary layer [47]. In this work, sixth-order gradient based interpolation is used for the majority of the results. Fourth-order accurate gradient interpolation is used for a few calculations and will be clearly stated when used later on. The fourth-order scheme has proven to obtain adequate results for studying instabilities on BoLT in the past [11].

In general, α from Equation 2.30 should vary from zero in smooth areas of the solution and approach one near sharp gradients. Ideally, a calculation would set α to zero in smooth regions of the flow so that the solution contains minimal numerical dissipation allowing for negligible wave damping properties. In fact, zero wave damping is achieved when setting α to zero with the formulation when applied to a 1-D grid and assuming that the grid and temporal scheme respect the spatio-temporal scales. However, for non-ideal grids of complex shapes, it may be impossible to obtained a converged solution or the amount of dispersion error can lead to significant cell-to-cell oscillations near sharp gradients. Therefore, for practical applications a lower bound for α almost always has to be set from either 0.001 to as high as 0.3, and is dependent on the grid and flow structures present. However, this can be detrimental to resolving high wavenumber content especially when propagating disturbances the length of a domain for transition studies.

In the case of wave propagation problems, which typically involves introducing some type of flow disturbance to a DNS calculation, it is a combination of the grid resolution and numerical scheme that dictates the spatial wave damping characteristics. For a coarse grid, the Nyquist frequency of the grid dictates the maximum resolvable wavenumber. On the contrary, for a very fine grid, the numerical scheme may significantly dampen higher frequency waves that convect through a domain. For example, consider a 1-D domain where slow acoustic waves are convected at a single frequency through the domain. The simulations utilize the sixth-order spatial

fluxes and vary the dissipative portion of the inviscid flux with α. Furthermore, a sufficiently low time step with explicit RK3 time integration is used so that wave damping is only associated with the spatial scheme. Based on theory for a slow acoustic planar wave with a wave length of λ, the perturbations depend upon the characteristic wavenumber [19, 48]:

$$p' = Ae^{i(kx-\omega t)}$$

$$\text{where, } k = \frac{\omega}{u-c} \text{ and } \omega = 2\pi f$$

$$\begin{pmatrix} \rho' \\ u' \\ T' \end{pmatrix} = \begin{pmatrix} \frac{1}{a_\infty^2} \\ \frac{-1}{\rho_\infty a_\infty} \\ \frac{(\gamma-1)T_\infty}{\rho_\infty a_\infty^2} \end{pmatrix} p' \tag{2.34}$$

where A is the disturbance amplitude, p' is the pressure perturbation amplitude, and ω is the angular frequency. The pressure perturbation takes the form of a plane sinusoidal wave and is applied at the inflow. The density and temperature adjust to the pressure disturbance based on the linearized isentropic relations thus satisfying the acoustic-mode.

Figure 2.3 shows how various resolutions resolve a single 800 kHz wave propagating the length of a 1 meter domain. The horizontal axis of the plots in Figure 2.3 is the distance that a disturbance travels. The vertical axis is the absolute value of the density perturbation relative to the freestream value plotted on a log-scale. One can clearly see that the magnitude of the wave amplitude drops dramatically when using a resolution of 12 points per wavelength (ppw). This is because the 1-D grid was purposely constructed to have a spacing that is near the limit of the high frequency sinusoidal wave propagating the length of the domain with the specified value of α. Considering when $\alpha = 0.01$, as denoted by the green line of a), the amplitude

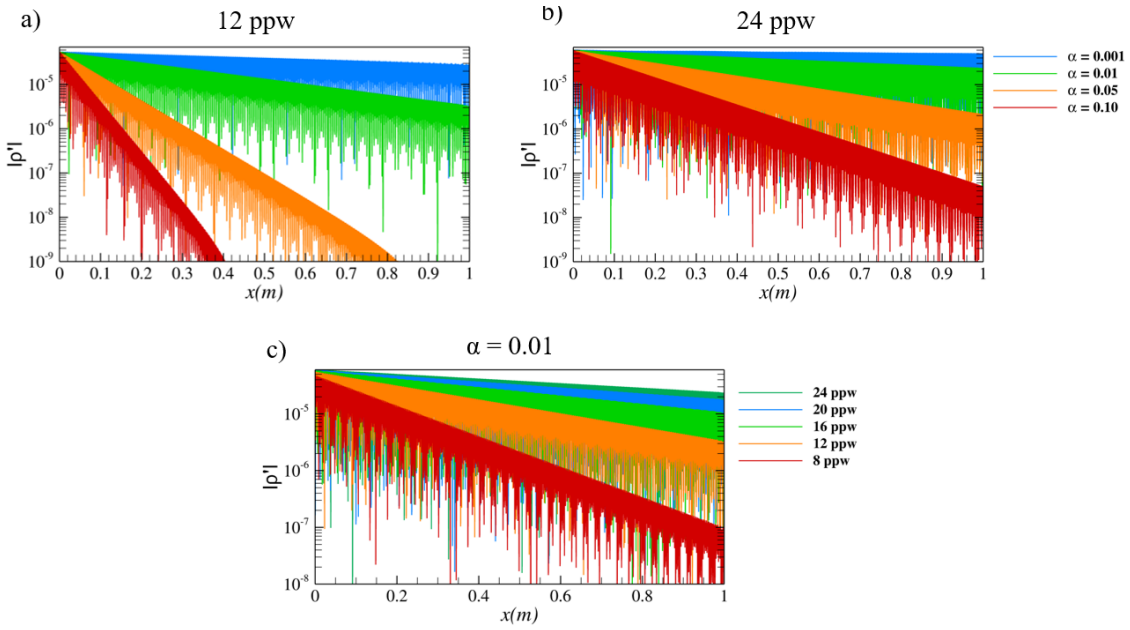

Figure 2.3: Planar acoustic wave damping of an 800 kHz slow acoustic wave on a 1-D domain. a) shows a grid with 12 points per wavelength (ppw) and b) shows a grid with 24 points per wavelength with varying values of α. Whereas, c) shows the effects of varying grid resolution with $\alpha = 0.01$

drops nearly an order of magnitude. This is nearly equivalent to setting $\alpha = 0.05$ with double the grid resolution of 24 ppw as seen in b) denoted by the orange line. From experience, 16 points per wavelength (based on the freestream conditions) for the maximum desirable frequency of a slow acoustic wave is sufficient for transition studies in a given direction when using $\alpha = 0.01$. Recall, for practical transition studies this depends upon the flow conditions, initial wave amplitude, three-dimensional grid stretching, distance that disturbances must travel to excite boundary layer instabilities, and location at which disturbances are introduced which will be discussed in later chapters. This can make it challenging if one is interested in quantifying an initial amplitude based approach for transition prediction using DNS.

2.3.4 Shock Sensors

Many numerical methods utilize so called shock sensors to identify regions of the flow which tune numerical dissipation to particular regions of a flow having sharp gradients to maintain numerical stability. The design of a well performing shock sensors continues to remain an open area of research for many numerical methods. As a result, a number of shock sensors have been introduced in the literature. In some cases, a poor choice of shock sensor will cause a high-order, low-dissipation method to appear dissipative when it may be the sensor that is limiting the potential of the scheme to obtain higher wavenumber resolution in crucial regions of the flow field. However, many researchers fail to show how well a particular shock sensor actually identifies regions to apply numerical dissipation. Typically, a comparison of solutions are shown but that is not effective for a general problem. This can lead to a misconceptions that certain shock sensors are claimed to be effective when the shock sensor in fact causes more numerical issues. Or, they can be more dissipative for a particular problem than what the user may or may not admit. This of course is problem dependent and must be explored for each case since even a slight amount of tuning is typically required even for a well performing shock sensor. An effective shock sensor for wave propagation transition studies must be only active where numerical stability is needed, inactive in smooth regions of the flow where the high-order method is applied, and avoid producing large amplitude numerical noise due to significant temporal variations. Most shock sensors that are commonly used in the literature take into account flow gradients of one or more primitive flow variables. One example is the shock sensor by Harten [49] which considered gradients of density and has a few variations. Also, a shock sensor considering pressure gradients was introduced by Jameson et al. [50]. Other physics-based sensors have been introduced which detect sharp gradients for subgrid-scale features for unsteady turbulent flows of high-order numerical methods. An overview of many shock sensors commonly used in the

literature have been summarized by Pirozzoli [51]. Personal experience has found that shock sensors which rely solely on gradients of a single primitive flow variable tend to be very dissipative and tedious to tune. Often they require to be combined with another shock sensor such as what was performed by Subbareddy and Candler [47]. Nonetheless, one of the most widely cited is the shock sensor by Ducros et al. [52] which is based on a dilatation to vorticity ratio.

$$\alpha_D = \frac{(\nabla \cdot \mathbf{u})^2}{(\nabla \cdot \mathbf{u})^2 + (\nabla \times \mathbf{u})^2 + \epsilon} \tag{2.35}$$

This formulation on its own does not account well for flow fields where the solenoidal (vorticity) component is small and dilatation (acoustic) component is large for a general problem with shock waves. Furthermore, the sensor identifies regions of expansion as well which can be problematic since numerical dissipation can be added in regions even if a dissipative scheme is not needed. To isolate regions of compression by neglecting the expansion portion, Larsson et al. [53] introduced a variation taking the following form,

$$\alpha_L = \frac{-(\nabla \cdot \mathbf{u})}{\max\left(C_1|\nabla \times \mathbf{u}|, C_2\left[a/\sqrt[3]{h}\right]\right)} \tag{2.36}$$

where C_1 and C_2 are tuning coefficients, a is the local speed of sound, and h is the cell volume. Quinlan et al. [54] introduced a variation which entailed tuning of the coefficients and setting bounds $\alpha_L \in [0, 1]$. This shock sensor along with the others mentioned previously are all computed at each time step. As a consequence, they are susceptible to potentially generating large amplitude numerical noise on non-shock aligned grids with stationary shocks. Therefore, Knutson et al. [55] introduced a time-independent shock sensor which based on the divergence of velocity. This first involves computing an initial solution with upwind fluxes, storing the dilatation

field of an initial solution, and setting α to be fixed in time with a user defined dilatation value based on the initial solution. This works well for solutions where sharp gradients remain relatively stationary such as for steady state solutions or transition simulations which involve excitation of very small amplitude perturbations post-shock to excite boundary layer instabilities. However, this approach can lead to a number of numerical issues if small amplitude disturbances are passed through shock waves or if regions of separation exist within the domain. Therefore, a shock sensor capable of handling a wide variety of unsteady, compressible flow problems is desirable since freestream disturbances are introduced to solutions later in this thesis.

Knowing that the value of α from Equation 2.30 can significantly impact the amount of numerical damping of high wavenumber content as seen from the previous section, it is desirable to tune the numerical dissipation with the use of a shock sensor. The desire is to activate the dissipative portion of the flux near sharp gradients and minimize the numerical dissipation everywhere when propagating waves for transition studies. In practice, it is straightforward to build accurate, local shock sensors, but may be tedious if fine tuning is demanded by the flow state which requires a high-order, low-dissipation method. In order to effectively construct and show how well a shock sensor performs, one must quantify the spatial location of numerical dissipation. This will help to understand where numerical dissipation is highest, and ensure that the shock sensor does not flicker (intermittently change in time) so as to not introduce aphysical numerical oscillations to the solution for unsteady, compressible flow problems. In the case of transition studies, it is possible for a shock sensor to introduce an unknown amount of forcing which can then invalidate a result since the amount of error can reach the same order of magnitude of small amplitude perturbations or corrupt results if the error growth is induced by numerical oscillations of the error which can then be amplified by boundary layer instabilities. This may happen if a shock sensor flickers near the bow shock wave and produce aphysical receptiv-

ity mechanisms which could then enter the boundary layer and excite instabilities. Therefore to understand the performance of a given shock sensor in the quantitative sense, the shock sensor value, α, is plotted in space for a number of test cases to confirm that relevant compressible flow phenomena can be simulated. However, since the shock sensor is computed at each cell face and depends on the direction of the flux, the cell-centered value is plotted by taking the average of all the surrounding cell faces for a given cell for visualization purposes.

2D Forward Facing Step

The first example is a 2D forward facing step case to investigate the tuning of a compression based sensor with respect to the divergence of velocity. The spatial scheme uses the sixth-order spatial fluxes and RK3 explicit time integration with a sufficiently low time step (CFL ≈ 0.75). The flow setup and conditions can be found in the paper by Hendrickson et al. [56] where the domain contains 1.344×10^6 cells ($N_x = 800 \times N_y = 2000 \times N_z = 1$). For demonstration, the Ducros sensor and compression based sensor are simulated with and without the divergence filtering step. The base compression shock sensor is a simple modification to the sensor by Larsson taking the following form,

$$\alpha_c = \frac{-\left(\nabla \cdot \mathbf{u}\right)}{\left[1.5|\nabla \times \mathbf{u}| + 0.05a/\sqrt[3]{h}\right]} \tag{2.37}$$

The purpose of writing it in this way will be made clear in the next chapter where a simple tuning is applied for boundary layer transition problems. For now, a filtering step is applied for tuning to the base shock sensors of the Ducros sensor and the compression-based sensor values by using the divergence of velocity, similar to

Hendrickson et al. [56]:

$$\beta = \frac{(\nabla \cdot \mathbf{u})^2}{(\nabla \cdot \mathbf{u})^2 + \left(\nu \frac{|\mathbf{u}|}{h}\right)^2 + \epsilon} \tag{2.38}$$

where ν is the tuning parameter and is set to 0.005. ϵ is a very small value to avoid division by zero. By using the base shock sensor value, α_D and α_c, from Equations 2.35 & 2.37 and the dilatation filter from Equation 2.38, the filtered sensor values are obtained,

$$\alpha = [\max((\alpha_{base} - \phi), 0)]\,\beta + \theta \tag{2.39}$$

where α_{base} is the base shock sensor value and θ is a user defined parameter that sets the minimum dissipation factor globally. For the current computations, θ is set to 0.01 in order to maintain numerical stability. This means that an upper and lower bound is set for $\alpha \in [0.01, 1]$.

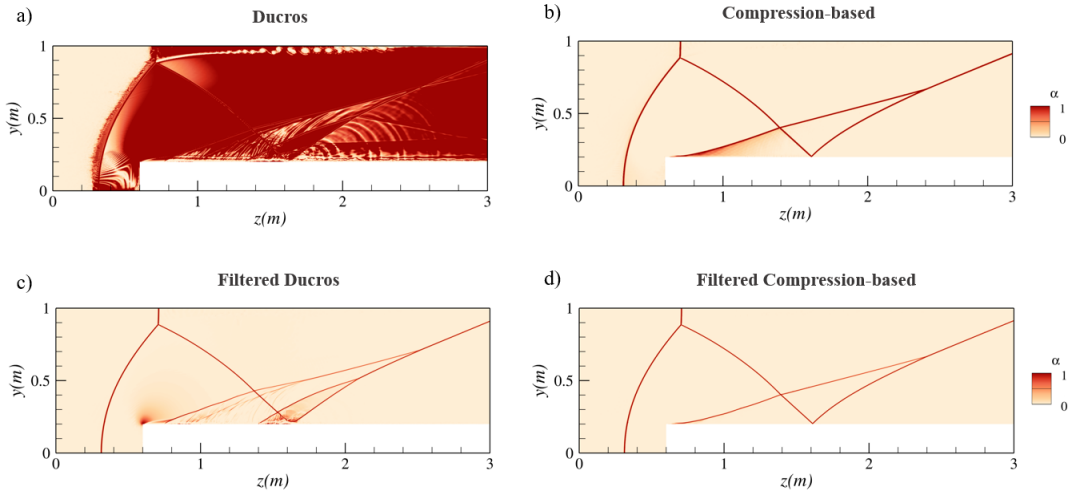

Figure 2.4: Comparison of the sensor values for a) Ducros sensor, b) Compression-based sensor, c) Filtered Ducros sensor, and d) Filtered Compression-based sensor

Figure 2.4 clearly shows the Ducros sensor on its own performs quite poorly since

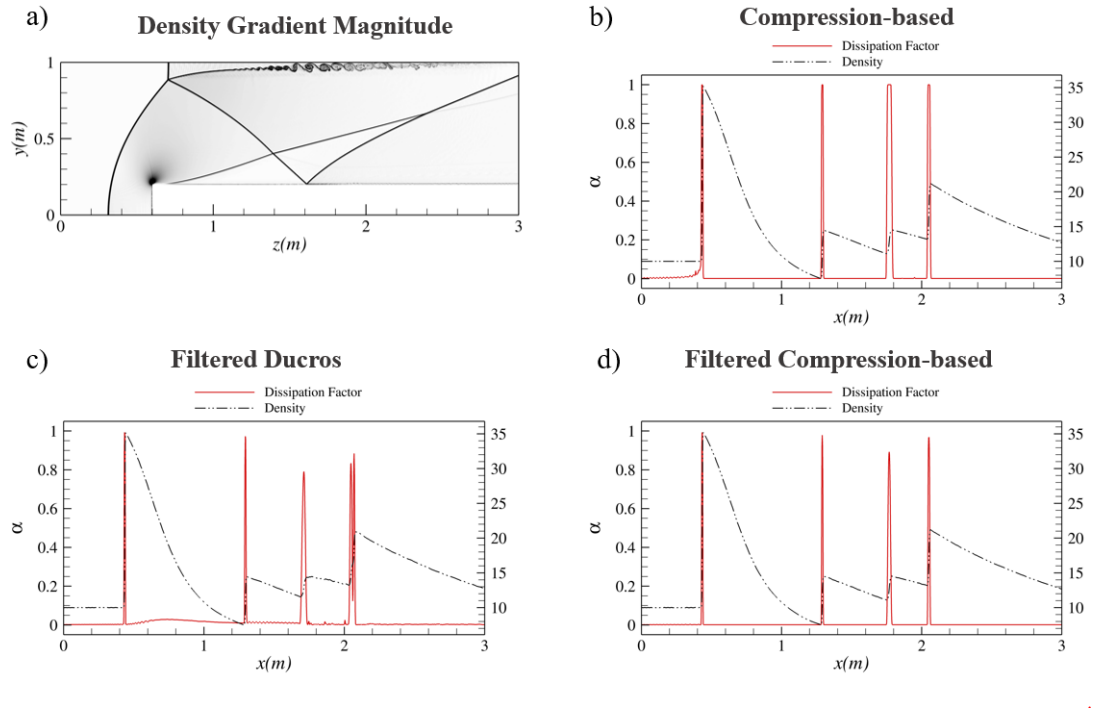

Figure 2.5: Line extraction comparison at $y = 0.5$ m where the solid, red line denotes the value of α and the dashed, black line denotes the density. The density gradient magnitude from the solution obtained with the compression-based sensor is shown in the upper left.

the dissipative portion of the inviscid flux is nearly set to one everywhere and therefore should never be solely used without tuning for wave propagation problems. Not to mention it flickers near the bow shock wave developing in front of the forward facing step. Whereas, the filtering step helps to correct this by tuning the sensor with the help of the instantaneous velocity divergence field. The compression-based shock sensor performs very well even without the filtering step. Nearly identical results were obtained with the Larsson sensor and variation introduced by Quinlan et al. [54] but are not shown for brevity. Upon closer inspection, a line extraction taken at y = 0.5 m shows a quantitative comparison. One can see that the filtered Ducros has a small increase in α behind the strong bow shock between $x = 0.5$ m and 1 m due to a region of expansion. This is not the case for the compression-based sensor. Also,

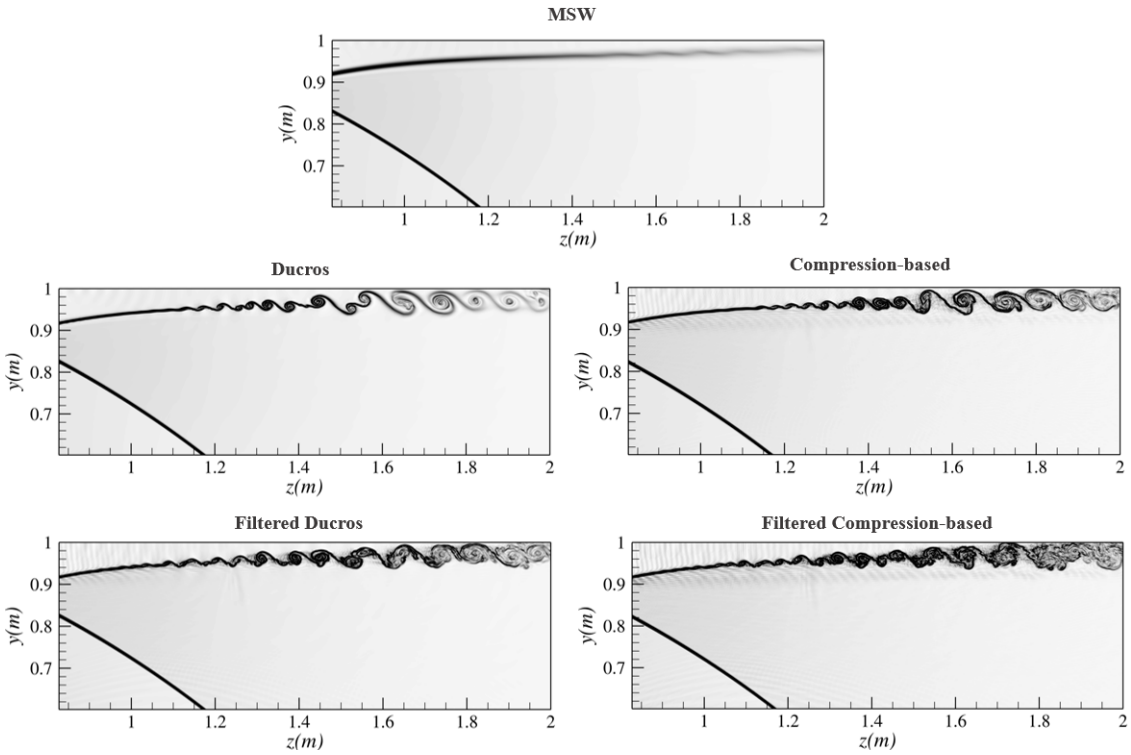

Figure 2.6: Comparison of density gradient magnitude near the shear layer of the shock-shock interaction producing a Kelvin-Helmholtz instability.

notice that the compression-based sensor adds dissipation just in front of the shock. This is because the current grid is not aligned with the bow shock and so numerical error is generated upstream of the shock resulting in the generation of numerical oscillations. The compression-based shock sensor dampens the numerically generated oscillations while the velocity divergence filter does not add enough dissipation near the shock and so the oscillations could potentially lead to numerical issues in practice if the filtering step is used in combination with a non-ideal grid. The only way to eliminate the numerical error with the introduced numerical method is to align the grid with the bow shock which will be discussed later. Lastly, Figure 2.7 shows that a shock-shock interaction near the top portion of the domain produces an unstable shear layer producing a Kelvin-Helmholtz instability. Notice that the resolved structures

are sensitive to the shock sensor used where a Modified Steger-Warming solution is shown for reference to demonstrate that by solely using an upwind biased dissipative scheme smooths out the density gradients and significantly attenuates the instability.

2D Shock-bubble Interaction

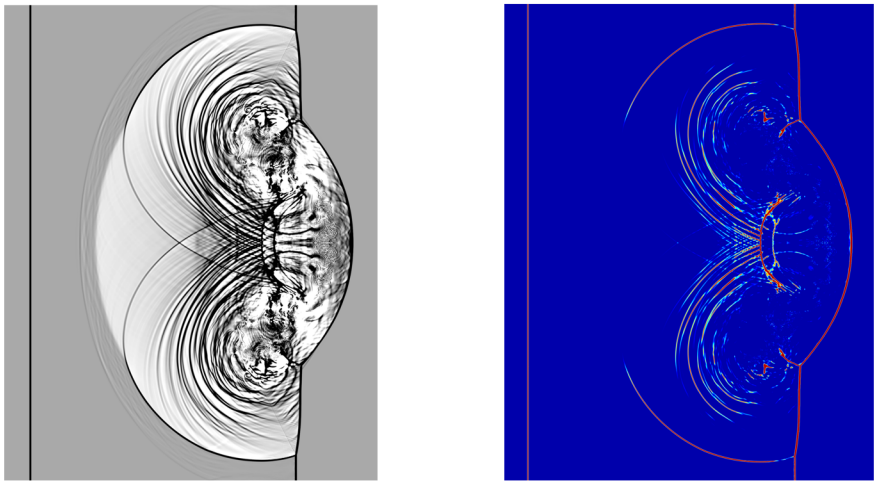

Figure 2.7: 2D shock-bubble interaction test case showing the velocity dilatation on the left (black compression and white as expansion) and the cell averaged value, α, of the shock sensor at the same time instance (right). Red is fully active and the blue denotes the lower bound of $\alpha = 0.2$.

The next problem considered for testing the compression-based shock sensor is a 2D shock-bubble interaction where a normal shock passes through a region of low density. The flow setup and initial conditions can be found at the following reference [57]. The total cell count is 7.68×10^6 cells ($N_x = 4800 \times N_y = 1600 \times N_z = 1$). The sixth-order inviscid flux is used along with explicit RK3 time integration. The solution is advanced in time to 0.2 seconds using a time step of $\Delta t = 1 \times 10^{-5}$ seconds corresponding to a CFL of approximately 0.33 for the grid used. The convecting normal shock passes over the low density region resulting in a spatio-temporal evolution of the shock front. As the incident shock passes over the bubble, a spectrum of acous-

tic waves are generated post-shock along with the development of Richtmyer-Meshkov instabilities and transmitted shock waves. The flow state contains very sharp gradients and as a result a lower bound was increased for numerical stability. Nonetheless, the shock sensor does an excellent job of identifying regions of high dilatation and numerical scheme is still capable in resolving small-scale vortical and acoustic waves.

2D Reimann Problem

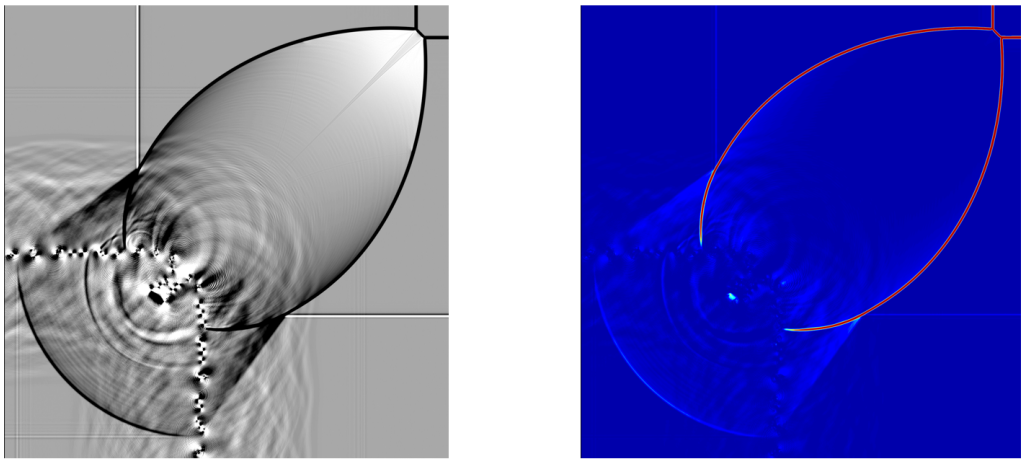

Figure 2.8: 2D Riemann problem example showing the velocity dilatation on the left (black compression and white as expansion) and the cell averaged value, α, of the shock sensor at the same time instance (right). Red is fully active and the blue denotes the lower bound of $\alpha = 0$.

The final inviscid flow problem is a 2D Riemann problem where the domain is initialized according to configuration 13 of Kurganov and Tadmor [58]. The initialization of four quadrants allows for inviscid shear layers to setup a shock triple point allowing for the generation of unstable shear layers when marching in time. The total cell count is 25.0×10^6 cells ($N_x = 5000 \times N_y = 5000 \times N_z = 1$). The sixth-order inviscid flux is used along with explicit RK3 time integration. The solution is advanced in time to 0.1 seconds with a time step of $\Delta t = 1 \times 10^{-5}$ seconds which corresponds to a CFL around 0.14. The black (compression) and white (expansion) colors of

the velocity divergence field of Figure 2.8 reveal the development of unsteady flow structures including unstable shear layers, propagating shock waves, acoustic waves, and vortical structures associated with a large Richtmyer-Meshkov instability. Notice that the acoustic waves are able to propagate with minimal amounts of damping near the unstable shear layers, along with a negligible amount of spurious acoustic wave generation near the normal shocks propagating through the flowfield.

Clearly the canonical test cases introduced showcase that a compression-based shock sensor with the numerical scheme performs quite well in identifying and applying dissipation for inviscid flow problems with shock waves and resolving hydrodynamic instabilities. This is meant to provide confidence that the shock sensor in combination with the numerical scheme is capable in capturing important physics of unsteady compressible flow problems with interacting acoustic and vortical structures in the presence of strong shock waves. This requires that the grid and time step respect the relevant spatio-temporal scales of the problem. The next step is to address how well the compression-based sensor performs for a realistic boundary layer transition problem when performing a DNS with the full Navier-Stokes equations. Furthermore, the relationship between spatial and temporal damping of boundary layer instabilities needs to be understood for a general problem. This will be investigated and discussed in the next chapter. Also, the tuning of the compression-based shock sensor used for transition studies will be introduced.

2.3.5 Shock Capturing

Recall, the formulation of shock capturing in this work has already been discussed where a characteristic based flux scheme is utilized by performing flux limiting with the use of eigenvalue limiters to ensure physically meaningful values are used for the flux calculation, slope limiters are used to obtain a second-order TVD MUSCL scheme, and the flux is smoothly varied between the original Steger-Warming flux and

the second-order MSW flux near strong shocks. As discussed with the low-dissipation flux scheme, a shock sensor is applied to help with tuning the dissipative portion of the inviscid flux. However, this is only a way to reduce the error and stabilize the solution and not necessarily a solution to eliminate the error completely. In order for the error to be minimized, the grids require alignment with discontinuities. For this reason, this work strictly utilizes hexahedral control volumes and carefully constructed grids to help with the alignment of the characteristics near sharp gradients. This is referred to in this work as grid tailoring and is meant to ensure the grid is aligned and approximately orthogonal at the bow shock. This is achieved by computing the maximum of the pressure gradient in the wall-normal direction to locate the bow shock of a converged solution on an initial grid, redistribute the grid points extending from the wall to the inflow, smooth along grid connected lines, and converge the improved solution on the tailored grid.

For complicated shock systems, it is inevitable that there will be some degree of misalignment of the grid with the shock waves at which the numerical method has to be relied upon. A potential solution is to use adaptive mesh refinement (AMR) or a shock-fitting approach for simulations of supersonic and hypersonic flows with the low-dissipation, high-order numerical flux reconstruction method to properly capture flow discontinuities. Shock fitting is an active area of code development and the extension to the unstructured, three dimensional numerical solver has not progressed to the application of the current work at the time of this writing. This is outside the scope of the current work because it requires great effort to extend shock-fitting to the unstructured, three-dimensional flow solver since the fluxes need to be arbitrarily rotated and aligned with the characteristic directions. Not to mention that the approach needs be able to scale well for grids on the order of $\mathcal{O} \sim 10^8$ thus requiring much attention related to the implementation itself. Higher-order numerical methods such as discontinuous Galerkin methods are capable of eliminating this issue entirely

when solving for PDEs governed by hyperbolic conservation laws by capturing sub-grid discontinuities. However, again, the scaling to practical applications requires much more efforts even after decades of development and investigations. Therefore, grid generation remains to be a tedious craft for users performing CFD. In some cases, a numerical method may not be able handle extreme grid stretching. Or, the numerical method may require grid improvements to be made by the user for obtaining a quality grid used for many hypersonic flow problems.

To demonstrate and help quantify the amount of error near the shock for an unaligned grid, a 2D cylinder in hypersonic crossflow is simulated. In theory, the enthalpy is a conserved variable and therefore it should remain constant across the bow shock in this case. The grid was arbitrarily generated such that a grid generation software was not used to enforce any type of orthogonality parameters and the cells were simply distributed with a constant spacing based on the domain dimensions. The cylinder wall has a radius of 0.4 m and the initial grid contains $10,000$ total cells, where 100 cells are used in both the wall normal and axial directions. The freestream flow conditions are: $\rho_\infty = 0.0895$ kg/m^3, $T_\infty = 217$ K, $U_\infty = 2363$ m/s which results in a freestream Mach number of 8. The inflow and outflow boundary conditions assumes supersonic flow. An isothermal wall is assumed by imposing a constant temperature of 400 K. The solution is obtained with the modified Steger-Warming flux scheme and integrated in time to a converged steady-state. Figure 2.9 shows the solutions obtained on the following grids: a baseline grid, a grid with shock alignment, a tailored grid with 1 level of AMR, and a tailored grid with 3 levels of AMR. Adaptive Mesh Refinement (AMR) [59, 60] was performed by tagging cells which contain a velocity divergence value within a specified range. The local refinement for each level of AMR is equivalent to doubling the grid size in every direction.

A comparison of the solutions from Figure 2.9a) and 2.9b) reveals that the mag-

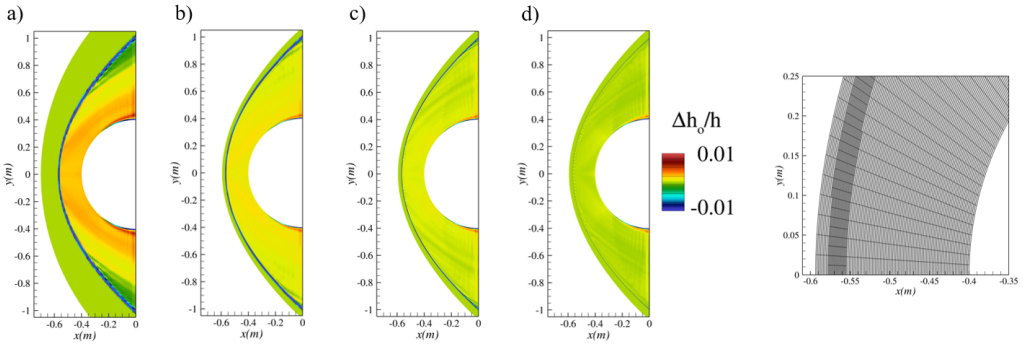

Figure 2.9: Cylinder in crossflow showing contours of enthalpy change relative to the freestream enthalpy value and the difference is normalized by the freestream enthalpy. a) non-aligned grid, b) tailored grid, c) tailored grid with 1 level of AMR, and d) tailored grid with 3 levels of AMR. The right plot shows the grid after 1 level of AMR where cells are identified based on the divergence of velocity.

nitude and distribution of the of the error changes significantly. Furthermore, grid refinement near the bow shock, as observed in 2.9c) and 2.9d), demonstrates that the magnitude of the error drops even though the distribution of the error does not change as significantly with increasing grid refinement. This is because the resulting error is dependent on the grid resolution of the flow features approximated discretely and the alignment of the characteristics with the resolved flow features. The error near the shock when the grid is not aligned is attributed to the fact that the numerical method used in this work and almost all other CFD codes are derived from 1-D characteristic methods. These methods can lose accuracy if not properly extended to three-dimensions to retain the same physical characteristics aligned with the discrete mesh. Therefore, the numerical method requires that the mesh be consistent with the original derivation such that the directions of the characteristics of a problem are aligned. Additionally, refinement allows for the numerical flux to become more oriented such that the flux calculation approaches consistency with the original flux formulation. Therefore, grid alignment and orthogonality is important for a variety of problems containing sharp gradients in practice, including the cases of this thesis.

2.4 Viscous Fluxes

As mentioned previously, the viscous fluxes are elliptical meaning that the diffusive terms of the governing equations, such as shear stress and heat flux, to not require flux vector splitting like the inviscid fluxes. The most accurate but expensive way would be to store the local stencil for each face and compute the gradients using the local stencil at each time step. Instead, for improved computational efficiency, the gradients for computing the viscous fluxes can be discretized in a relatively simpler manner with a central scheme. In order to do this accurately, the viscous fluxes are evaluated with gradients at the faces derived from the cell-centered values. This is similar to how the cell-centered gradients were computed from the high-order, low-dissipation inviscid flux calculation. A summary of the methods for computing the cell-centered gradients of the viscous fluxes are described by Drayna [61]. However, the method which balances computational-efficiency and accuracy for problems containing cells with high-aspect ratios near the wall that are required to fully resolve boundary layers in this work is the weighted least squares method. This approach solves for the gradient reconstruction by minimizing the summation of the squares of the gradients between the cell evaluated and the neighboring cells. An approximation of the weights is obtained to acquire second-order accuracy as first described by Bartkowicz [46].

After constructing the gradients at the cell-centers, the gradients are then interpolated to the face for the viscous flux calculation. If the gradients were simply averaged results in an inaccurate viscous flux due to improper discretization. Instead, the flux is calculated using a deferred correction method to obtain the face centered gradient, $\nabla\phi_f$, at face, $i+1/2$. This involves decomposing the gradient at the face into normal and tangential components,

$$\nabla\phi_f = (\nabla\phi_f)_N + (\nabla\phi_f)_T$$
$$\nabla\phi_f = (\nabla\phi_f \cdot \hat{n})\hat{n} + (\nabla\phi_f - (\nabla\phi_f \cdot \hat{n})\hat{n})$$

Since the grids used are smoothly varying, the components obtained with a face normal unit vector are equivalent to the components defined by using a unit normal vector, $\hat{e}$, that points from the cell centroid at i to the cell centroid at $i+1$. The normal component is then calculated with a second-order compact stencil,

$$(\nabla\phi_f)_N \approx \nabla\phi_f \cdot \hat{e} = \frac{\phi_{i+1} - \phi_i}{\Delta h_{i,i+1}}$$

where $\Delta h_{i,i+1}$ is distance between cell centroids i and $i+1$. Similarly, the tangential component is computed with $\hat{e}$ with a simple averaging of the cell-centered gradients,

$$(\nabla\phi_f)_T \approx \frac{\nabla\phi_{i+1} + \nabla\phi_i}{2} - \left(\frac{\nabla\phi_{i+1} + \nabla\phi_i}{2} \cdot \hat{e}\right)\hat{e}$$

The deferred correction gradient at face $i+1/2$ is then,

$$\widetilde{\nabla\phi_f} = \frac{\nabla\phi_{i+1} + \nabla\phi_i}{2} + \left(\frac{\phi_{i+1} - \phi_i}{\Delta h_{i,i+1}} - \frac{\nabla\phi_{i+1} + \nabla\phi_i}{2} \cdot \hat{e}\right)\hat{e} \tag{2.40}$$

2.5 Time Integration

The discrete system of equations that are solved requires a time advancement method to acquire the intermediate states to reach the final state. The two classifications for time advancement schemes are explicit and implicit time integration methods. The unsteady cases performed prior to this section were obtained with explicit time integration. Whereas, the results sections of this thesis strictly utilize high-order implicit time integration. The purpose of this will be discussed in the following sections and demonstrated for boundary layer transition in the next chapter.

2.5.1 Explicit Methods

From Equation 2.12, a discrete representation of the time derivative with respect to the state vector is,

$$\frac{\partial U}{\partial t} = \frac{U^{n+1} - U^n}{\Delta t} + \mathcal{O}(\Delta t) = -\frac{1}{V}\sum_f (F_f^n S_f) \tag{2.41}$$

where the current time level is denoted as n and the time step is Δt. The truncation error reaches first-order accuracy when advancing in time by solving for U^{n+1}. This particular explicit method is conditionally stable for a numerical solution which does not exponentially amplify numerical error. This is because numerical stability for this method contains an upper limit on the time step that is restricted by the local grid spacing and convective time scales for a problem. A simple stability analysis on a 1-D domain shows that the maximum stable time step must satisfy the following inequality,

$$\Delta t \leq \frac{\Delta x}{|u'| + a}$$

where the grid spacing is Δx and the maximum characteristic wave speed is $|u'| + a$ dictated by the local fluid velocity and sound speed. This is owed to the fact that the scheme becomes unstable if information propagates further than one cell per time step due to the convective time scale, $\sigma_{conv} \sim \Delta x/(|u'| + a)$. Based on this notion, the ratio of the time step taken to the explicit time step is referred to as the Courant-Fredericks-Lewy (CFL) number,

$$\text{CFL} = \frac{\Delta t(|u'| + a)}{\Delta x}$$

and is often used to define the numerical stability for explicit methods which implies that the scheme is stable when a CFL equal to or less than one is imposed by the time step. For practical cases using the full Navier-Stokes equation, the numerical stability can require that the CFL be much lower than one to enforce numerical stability. This is related to the viscous time scales, $\sigma_{visc} \sim \Delta x^2/\nu$, for a case where the physics may limit the numerical stability of the problem.

The Runge-Kutta explicit time advancement methods are capable in achieving excellent temporal accuracy with minimum dissipation and dispersive error when using a very low time step. Additionally, the methods require very little memory storage allowing for codes to acquire less time per iteration. However, the largest drawback is the limitations imposed by high Reynolds number flows related to the CFL condition for numerical stability. The simulations of this thesis require fine grid spacing to resolve boundary layer profiles and instabilities for a wide range of length scales for three-dimensional flow structures. This restricts the time step drastically if an explicit time integration scheme were used for the cases of this thesis since the time required to performed such calculations would not be practical. This is the primary reason which motivates the use of implicit time integration.

2.5.2 Implicit Methods

The most advantageous property of implicit time advancement over explicit is the ability to take large time steps and still maintain numerical stability. For this reason, implicit methods are ideal for obtaining converged steady-state flow solutions quickly. This is attributed to the fact that when the time derivatives of the governing equations are zero, it is most efficient to take the largest time step possible. Although, this requires that the time step respects the convective length scales of the problem which the user has to be able to recognize since the improved numerical stability with a large time step can increase the dissipative error contributed by the temporal discretization.

For example, in the case of a re-entry capsule grid the high aspect ratio due to near wall clustering required for resolving the boundary layer may be stable with a CFL number on the order of $\mathcal{O} \sim 10^4$ but the gradients in the wake will be diffused thus requiring the user to lower the time step in order to resolve the convective length scales of the problem. In the case of an unsteady flow simulations, the time accuracy needs to ensure that the dissipative error is minimized. For this reason, explicit time integration is strictly utilized in the literature to ensure the dissipative error does not adversely affect the solution quality for turbulent boundary layer problems. As preluded to earlier, the restrictive stable time step imposed by explicit methods would require for some cases in this thesis to have prohibitively long run times. As such, a higher-order implicit method is used for the boundary layer transition results of this thesis while maintaining time accuracy in regions of the flow where the timestep is less than the local convective and viscous time scales. Therefore, a semi-discrete representation of the fully implicit system takes the following form,

$$\frac{\partial U}{\partial t} = -\frac{1}{V}\sum_{f}(F_f^{n+1}S_f) \tag{2.42}$$

2.5.3 Solution of Linear System

To obtain the inviscid flux at a future time level, $n+1$, a linearization of the fluxes in time is performed by using flux vector splitting and including the inviscid flux Jacobian,

$$F_I'^{n+1} = F_I'^{n} + \frac{\partial F_I'^{n}}{\partial U}(U^{n+1} - U^n) + \mathcal{O}(\Delta t^2) \tag{2.43}$$

where $A'^n = \frac{\partial F_I'^n}{\partial U}$ is the inviscid flux Jacobian and the explicit update, $\delta U^n = U^{n+1} - U^n$, is first-order accurate in time, $\mathcal{O}(\Delta t)$, even though the linearization error term

is $\mathcal{O}(\Delta t^2)$. For higher-order implicit time integration, we can address the partial derivative in time and approximate it with a generalized implicit scheme,

$$\delta U^n = \frac{\theta \Delta t}{1+\phi}\frac{\partial}{\partial t}\delta U^n + \frac{\phi}{1+\phi}\delta U^{n-1} + \mathcal{O}\left[(\theta - \frac{1}{2} - \phi)\Delta t^2\right] \tag{2.44}$$

where the combination of θ and ϕ dictates the order of accuracy. For example, first-order Euler (or BDF1) implicit is obtain with $\theta = 1$ and $\phi = 0$, a scheme approximately equivalent to a Crank-Nicholson scheme can be obtained with $\theta = 1/2$ and $\phi = 0$, and second-order Euler method (or BDF2) with $\theta = 1$ and $\phi = 1/2$. As formulated, the numerical method will be first-order accurate in time because the flux linearization is first-order accurate even if a second-order accurate time integration scheme were used. This means that the implementations of the above methods into the unstructured solver would result in first-order accuracy because of the flux linearization. However, as will be discussed in the next section, if a nonlinear system solve is applied and converges, the order of accuracy of the numerical method will not depend upon the order of accuracy of the flux linearization. In this case, if a second-order accurate time integration method is used then the flux linearization will not reduce the order of accuracy in time.

As for the linearized viscous flux, it takes the following form:

$$F_v'^{n+1} = F_v'^{n} + (Q^{-1}MQ)\frac{\partial}{\partial n}(N\delta U^n)$$

where $\partial/\partial n$ is with respect to the face-normal directions and $N = \partial V/\partial U$ is the transformation of conservative to primitive flow variables. Q is the rotation matrix containing the set of orthogonal transformations used to transform the frame of reference from the cartesian coordinate system to the face normal and tangential directions with respect to the cell boundary. This is applied to simplify the form of the matrix operator denoted by M. The linearized fluxes being solved utilize the Modified

Steger-Warming flux formulation for the inviscid Jacobian and central scheme for the face-normal derivatives of the viscous fluxes is,

$$F_f'^{n+1} = F_f'^{n} + \left[A'_+ \delta U_i + A'_- \delta U_{i+1} + M'(\delta U_{i+1} - \delta U_i)\right]$$

where

$$M' = \frac{[Q^{-1}MQN]_f}{\Delta h_{i,i+1}}$$

and $\Delta h_{i,i+1}$ is the distance between cell-centers of the face evaluated. The implicit system of equations discretized with the first order Euler (BDF1) is written as,

$$\left[\frac{1}{\Delta t} I + \frac{1}{V_i}\sum_f (A'_+ - M')_f S_f\right] \delta U_i^n + \left[\frac{1}{V_i}\sum_f (A'_- + M')_f S_f \delta U_{i+1}^n\right] = -\frac{1}{V_i}\sum_f F_f'^{n} S_f$$

We commonly express the implicit system in the following compact form,

$$\tilde{A}^n \delta U^n = \tilde{R}^n \tag{2.45}$$

where $\tilde{A}^n$ is the implicit operator and $\tilde{R}^n$ is the explicit residual. The implicit boundary conditions are incorporated into the diagonal entries of implicit operator matrix [62, 63]. The linear system is constructed by forming a block diagonal matrix, $\tilde{A}^n$, and the block-diagonal system of equations is solved using an LU factorization and back-substitution. In this work, a relaxation method is used to solve the system of equations by moving the off-diagonal terms to the RHS,

$$(\tilde{A} - \tilde{B})^n \delta U^k = \tilde{R}^n - \tilde{B}^n \delta U^{k-1}$$

where the superscript k is a specified number relaxations steps and $\tilde{B}$ contain com-

ponents of $\tilde{A}$ which are relaxed. In this work, the linear system is solved either by full-matrix point relaxation (FMPR) [64] or data-parallel line relaxation (DPLR) [65] where the implementation is described in detail by Wright [66]. For solutions in this thesis, line relaxation is used for obtaining steady-state solutions and point relaxation is used for unsteady cases. A general problem typically requires a minimum of 4 relaxation sweeps, k_{max}, to converge the linear system. For cases in this thesis, the number of relaxation sweeps is set between 4 to 20 to ensure time accuracy depending on the problem. This is dictated by the convergence of the linear system.

Nonlinear System Solve

For unsteady flow problems, the error associated with the implicit time integration method is reduced and improved temporal accuracy is achieved with a Newton's method [67, 68]. This is essential for obtaining time accurate solutions for the cases of this thesis with the introduced numerical method, and requires that the nonlinear Navier-Stokes equations are discretized with respect to the time derivative. The description and implementation of the high-order implicit time integration was first described in detail by Knutson [69] and is summarized here. Considering a second-order backwards difference formulation of the time derivative with a constant timestep is as follows,

$$\frac{\partial U}{\partial t} = \frac{3U_i^{n+1} - 4U_i^n + U_i^{n-1}}{2\Delta t}$$

Therefore, we discretize the nonlinear system of equations as:

$$\frac{3U_i^* - 4U_i^n + U_i^{n-1}}{2\Delta t} + \mathscr{F}(U^*) = \mathscr{R}(U^*)$$

where $U*$ is obtained from the iterative, nonlinear system solve via Newton's method and $\mathscr{R}$ is the nonlinear residual. A similar form as Equation2.45 can be written as,

$$\left[\frac{\partial \mathscr{R}(U^{*,s})}{\partial U}\right] \delta U^{*,s} = -\mathscr{R}(U^{*,s}) \tag{2.46}$$

where s corresponds to the number of subiterations, k_{maxo}, of the nonlinear system solve and $\delta U^{*,s}$ is obtained from the linear system solve from Equation 2.46. $\delta U^{*,s}$ is obtained in this work using either line relaxation (DPLR) or point relaxation (FMPR) with a specified number of linear system solves k_{max}. The second-order backwards difference (BDF2) formulation in this work assumes a constant time step,

$$\left[\frac{3}{2\Delta t} I + \frac{\partial \mathscr{F}(U^{*,s})}{U}\right] \delta U^{*,s} = -\left[\frac{1}{2\Delta t}(3U^{*,s} - 4U^{n} + U^{n-1}) + \mathscr{F}(U^{*,s})\right] \tag{2.47}$$

By successfully converging the residual of both the linear and nonlinear system solves will allow the time advancement scheme to achieve higher-order time accuracy. This is because the temporal accuracy of the solution will no longer depend on the flux linearization or on the implicit approximations made to the Jacobian.

Knutson [69] demonstrated the time accuracy of various implicit and explicit methods by comparing the error versus the number of grid points for a 1-D domain with a convecting density pulse. It was established that the nonlinear system converges with 3 Newton iterations by comparing the L_2 error with the various time integration methods. In practice, experience has found that when the L_2-norm of the residual from the nonlinear system solve drops below 2 orders of magnitude relative to the initial value typically indicates that a solution is time accurate with nonlinear BDF2. This should be explored on a case-by-case basis at which the number of iterations of the Newton method may have to be increased. For all unsteady cases in this thesis, the nonlinear BDF2 time integration scheme is used with 3 Newton iterations unless otherwise stated.

Chapter 3

Computational Methodology

In this chapter, the framework used to study the BoLT-2 flowfield is introduced. This includes a review of disturbances sources that are likely to contribute transition in flight and the methods for simulating disturbances representative of various sources are briefly covered. For DNS, this is often referred to as "forcing" since small amplitude perturbations are introduced into the flowfield. The simulation methodology is discussed and demonstrated for a relatively simple test case to show how the simulation of instabilities are affected by the numerical methods introduced from the last chapter. The simulation approach used for the BoLT-2 cases is applied to an example to ensure the method can faithfully simulate transition through nonlinear breakdown. Additionally, modal analysis techniques applied to forced DNS datasets for quantifying spatio-temporal properties of boundary layer modes are introduced as well.

3.1 Simulation & Analysis Methodology

The computational methodology for studying boundary layer instabilities by performing DNS involves two separate components: simulation and analysis. The simulation approach involves solving the three-dimensional compressible Navier-Stokes equations

using the unstructured finite volume code, US3D, developed at the University of Minnesota. The numerical methods described in the previous chapter are applied in this chapter to demonstrate the application of the introduced numerical method for simulating boundary layer instabilities. Recall, DNS is chosen as the tool to simulate linear and nonlinear flow processes in order to accurately simulate potential mode interactions and secondary flow effects present in transition studies. Furthermore, the numerical method uses high-order gradient reconstruction for the spatial discretization of the convective terms with cell-centered spatial derivatives computed using a weighted least-squares method. The diffusive terms are calculated with a deferred correction approach by extrapolating cell-centered gradients to evaluate the fluxes at the faces. Low-dissipation inviscid fluxes are split into a non-dissipative symmetric component and a dissipative upwind component that is tuned to the instantaneous negative dilatation field with a shock sensor. The shock sensor allows for the tuning of numerical dissipation to maintain numerical stability. The low-dissipation, high-order fluxes are applied to regions of interest in order to resolve boundary layer instabilities and capture spatio-temporal scales of relevant flow structures. This allows for the study of how the nonlinearity contributes to the growth and decay of the perturbations introduced into the flowfield. The nonlinear BDF2 time integration method is used for implicit time advancement, and the linear system of equations is solved with line relaxation. The nonlinear system is converged by applying a Newton's method and solving the nonlinear set of equations to obtain time accurate solutions. The simulation methodology is briefly summarized as follows:

1. Compute a converged, steady-state solution using second-order upwind fluxes with first-order implicit time integration.

2. Perform grid tailoring to enforce shock-alignment to minimize potential numerical error.

3. Converge solution again with upwind fluxes to initialize solution for low-dissipation fluxes. Next, calculate the flow quantities from the initial solution and tune the shock sensor to desired length scales.

4. Compute a converged, steady state solution using the low-dissipation fluxes with numerical dissipation applied using the tuned shock sensor. Ensure the solution converges by assuming a laminar flow state before applying any type of forcing.

5. Alter boundary conditions representative of physical disturbances to apply forcing to the DNS solution. The unsteady case requires time accuracy using a high-order time integration. Typically about 2 to 3 convective flow times based on the freestream velocity and domain length are required to reach a statistically converged periodic state.

6. Restart the statistically converged unsteady state and collect flowfield statistics for analysis and post-processing.

The analysis involves extracting modes from the forced DNS datasets using modal decomposition techniques. This allows for the extraction of spatio-temporal information from flowfield snapshots generated by simulation. An overview of current modal analysis techniques with their applications are described in the papers by Taira et al. [32, 33]. Many of these analysis techniques are purely data-driven and typically apply modal decomposition to a dataset of a particular flow variable, or of an operator relevant to the system. The modal analysis techniques used for instability quantification will be described later in this chapter and includes: Streaming Total Dynamic Mode Decomposition (STDMD) and Spectral Proper Orthogonal Decomposition (SPOD)

3.2 Disturbance Sources

Under realistic flow conditions, such as wind tunnels or flight, there is a spectrum of potential disturbance sources present in the flowfield. Much progress has been made to more accurately characterize the disturbance environment in flight [19] and this continues to be an area of further research. In hypersonic wind tunnels, a boundary layer develops on the nozzle wall which can radiate acoustic noise and become significant if the boundary layer becomes turbulent. Therefore, hypersonic "quiet" wind tunnels aim to maintain a low noise level environment with the help of enforcing the nozzle wall boundary layer to remain laminar using a polished surface in combination with bleed slots. The disturbances sources of the environments under realistic operating conditions can contain small-amplitude perturbations which introduces a spectrum of waves. The waves are capable of propagating through the flowfield and lead to small-amplitude disturbances to pass through regions of instabilities that may amplify the disturbances by absorbing energy from the local flow state. This motivates the need to be able to properly characterize the disturbance environment that is representative of the actual flow state in order to serve as an initial condition for boundary layer instabilities. Therefore, a forcing function must be used in simulations to introduced small-amplitude perturbations to excite the physical flow state otherwise the transition process may never be realized even if the flow state is physically unstable. This requires that the error in the solution is minimized such that the fluctuations induced by the error are many orders of magnitude lower than the amplitudes of the physical disturbances. However, a proper model of the disturbance environment should be chosen if one is interested in simulating physically meaningful transition processes. Simulations in the past have used a number of models for introducing disturbances in order to excite and study boundary layer instabilities such as altering the boundary conditions meant to mimic the effects surface roughness, blowing/suction,

particulates, and wave forcing applied to flow quantities. The investigation of the flight relevant disturbances sources (flight orientation, surface roughness, variables wall temperatures, freestream turbulence, particulates, etc.) and the significance at flow conditions across the flight trajectory would require many studies. Therefore, the type of source used to study the transition process on BoLT-2 in this thesis is primarily freestream disturbances to mimic the effects of natural transition.

3.2.1 Distributed Surface Roughness

Steady forcing is when a condition that is imposed to act as a forcing mechanism to the flowfield is constant in time. Common examples of this is distributed roughness, discrete roughness elements, blowing/suction, variable wall temperatures, and many more. The examples mentioned are commonly studied since the steady mechanisms can alter the flow state and affect the onset of transition. This is typically attributed by tripping of the flow induced by the steady forcing mechanism leading to steady streamwise vortices that support instabilities. Furthermore, variable wall temperatures lead to non-uniform T_{wall}/T_{edge} ratios. It is well known that these steady forcing mechanisms can trigger instabilities near regions of high shear stresses. Thome et al. [70] have shown that variable wall temperatures using conjugate heat transfer [71] and distributed roughness can significantly alter the boundary layer flow state of BoLT. Specifically, it is the excitation of stationary crossflow instabilities which are attributed by distributed roughness and variable wall temperatures on BoLT. This motivates the investigation of transient growth mechanisms which takes the form of instabilities near streamwise vortices. Aside from this, recent work has shown that a dominant flow response for blunted nosetips of straight cone configurations appears in the form of low-frequency steady streamwise structures, forced by freestream noise and surface roughness [72]. For cone configurations, the amplification of this response scales with Reynolds number and nosetip bluntness. The non-modal growth

mechanism may exist near the leading edge of the BoLT-2 geometry, and could be a dominant response at the higher Reynolds numbers expected in flight. Therefore, both the flight and subscale configurations are simulated later on to investigate this mechanism and quantify the disturbance amplification spatially and temporally. In order to generate surface roughness, a random probability density function is used and meant to represent a degree of distributed roughness. Each wall node is perturbed using a random number between (-1,1) and multiplied by a maximum amplitude. Next, the displacement is smoothed along grid connected lines as described by Dinzl and Candler [26]. Previous work by Thome et al. [70] showed that different heating patterns are observed on the BoLT configuration by displacing grid nodes using various probability density functions to acquire different wavenumber distributions representative of surface roughness. Even though a normal distribution is used in this work and is not necessarily a physically accurate representation of a surface roughness distribution in practice, a non-biased wavenumber distribution allows for an exploratory look at the flowfield response without filtering out potentially relevant disturbances related to unforeseen instabilities.

3.2.2 Particulate-induced Transition

In more recent studies, particulates have been investigated to understand how boundary layers are receptive to particle-induced transition. Bushnell [73] hypothesized particles in the atmospheric could produce receptivity mechanisms that seed boundary layer instabilities that may cause transition in flight. This is postulated since a spectrum of particulates in the atmosphere may originate from vehicle exhaust gases, aerosols, statospheric clouds, and/or other environment origins [74]. Therefore, recent efforts have dedicated resources to quantifying particle sizes and number density distributions that exist in the atmosphere for high-speed vehicle flight [75]. The quantification of particle sizes and number densities is meant to help guide simulations

of particle-induced transition for realistic flight environments. For this reason, the measurements of atmospheric particulates were collected during the preparation of the BoLT-2 experiment by conducting a ballooning campaign using optical-particle-counters. Measurements were primarily collected at altitudes corresponding to the transition for the ascent and descent windows of the trajectory. It was found that the majority of the particles range below 1 μm but may be as large as 20 μm depending on the altitude. Therefore, particulate-induced transition is simulated at a conservative flight condition of the BoLT-2 trajectory using Lagrangian particle tracking and is located in Chapter 5 of this thesis to investigate if transition is possible by this source in simulation.

3.2.3 External Wave Forcing

As mentioned previously, another common disturbance source is freestream disturbances which can take the form of freestream turbulence or wind tunnel noise. There is an exhaustive amount of studies in the literature which have attempted to quantify the amplification of instabilities using various types of forcing to act as initial conditions for instabilities such as acoustic wavepackets, wall-normal momentum forcing, and freestream waves. Each of these sources can have their own characteristic receptivity mechanisms meaning that the disturbance sources can produce various combinations of characteristic waves caused by variations in entropy, vorticity, and fast and slow acoustic waves. Analytical solutions have been found for the various characteristic wave types as solutions to the linearized Euler equations. It was shown that any type of freestream disturbance can be expressed as a linear combination of the four characteristic wave types. Due to the wave speed, the slow acoustic wave is the most damped characteristic wave type in simulations. Therefore to demonstrate the performance of the spatial damping caused by changing the shock sensor parameters in this work, slow acoustic planar wave forcing is applied to a straight cone at a

flight condition. Additionally, a comparison between time advancement schemes are made to demonstrate the temporal damping of instabilities and importance of time accuracy required to simulate breakdown. This is meant to be a simple test case by forcing the flow state with the most physically unstable wave frequency according to PSE for second-mode instabilities. Therefore, the planar wave forcing at a single frequency is not meant to be representative of a realistic disturbance source and only for testing purposes.

A proper representation of a wind tunnel environment is needed to accurately replicate the transition process in simulation. This has to be understood since wind tunnels are often used to compare simulations and heavily utilized for vehicle design. Therefore, more recent efforts have been made to characterize the wind tunnel environment and elucidate on the relation between tunnel-noise effects and the receptivity process using DNS [76]. However, the logical question is how accurate does the forcing function have to be in order to obtain a response representative of natural transition? This of course is dependent on the instabilities supported by the boundary layer state. Not to mention, that the numerical method and grid will artificially filter very high frequency receptivity mechanisms of the particular forcing function. Nonetheless, a number of natural transition simulations share agreement with wind tunnel results. Work by Tufts et al. [77] performed forcing by utilizing a systematic approach of generating perturbations between the shock layer and the boundary layer. The approach obtained qualitative surface heating comparisons on a subscale HIFiRE-5 geometry between the DNS and conventional wind tunnel measurements. Additionally, Hader and Fasel [78] applied pressure disturbances near the inflow boundary and acquired results that matched well with experimental observations as well. Therefore, the stochastic pressure forcing applied to a flared cone similar to Hader and Fasel [18] is carried out in Chapter 4 to demonstrate that the numerical method used in this work is capable of simulating breakdown mechanisms on BoLT-2. Furthermore, a compar-

ison with experiments is meant to justify the numerical methodology for simulating transition.

3.3 Test Case: Straight Cone

First, the case considered for testing is a spherical-nose, 7 deg straight cone geometry that is representative of the HIFiRE-1 geometry. This case is meant to demonstrate the the amount of numerical damping of the numerical method in combination with the shock sensor used for simulating nonlinear breakdown. This is relevant in obtaining accurate disturbance amplification because propagating disturbances can absorb a large amount of energy from the local flow state. This means that the flow state evolves such that the solution can depart from what linear stability theory predicts when undergoing breakdown. Also, this example is meant to quantify temporal damping related to the implicit time integration for studying breakdown and demonstrate challenges related to quantifying disturbance amplification. This is a critical point to make since the locations at which flow transition of a particular boundary layer occurs is dictated by the actual disturbance amplitude and not necessarily on a relative disturbance amplification.

The grid was constructed to be two-dimensional to make direct comparison with the Parabolized Stability Equations (PSE) which assumes the boundary layer state remains linear [79]. A numerical sponge layer at the end of the domain is used to dampen any possibility of spurious oscillations that may arise and potentially propagate back upstream. The grid metrics are 300 wall normal cells, 11590 cells in the streamwise direction, and 1 cell in the azimuthal direction ($N_{xi} = 300$, $N_{zeta} = 11590$, $N_{eta} = 1$). The inflow and outflow assumes supersonic flow and the isothermal wall has a temperature of 300 K. The freestream flow conditions are: $\rho_\infty = 0.088035$ kg/m^3, $T_\infty = 216.65$ K, and $U_\infty = 2950.7$ m/s resulting in a Mach number of 10 and

is consistent with conditions by Melander and Candler [80] who performed analysis in the same manner but instead used the low dissipation, time-independent shock sensor first introduced by Knutson et al. [55]. Based on PSE [80], the most amplified second-mode frequency at the condition is 718.94 kHz. Therefore, estimating the wavelength of a slow acoustic wave at the corresponding frequency based on the flow conditions gives, $\lambda_{718kHz} = 3.69$ mm. This estimates that there are over 32 points-per-wavelength with respect to a slow acoustic wave in the streamwise direction at the region of interest of 1 meter ($\Delta\zeta = 0.111$ mm). This ensures that the grid is more than capable in resolving the instabilities present to demonstrate the significance of numerical dissipation of a high resolution grid and reveal the temporal accuracy of implicit time integration on simulating through breakdown. The fourth-order, low-dissipation flux scheme is used for all cases of this chapter and time integration includes both linear BDF2 and nonlinear BDF2 time advancement schemes using different constant timesteps. The shock sensor takes the following form:

$$\alpha = \frac{-\left(\nabla \cdot \mathbf{u}\right)}{\left[\left|\nabla \times \mathbf{u}\right| + \epsilon \cdot \frac{U_\infty}{\delta}\right]} \tag{3.1}$$

The dissipation is tuned to the dilatation field using a compression based shock sensor of the same form as Equation 2.37. Here, ϵ is a tuning parameter, U_∞ is the freestream velocity, and δ is the maximum boundary layer thickness. A value for ϵ between 0.05 and 0.5 is typically sufficient for simulating most boundary layer problems. Additionally, a lower bound is set for spatial damping comparison. The flow state is forced by periodically introducing a slow acoustic wave at a single frequency of 718.94 KHz based on Equation 2.34. The initial amplitude of the wave is set to 10^{-7}. The relative amplification for the forced DNS solution is defined using an N-factor based on the magnitude of the wall pressure fluctuation, A_f, relative to the

initial freestream amplitude of the wave, $A_{0,f}$:

$$N_f = \ln\left(\left|\frac{A_f}{A_{0,f}}\right|\right)$$

Second-mode Instability: Spatial Damping

To demonstrate how the shock sensor performs in the presence of large perturbations attributed by instabilities in breakdown calculations, the tuning parameters ϵ and lower bound of α are varied. 3.1a) shows the value of α ranging from 0.01 to 1.0 and ϵ is 0.50. This illustrates that the shock sensor works very well in tuning numerical dissipation near the bow shock and away from instabilities present in the boundary layer. As for 3.1b), the shock sensor using $\alpha \in [0.01, 1.0]$ and $\epsilon = 0.01$ tunes a high amount of dissipation to large perturbations induced by second-mode amplification. This is highly undesirable if one were interested in quantifying the amplification of instabilities or turbulent flow quantities for DNS calculations since the added numerical dissipation can attenuate local perturbations. This is not as apparent when applied to this case since the very high resolution of this particular grid significantly reduces the amount of spatial damping. This becomes more important when grid size is constrained by computational resources. In which case, the grid spacing will have less points per wavelength resulting in a fine-scale limit on spatial length scale resolution of the problem.

Figure 3.2 shows the surface pressure perturbations defined as the instantaneous value relative to the baseflow value and normalized by the maximum value. This has the same interpretation as a typical N-factor analysis whereby the absolute value is plotted on a log-scale and the black line denotes N-factor values from PSE of the same condition. The combination of the shock sensor and grid resolution proves that the spatial damping of second-mode amplification remains on the same order of magnitude despite changing the tuning parameters for this case. However, this is

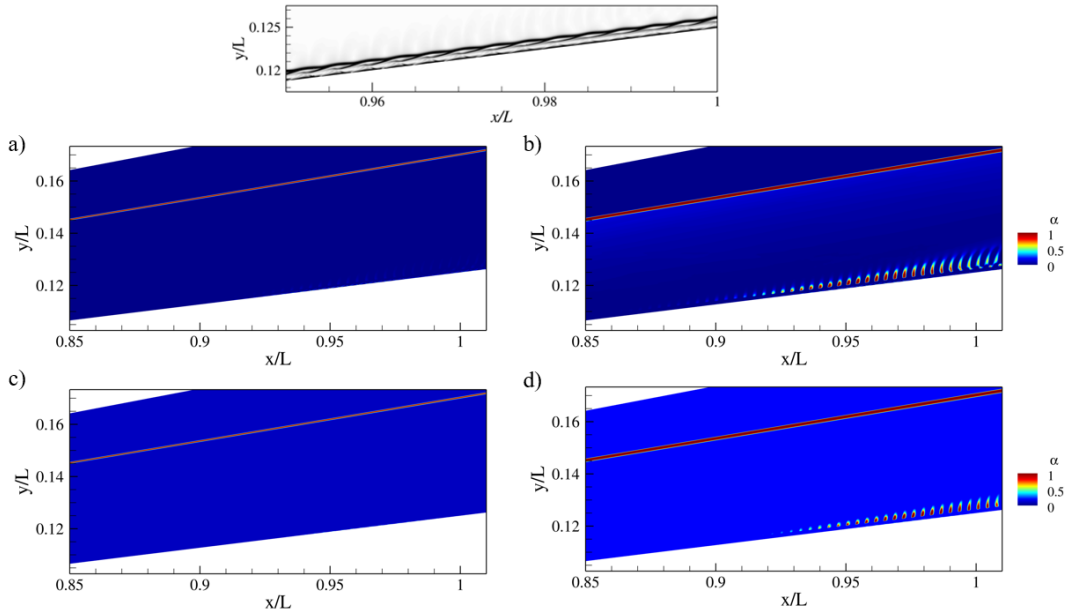

Figure 3.1: Shock sensor values of second-mode breakdown case for 2D straight cone. a) $\alpha \in [0.01, 1.0]$ and $\epsilon = 0.50$, b) $\alpha \in [0.01, 1.0]$ and $\epsilon = 0.01$, c) $\alpha \in [0.1, 1.0]$ and $\epsilon = 0.50$, d) $\alpha \in [0.1, 1.0]$ and $\epsilon = 0.01$. The density gradient magnitude is shown above and is calculated from a) revealing second Mack mode instability.

increasingly more important when using a lower grid resolution at which the spatial damping of the maximum resolvable wave can be significantly attenuated. When it comes to three-dimensional domains, a resolution of 32 points-per-wavelength is not realistic at which even 16 points-per-wavelength in the streamwise and spanwise directions could demand a grid on the order of billions of grid elements. Therefore, if one is interested in amplification of perturbations using DNS this must be explored for the specific case. Lastly, recall that PSE is based on linear theory. For this reason, the amplification of pressure disturbances on the wall departs from linear theory since the flow state is experiencing non-linear flow behavior due to the fluctuations having grown large enough to alter the local flow state in the boundary layer.

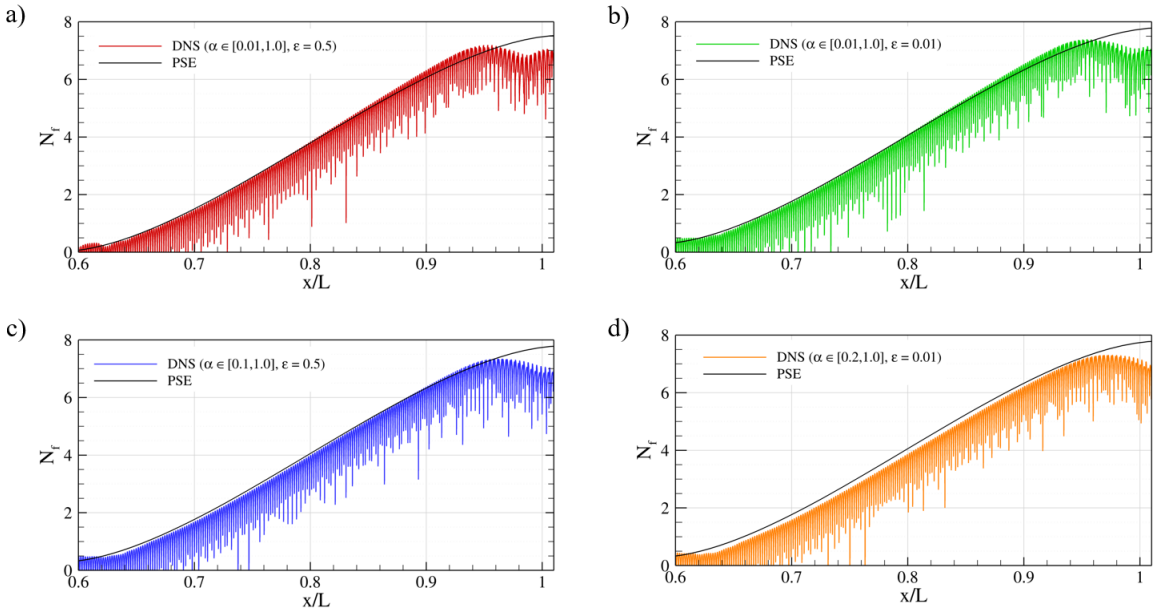

Figure 3.2: Spatial damping of surface pressure perturbations with different shock sensor parameters.

Second-mode Instability: Temporal Damping

To demonstrate the effect of temporal damping using implicit time integration, the amplification of perturbations associated with the second Mack mode instabilities is compared using the shock sensor parameters of 3.1a). Similar to the previous section, the wall pressure disturbance amplitude is calculated and compared to PSE N-factors for reference. This is shown in 3.3 with linear BDF2 and nonlinear BDF2 time integration along with varying timestep. Previous work by Knutson [69], investigated the effects of grid resolution and numerical damping of second-mode amplification as well. For nonlinear BDF2, it was concluded that 140 timesteps per period was sufficient in resolving second-mode amplification using second-order implicit time integration with three Newton iterations for the nonlinear system. In this work, it was found in the case of breakdown that 35 timesteps per period for the maximum desirable frequency ($\Delta t = 40$ ns) is capable in resolving second-mode amplification. How-

ever, convergence of second-mode amplification for nonlinear breakdown is around 70 timesteps per period ($\Delta t = 20$ ns) using BDF2 with three Newton iterations for the nonlinear system from 3.3b). Because of the Newton iterations for the nonlinear solve, the method is 3 times more expensive per timestep than using linear BDF2. Even though it is more computational expensive, the solution accuracy is improved. This is illustrated by comparison of 3.3a) and 3.3c) where the second-mode amplification is significantly attenuated. 3.3c) uses BDF2 without applying Newton iterations (linear solve only) with $\Delta t = 1$ ns. It is observed that the growth rates are similar, but the amplitude of the perturbations are an order of magnitude smaller. In terms of cost, nonlinear BDF2 with 3 Newton iterations took 11,230 core-hours to reach a converged unsteady solution using a timestep of 10 ns. For reference this corresponded to 1.8 days in real time using 1 node on the high performance computing cluster at the University of Minnesota. If explicit RK3 time integration were used it would take 2,410,275 core-hours to reach the same flow time which equates to 27.9 days in real time using the same HPC node. This is a result of the timestep limitation imposed by using an explicit time integration scheme. This is attributed by the near wall spacing of the first cell off the wall for the grid used here.

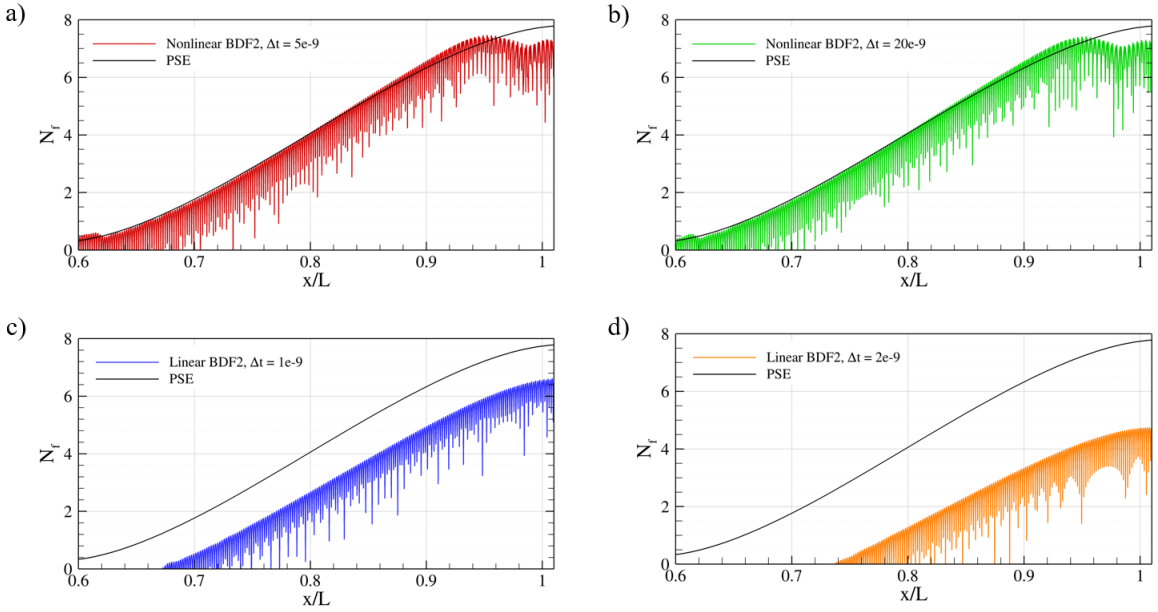

Figure 3.3: Temporal damping of surface pressure perturbations using implicit time integration schemes and varying timestep.

3.4 Modal Analysis

3.4.1 Dynamic Mode Decomposition Methodology

The general idea of dynamic mode decomposition (DMD)[81] is to decompose the flowfield in terms of its dynamics by deconstructing a sequence of snapshot data into a set of spatial modes, each with an associated frequency and growth/decay rate. When these modes are combined, they form a low-order representation for the dynamics underlying the original dataset. Therefore, the method assumes there is an underlying linear dynamical system that governs the evolution between snapshots. The data consists of a sequence of M+1 snapshots spaced a fixed Δt apart, $\{\psi_0, \psi_1, \ldots, \psi_M\}$, where $\psi_i \in \mathbb{R}^N$ is a column vector denoting the i-th snapshot. The N components in each snapshot correspond to the total number of states (i.e., cell centered values) that define the flow state at a given instant in time. Next, two data matrices are formed from the original snapshot sequence:

$$X := [\psi_0, \psi_1, \ldots, \psi_{M-1}] \in \mathbb{R}^{N \times M}$$
$$Y := [\psi_1, \psi_2, \ldots, \psi_M] \in \mathbb{R}^{N \times M}$$

Even though a linear mapping is assumed, DMD is still quite capable in quantifying the dynamics of a flow even if the physical flow processes may be nonlinear in nature[81]. Following the definition in Tu et al. [82], the DMD modes and eigenvalues are determined from a best-fit/minimum norm linear mapping, $\boldsymbol{A} \in \mathbb{R}^{N \times N}$, satisfying the snapshot data relation. In DMD, $\boldsymbol{A}$ is given by the least-squares/minimum-norm solution:

$$\boldsymbol{A}_{DMD} := YX^{+}$$

where X^{+} denotes the Moore-Penrose pseudoinverse of X. The above expression gives the minimum-norm solution provided that $Y = \boldsymbol{A}X$ is exact. For practical cases, such as simulation data, this is not always the case since the data sets are typically underconstrained meaning the total number of states is much larger than the total number of snapshots in time. Note that the eigendecomposition of an $N \times N$ matrix scales with $\mathcal{O}(N^3)$, and so this can be an expensive calculation when N is large. In practice, it is more computationally expedient to work with a low-dimensional proxy system through a projection onto an r-dimensional subspace $\mathbb{R}^r$, where $r < N$. The standard approach for performing this projection involves a singular value decomposition (SVD), which can introduce a heavy memory/storage requirement for large snapshot matrices. A low-storage "streaming" formulation of the DMD algorithm was proposed in [83] to overcome this issue for large datasets. Although the streaming DMD algorithm enables analysis of large datasets, the method can be fragile to noise and round-off error. A noise-robust variant of the streaming DMD algorithm was proposed in [84], which extended the noise-robust total DMD method of Hemati et al. [85] into a low-storage single-pass method. In this work, exclusive use of the streaming total DMD (STDMD) algorithm is made since it is low-storage

and provides a more reliable analysis of stochastically forced DNS datasets of later chapters than the original streaming DMD algorithm. A freely available software implementation of the STDMD algorithm is available [86] and applied in this work.

3.4.2 Compressible Energy Norm Weighting

Before performing STDMD, a linear transformation of the snapshot data is made to be consistent with the Chu energy norm with respect to a mean flow state [87]. Following Dwivedi [88], the energy norm from (4.1) is rewritten in terms of a vector of primitive fluctuation variables, $q = \begin{bmatrix} \rho' & u_i' & T' \end{bmatrix}^T$, as

$$E_{CE} = \int_\Omega q^T \boldsymbol{M} q \, d\Omega, \tag{3.2}$$

where the weight matrix, $\boldsymbol{M}$, is defined as,

$$\boldsymbol{M} = \begin{bmatrix} \frac{\overline{p}}{2\overline{\rho}^2} dV & 0 & 0 & 0 & 0 \\ 0 & \frac{\overline{\rho}}{2} dV & 0 & 0 & 0 \\ 0 & 0 & \frac{\overline{\rho}}{2} dV & 0 & 0 \\ 0 & 0 & 0 & \frac{\overline{\rho}}{2} dV & 0 \\ 0 & 0 & 0 & 0 & \frac{\overline{E}_{int}}{2\overline{T}^2} dV \end{bmatrix}.$$

Because the cell centered data are scalar values, the transformation is simply a weighting of the primitive flow variables including the cell volumes. The transformation is related to the matrix square root of the weight matrix derived from the Chu energy norm inner product. A consideration of the cell volumes is important since each cell carries its own weight of information that is contributing to the total energy of the system. In order to make the modal analysis consistent with the Chu energy norm,

the linear transformation is applied,

$$\tilde{q} = \boldsymbol{M}^{\frac{1}{2}} q,$$

where the vector of disturbance fluctuations now includes the energy norm weighting,

$$\tilde{q} = \begin{bmatrix} \rho' \sqrt{\frac{\bar{p}}{2\bar{\rho}^2} dV} \\ u' \sqrt{\frac{\bar{\rho}}{2} dV} \\ v' \sqrt{\frac{\bar{\rho}}{2} dV} \\ w' \sqrt{\frac{\bar{\rho}}{2} dV} \\ T' \sqrt{\frac{\overline{E}_{int}}{2\bar{T}^2} dV} \end{bmatrix}.$$

Then, the Euclidean norm of $\tilde{q}$ gives the compressible energy of a cell, i.e.,

$$E_{CE} = \tilde{q}^T \tilde{q}.$$

This allows for STDMD to identify boundary layer modes underlying the response associated with local disturbance energy growth.

The dominant mode is the same for all field variables since the simulation is converged to a periodic state, and STDMD is performed on the full flow state including all of the primitive flow variables. Plotting mode shapes for different flow variables reveals the growth or decay of local perturbation quantities as well as the eigen-mode of a flow variable at a discrete frequency. Spatial structures are consistent with simply performing DMD on the raw fluctuation data. However, temporal quantities (i.e., frequencies) computed from the eigenvalues of the raw data without the energy norm weighting are not guaranteed to be consistent with growth of disturbances induced by boundary layer transition mechanisms. The eigenvalues of the modes computed from raw fluctuation data are often damped modes. Whereas, the linear transfor-

mation yields physically meaningful oscillatory modes since the resulting coordinate system for the analysis is consistent with the Chu energy norm. Therefore, STDMD is performed on $\tilde{q}$ to provide an improved approximation of frequencies and mode selection. This makes it so that dominant modes are identified considering five flow variables and their contribution to the kinetic, acoustic, and internal energies relative to a mean flow state.

Streaming algorithm adapted from Hemati et al. [83]:

1. For each new pair of data vectors x_i and y_i, compute the residual $e_Z = z_i - Q_Z(Q_Z^T z_i)$

   (a) First, assemble the data vector

   $$z_i = \left[x_i; y_i\right] = \left[\tilde{q}_i; \tilde{q}_{i+1}\right]$$

   (b) Rather than forming the projection $Q_Z Q_Z^T \in \mathbb{R}^{2n \times 2n}$ explicitly, directly utilize $Q_Z \in \mathbb{R}^{2n \times r_Z}$ and $Q_Z^T z_i \in \mathbb{R}^{r_Z}$.

   (c) Make use of an iterative Gram-Schmidt reorthogonalization procedure to ensure orthogonality of the projection to full working precision [89].

2. If $||e_Z||/||z_i|| > \epsilon$ such that ϵ is a set tolerance, increase the dimension of the corresponding basis, Q_Z, by appending an additional column $e_Z/||e_Z||$ while zero-padding G_Z.

3. Set $\tilde{z}_i = Q_Z^T z_i$ and $G_Z \leftarrow G_Z + \tilde{z}_i \tilde{z}_i^T$ to be used for the Gram-Schmidt procedure of the next snapshot update.

4. Apply POD compression as needed: If the basis, Q_Z, becomes too large (i.e., $r_Z > r_o$ such that r_o is a specified number of modes to retain), compute the leading eigenvectors of G_Z (i.e., V_Z), then set $G_Z \leftarrow V_Z^T G_Z V_Z$ and $Q_Z \leftarrow Q_Z V_Z$. Update until every snapshot of the original data set is read in.

5. Compute the DMD modes and eigenvalues of the de-biased orthonormal basis for the image of X, $\tilde{A} = Q_X^* \begin{bmatrix} 0 & I \end{bmatrix} Q_Z G_Z Q_Z^* \begin{bmatrix} 0 & I \end{bmatrix}^T Q_X G_X^+$, using the definitions as reported in Hemati et al. [84].

To demonstrate modes obtained from a DNS simulation of hypersonic boundary layer transition in the presence of breakdown, STDMD is applied to the forced DNS dataset of the 2D straight cone breakdown case. This is meant to verify the successful parsing of data and implementation for extracting modes since it is expected that a 718 kHz mode will be obtained and representative of second-mode instability. Flowfield snapshots were collected using the sampling parameters of Table 3.1.

Table 3.1: Sampling Parameters

Simulation Timestep	5 ns
Number of Snapshots	1000
Snapshot Spacing	0.2 μs
Sampling Frequency	5 MHz
Snapshot Sequence	200 μs
Single Period Wave	5 kHz

The dataset encompasses the region where the second-mode amplification of the wall pressure signature departs from second-mode amplification predicted by PSE to show that this approach is capable in identifying the dominant mode in the presence of breakdown. For the modal analysis, a rank threshold is required to be set for the number of modes to be retained. Therefore, the frequency spectrum of the total disturbance energy of the entire dataset is computed and shown in Figure 3.6. The large peaks in the frequency spectrum are associated with relevant flow processes, and are therefore used to set the rank threshold. For example, the rank threshold is set to 6 based on the number of peaks for this case since a single oscillatory mode corresponds to two DMD modes.

For the current method, DMD amplitudes are not computed directly and are typ-

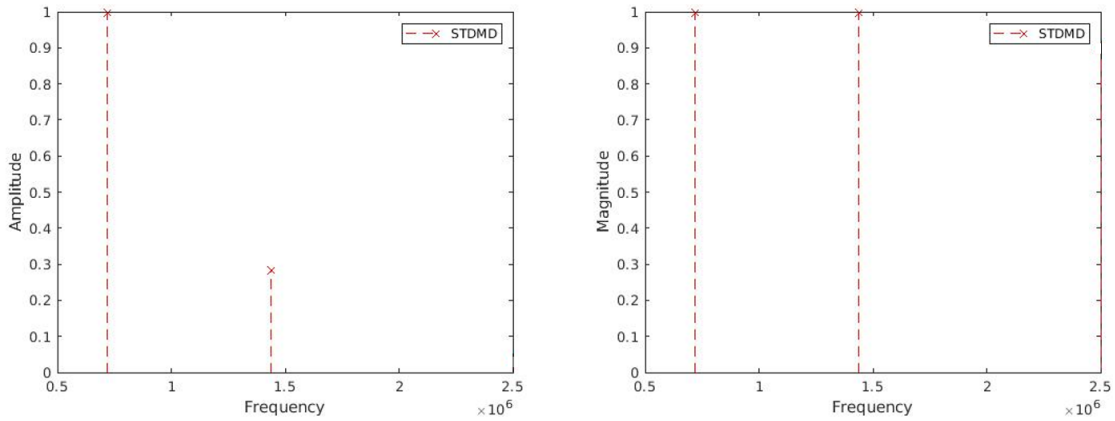

Figure 3.4: Relative DMD amplitudes (left) and magnitudes of the eigenvalues obtained from the eigenvalue decomposition of the linear operator (right).

ically used to identify which modes are most important in describing the lower order representation of the underlying dynamical system. Ideally, the original snapshot matrix would be reconstructed and an associated error computed based on the modes retained with an estimated performance loss. Instead, an approximation of the DMD amplitudes of the corresponding modes were computed by calculating the dot product between the associated right eigenvector of $\tilde{A}$, v_i^+, and the first snapshot of the data sequence, x_o, written as $\alpha_i = v_i^+ \cdot x_o$. The DMD amplitudes are normalized by the mode having the largest amplitude. The modes are then ordered in terms of largest relative amplitudes (i.e., Mode 1, $\alpha_i = 1.0$). The DMD amplitudes and magnitude of the eigenvalues obtained from performing an eigenvalue decomposition on $\tilde{A}$ are shown in Figure 3.4. The leading mode extracted has a frequency of 718.3 kHz and is associated with second-mode amplification as expected. This mode is consistent with the wall pressure signature since the largest signatures near the wall occur around x/L = 0.94. By observation, the mode is oscillatory based on the magnitude of the eigenvalue from Figure 3.4. Furthermore, the second leading STDMD mode has a frequency nearly double that of the leading mode. The mode shape from Figure 3.6 appears to be associated with secondary behavior of second Mack mode instability.

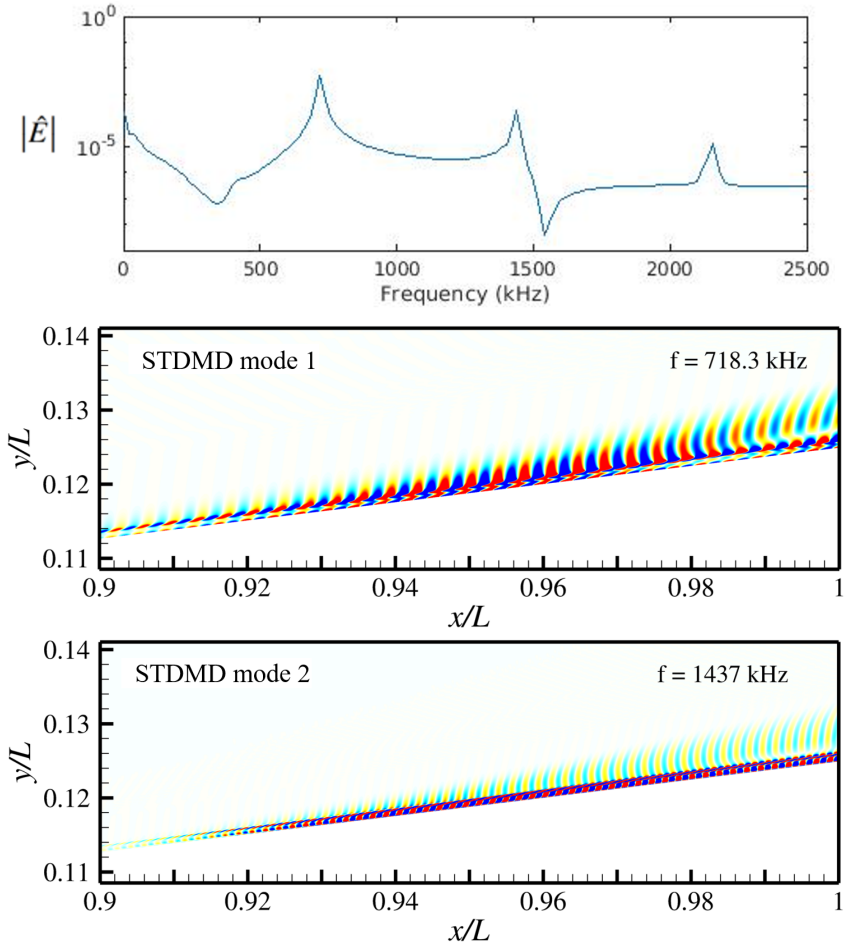

Figure 3.5: Frequency spectrum of the total disturbance energy of the dataset and density perturbation mode shapes associated with the dominant STDMD modes.

This illustrates that acoustic waves are radiating away from the wall which would explain why the DNS solution departs from the PSE prediction which assumes that the boundary layer state does not evolve. A third leading mode is identified using STDMD having a frequency of 2156 kHz but is not shown in this section.

3.4.3 Spectral Proper Orthogonal Decomposition Analysis

Another modal analysis technique utilized later in this work is the spectral proper orthogonal decomposition (SPOD). This method approximates the two-point space-time correlation (covariance) tensor associated with the flow response [90],

$$\mathbf{C}(x, x', t, 't) = \mathbb{E}\left(q(x,t)q(x',t)\right)$$

$q(x,t)$ is the state of interest and $\mathbb{E}$ is the expectation operator and can be thought of as an ensemble average of flow realizations. For stationary states, an efficient implementation is derived in the frequency domain by expanding the Fourier modes as introduced by Towne et al. [91] and Schmidt and Colonius [92],

$$\hat{q}(x,f) = \sum_{j=1}^{\infty} a_j(f)\psi_j(x,f)$$

$$q = \begin{bmatrix} u' \\ v' \\ w' \\ \rho' \\ T' \end{bmatrix}, \qquad W = \int_V \begin{bmatrix} \overline{\rho} & & & & \\ & \overline{\rho} & & & \\ & & \overline{\rho} & & \\ & & & \frac{\overline{T}}{\gamma\overline{\rho}\overline{M}^2} & \\ & & & & \frac{\overline{\rho}}{\gamma(\gamma-1)\overline{T}\overline{M}^2} \end{bmatrix} dV$$

where the expansion coefficients are $a_j(f) = \langle \hat{q}(x,f), \psi_j(x,f) \rangle$ with an appropriate definition of the inner product $\langle \cdot, \cdot \rangle$ in the spatial domain. The choice of inner product defined by the weight matrix, W, is the compressible energy norm following the original derivation [87, 92]. The local cell volume is used to account for the spatially discretized integration while the perturbations quantities are the flow quantities with respect to a mean value. Typically, the baseflow value is commonly used for boundary

layer stability analysis and quantifying disturbance amplification. This is because the amplification of disturbances is typically quantified relative to the laminar flow solution. However, the time-averaged value was chosen to be the mean flow value in this work rather than subtracting off values from two different CFD solutions. However, using the baseflow value can still be used to extract relevant modes. This does not necessarily mean that the extracted eigen-modes are different but the relative modal energies obtained by the weighting energy norm may vary if one used the baseflow value as a fluctuation reference value.

Therefore, stationary snapshots are taken of the unsteady simulations with the perturbations values obtained by subtracting off the time-averaged value. Since the flow is forced stochastically and converged to a periodic state, each snapshot is considered independent and the corresponding SPOD modes are the resolvent modes. Both the mode shape locations relative to regions having the highest disturbance energy and the spectral energy associated with the corresponding modes are used to order each mode based on the contribution to the modal energy relative to the total modal energy. Since we are performing SPOD on five flow variables consistent with the compressible energy norm weighting, the modal energy is associated with the spatio-temporal disturbance energy contribution. Since it is possible for the datasets to be non-periodic in nature due to sampling, a Hamming window is utilized and a specified window length containing 50% overlap is applied to all cases of this thesis. The open-source, freely available software implementation of the SPOD algorithm was used for all results in this work [93].

SPOD algorithm, as reported by Towne et al. [91]:

1. For each data block $n = 1, 2, \ldots, N_b$

   (a) assemble the data matrix

$$\boldsymbol{Q}^{(n)} = \left[\boldsymbol{q}_{1+(n-1)(N_f-N_o)}, \boldsymbol{q}_{2+(n-1)(N_f-N_o)}, \ldots, \boldsymbol{q}_{N_f+(n-1)(N_w-N_o)}\right]$$

(b) using a FFT with a Hamming window, calculate and store the row-wise DFT

$$\hat{\boldsymbol{Q}}^n = \mathrm{FFT}\left(\boldsymbol{Q}^{(\mathrm{n})}\right) = \left[\hat{\boldsymbol{q}}_1^{(\mathrm{n})}, \hat{\boldsymbol{q}}_2^{(\mathrm{n})}, \ldots, \hat{\boldsymbol{q}}_{\mathrm{N}_w}^{(\mathrm{n})}\right]$$

The column $\hat{\boldsymbol{q}}_k^{(n)}$ contains the nth realization of the Fourier mode at the kth discrete frequency f_k.

2. For each frequency $k = 1, 2, \ldots, N_f$:

   (a) assemble the matrix $\hat{\boldsymbol{Q}}_{f_k} = \sqrt{\kappa}\left[\hat{\boldsymbol{q}}_k^{(1)}, \hat{\boldsymbol{q}}_k^{(2)}, \ldots, \hat{\boldsymbol{q}}_k^{(N_b)}\right]$ of Fourier realizations from the kth column of each $\hat{\boldsymbol{Q}}^{(n)}$

   (b) Calculate matrix $M_{f_k} = \hat{\boldsymbol{Q}}_{f_k}^* \boldsymbol{W} \hat{\boldsymbol{Q}}_{f_k}$

   (c) compute the eigenvalue decomposition $M_{f_k} = \boldsymbol{\Theta}_{f_k} \hat{\boldsymbol{\Lambda}}_{f_k} \boldsymbol{\Theta}_{f_k}^*$

   (d) obtain and store the SPOD modes $\boldsymbol{\Phi}_{f_k} = \hat{\boldsymbol{Q}}_{f_k} \hat{\boldsymbol{\Theta}}_{f_k} \tilde{\boldsymbol{\Lambda}}_{f_k}^{-1/2}$ and modal energies $\tilde{\boldsymbol{\Lambda}}_{f_k}$ for the kth discrete frequency.

The interpretation of modes obtained using SPOD is the same as the modes obtained using DMD. For example, if we consider the same forced DNS dataset from the 2D straight cone breakdown case will provide us with very similar dominant mode shapes and frequencies as seen in Figure 3.6. In this case, the dominant modes are identified by summing the eigenvalues of the modes at each frequency and observing the peaks in the power spectral density. Notice, the peaks in the modal energy spectrum are similar to the peaks of the frequency spectrum from the total disturbance energy of the dataset. However, the modal energy spectrum contains more distinct peaks located at 40 kHz, 720 kHz, 1440 kHz, and 2160 kHz. The high frequency modes are associated with secondary instability and subharmonics are consistent in terms of mode shapes and corresponding frequencies obtained with STDMD. As for the 40 kHz mode, the mode shape shows smaller-scale structures are more fine than the highest 2160 kHz mode. This mode was not identified as a dominant mode using

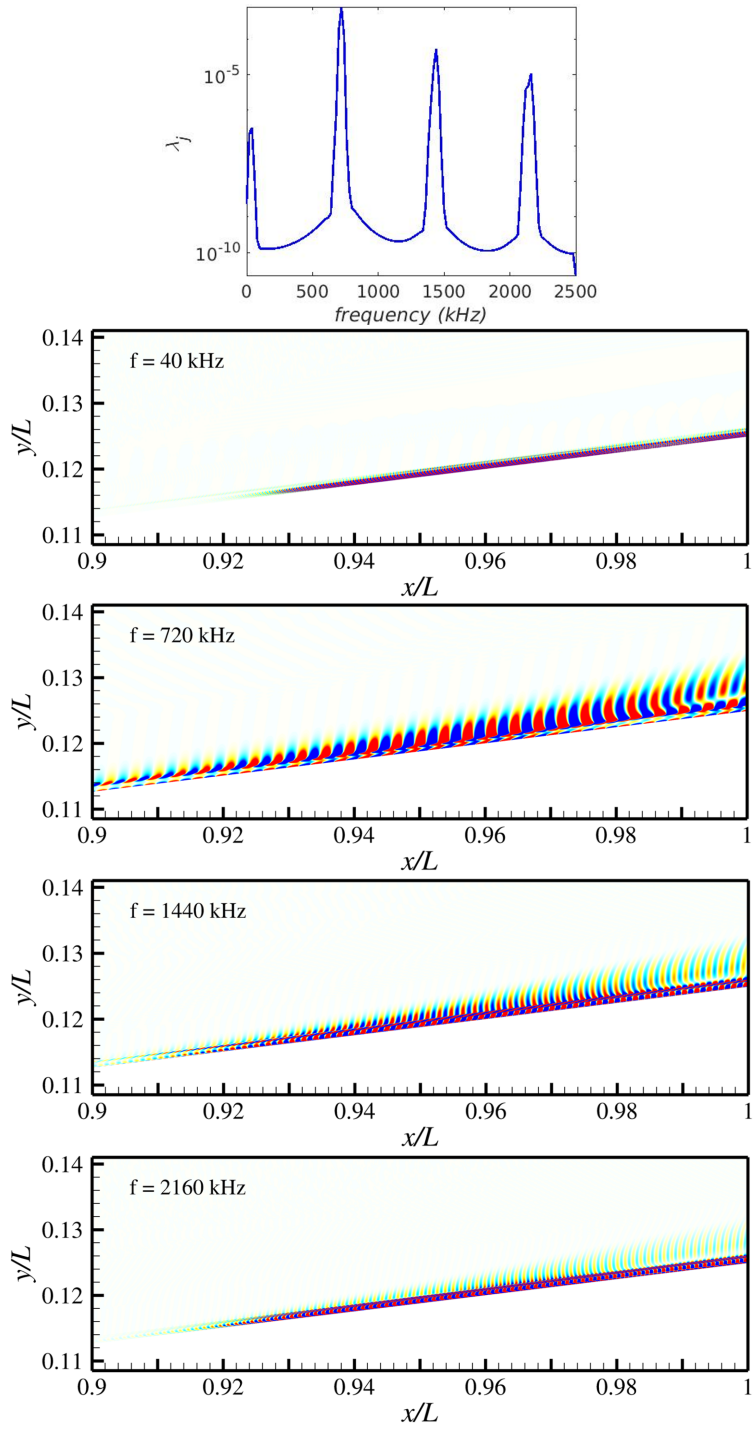

Figure 3.6: Modal energy spectrum and leading SPOD mode shapes.

STDMD. This is potentially attributed by the higher harmonics generated by the developing structures for this particular case since the flow is not allowed to become three-dimensional. Close inspection of the low frequency mode shows evidence of cell-to-cell oscillations. The cell-to-cell oscillations are potentially accumulating more disturbance energy and so may be the reason for the 40 kHz mode shape which arises as a modal energy peak captured by SPOD. Nonetheless, dominant modes extracted using STDMD and SPOD are consistent which allows for the quantification of temporal information associated with dominant instabilities in the presence of breakdown by following the proper numerical methodology.

Chapter 4

Boundary Layer Turbulence (BoLT-2) Simulation and Analysis at Wind Tunnel Conditions

In this chapter, results are presented for simulations performed under quiet wind tunnel conditions to verify the numerical approach for simulating breakdown on BoLT-2. This is achieved by comparing to experimentally observed measurements collected in a low acoustic noise level environment. The experimental measurements were made in the Mach 6 Quiet Wind Tunnel (M6QT) and provided by Texas A&M University. The measurements for comparison include surface heating, surface pressure spectra, and flowfield fluctuations.

4.1 Steady Flowfield

The baseflow was first computed using the freestream values of Table 4.1 to gain an understanding of the flow structures that exist in the flowfield. Similar three-dimensional flow features were first simulated on BoLT and described in previous papers by Thome et al. [10, 94]. The leading edge of the geometry is a two-dimensional cylindrical edge that revolves to four swept edges. The hypersonic flow around the surface curvature produces strong bow shock curvature where a shock-shock inter-

action generates vorticity post-shock. Thome et al. [94] computed vorticity budgets quantifying the vorticity distribution in the near wall region. This produces varying pressure gradients close to the wall and developing vortex structures that are able to support various types of boundary layer instabilities.

Table 4.1: Freestream Conditions

M_∞	U_∞ (m/s)	ρ_∞ (kg/m^3)	T_∞ (K)	T_{wall} (K)	Re/m (m^{-1})
5.9	871.09	0.0424	52.68	300	10.8x10^6

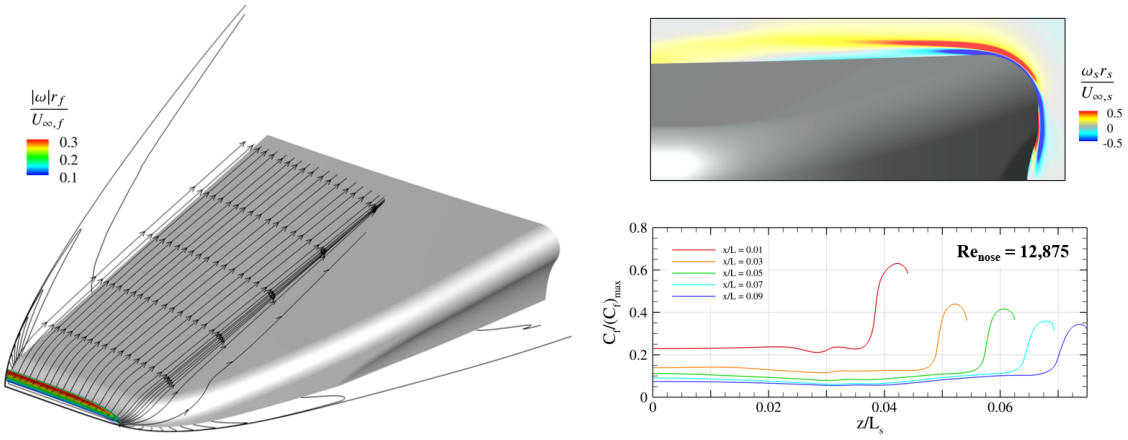

Figure 4.1: Left shows streamlines originating from regions having high vorticity magnitude. The normalized streamwise vorticity is show on the top, right. The bottom, right shows surface line extractions of the skin friction coefficient normalized by the maximum value on the wall.

The most apparent structures are located further downstream taking the form of large-scale counter rotating vortex structures located on both sides of the centerline of the top surface. Between the centerline and swept edge, there is a high amount of localized vorticity where downstream developing vortex structures become apparent. This has a direct affect on the surface heating distribution where the varying thickness of the boundary layer produces streaks in the surface heat flux distribution. A three-dimensional view in Figure 4.2 depicts this where planar slices show colored

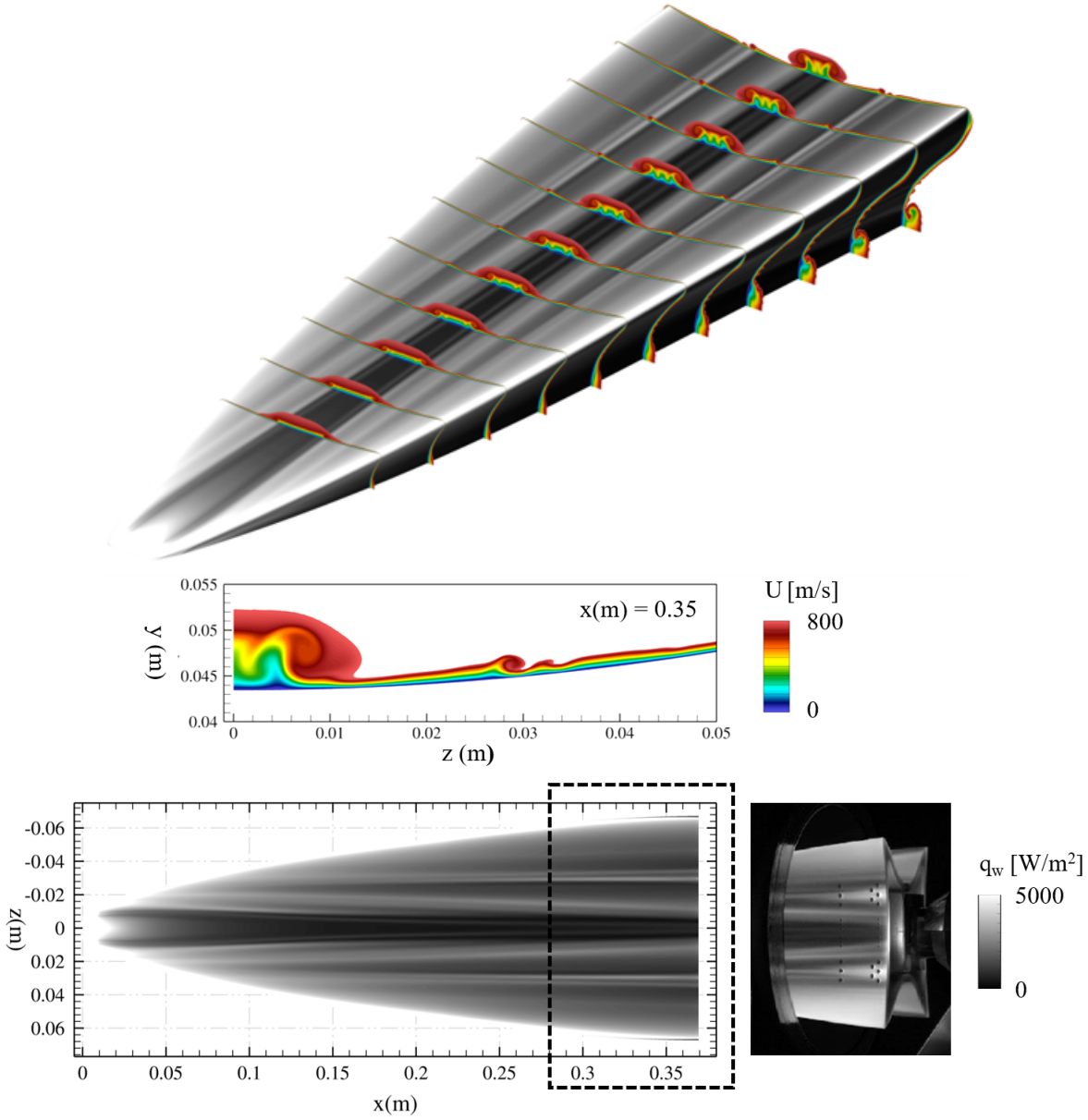

Figure 4.2: Planar slices from x/L = 0.25 to 1.0 (L = 0.36925 m) show streamwise velocity contours cut off at 800 m/s. The wall is grey-scale shaded from 0 to 5000 W/m^2 to show surface heat flux variations. Comparison is with the smooth 25% subscale 1.5 m model IR image from [15].

contours of streamwise velocity and the surface heat flux is plotted on a grey-scale. Notice the heat flux gradients become more distinct with the development of vortices

resulting from a strong crossflow component. A qualitative comparison of the baseflow solution assumes laminar flow and therefore does not capture the same localized heating as seen in experiments. Thermal imaging from experiments reveal increased heating downstream originating near developing crossflow vortex structures. Even though some discrepancies are likely contributed by a finite amount of roughness and possible sideslip, the initial stages of breakdown appear in this region motivating the current work and suggests that the boundary layer is transitional. Furthermore, Figure 4.2 shows a qualitative comparison of the surface heat flux with experiment. The experimental model shown is a surface finished 25% subscale 1.5 m geometry used in simulation[1]. Qualitative comparison shows similar heating effects except for highly localized regions near the developing vortical structures when compared to the laminar solution from simulation. Therefore, in this chapter a forcing function is used to introduce disturbances into the flowfield to mimic the effects of wind tunnel noise to obtain a response representative of natural transition.

4.1.1 Grid Resolution Estimate

The grid used in this work is a much higher resolution than what was previously used to investigate BoLT in the past [11] which was shown to resolve the steady-state flow structures at a slightly lower Reynolds number. Furthermore, it was shown that the steady state flow structures are converged with using a grid that contained less cells using the high-order, low-dissipation numerics. However, the total cell count is a relative value since it is the local resolution that is important. Additionally, a grid used for DNS should be constructed to be based on the desired spatio-temporal resolution of the grid and numerical method used. Therefore, the grid in this work

[1]The actual axial length, from the leading edge to the end of the research geometry, of the CAD file of the so called 1.5 m geometry is 1.477 m. Therefore, 0.36925 m is used for all non-dimensional lengths of the 25% subscale 1.5 m geometry in this work

was constructed to have a resolution at the end of the domain capable of resolving potentially high frequency content for the unsteady solutions. As a consequence of grid topology construction, a much finer resolution is obtained upstream. Details of the grid generation process and resolution estimate can be found in [95]. The grid metrics are summarized in Table 4.2. The next chapter introduces convergence related to the grid resolution and modal analysis sampling following the results of this chapter.

Table 4.2: Subscale BoLT-2 grid resolution

Fine Grid	
Total cell count	534 million
Streamwise cells	2880
Wall-normal cells	425
$\Delta\xi_(x/L = 1.0)$, mm	0.14
$\Delta\zeta(x/L = 1.0)$, mm	0.23
y^+_{max}	0.06

4.1.2 Boundary Conditions

To save on computational cost as well as focus on the later stages of transition, the simulations were carried out on a subdomain so that forcing is introduced at the inflow of the subdomain. Therefore, this requires a zonal DNS approach thereby neglecting the receptivity process to allow for high-fidelity study of modal growth mechanisms. This is achieved with the help of a converged baseflow solution from a separate upstream solution. Next, cell centered data is extracted at the outflow boundary of the upstream solution containing all primitive variables. This computational plane begins at the wall, spans the two symmetry planes, and extends to the freestream boundary surface. The computational plane is imposed as a Dirichlet boundary condition at the inflow ghost cells of the downstream subdomain. The location of the inflow plane is at x/L = 0.23 based on the geometry length, defined from the nose tip to the end

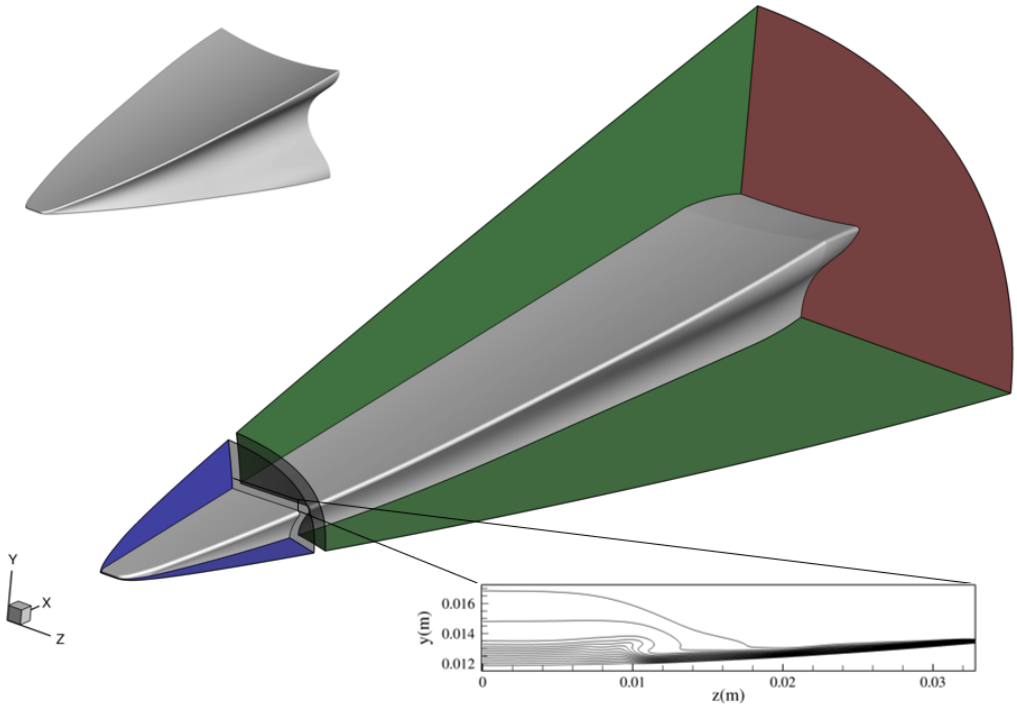

Figure 4.3: Individual subdomains used for interpolated inflow with computational plane imposed as boundary condition onto the domain of interest.

of the geometry. The inflow plane location was chosen such that predicted N-factors from PSE for the second mode and crossflow instabilities remains low upstream of x/L = 0.30. The boundary conditions are shown in Figure 4.3 and assumes a uniform supersonic inflow (hidden), isothermal wall with no-slip (grey), supersonic outflow (red), and symmetry planes (green) in the xy- and xz-planes to take advantage of the bilateral symmetry. The domain contains an extended expansion corner for improved representation of the flow conditions at the end of the experimental model. The isothermal wall is imposed since wind tunnel runs are relatively short duration and the magnitude of the surfacing heating is low. Therefore, the wall temperatures are expected to remain nearly constant. Even though there is a possibility of a finite amount of angle of attack and side-slip, the flow is assumed to be at zero degrees angle of attack and side-slip for simplicity. The grid of the downstream subdomain

contains approximately 390M total elements due to truncation.

4.2 Unsteady Boundary Layer Instability Analysis

Before introducing controlled disturbances, a steady-state solution is fully converged before applying forcing to the baseflow state. The forcing approach is similar to the random forcing approach by Hader and Fasel [18] which is meant to simulate natural transition. Therefore, the approach used in this work is meant to mimic the effects of freestream wind tunnel noise by introducing disturbances at the interpolated inflow boundary only. By doing this, the receptivity process is neglected to focus on investigating the disturbance growth response due to boundary layer instabilities. The idea is to force with a wide range of frequencies to investigate the transition process so that there is not a bias towards a distinct instability mechanism. This is achieved by specifying a noise amplitude, A_{noise}, and using a pseudo-random number, $r\epsilon[0,1]$, which is generated for each cell element when looping over the inflow cells of the computational plane. Furthermore, a new random number is generated at every time step as well to apply a broadband range of frequencies. The random perturbations are directly applied to the pressure field at the forcing plane, the same computational plane as the imposed inflow boundary condition for ease of implementation. The density and temperature adjust to the pressure perturbations based on the linearized isentropic relations thereby assuming initial entropy fluctuations are negligible to satisfy the acoustic-mode.

In the past, environmental freestream characterization for wind tunnels have measured mass flux fluctuations (ρu)'. There is uncertainty with the characterization of mass flux fluctuations for this forcing function that are representative of a quiet wind tunnel environment. Using the RMS voltage measurement from a hotfilm, Huntley [96] estimated a freestream mass flux fluctuation of 2% of the freestream mass flux

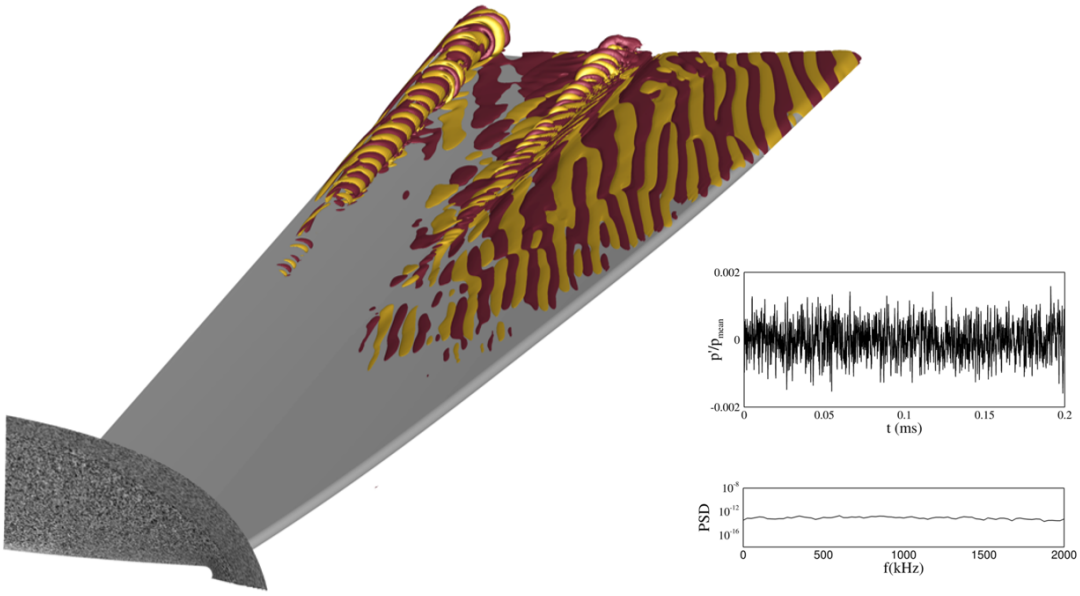

Figure 4.4: Isosurfaces of the streamwise velocity perturbations, u' = $\pm$1x10^{-3} (left) and pressure disturbance time signal & frequency content of a freestream point lying on the forcing plane (right).

fluctuation level for a conventional wind tunnel. It is well known for quiet wind tunnel environments that the freestream mass flux fluctuations are much lower. Therefore, a perturbation in velocity is applied to include a disturbance kinetic energy such that the maximum RMS mass flux fluctuations are reported to be less than 0.003% of the freestream mass flux. This makes it so that the fluctuations introduced are a discrete approximation of the spectrum with the pressure and velocity disturbances having close to the same noise levels. By setting the initial amplitude of the velocity disturbances equal to the noise amplitude, the mass flux fluctuations are the same order of magnitude as the estimate based on the density perturbations and convection velocity relation following Smits and Dussauge [97]:

$$\frac{(\rho u)'}{\overline{\rho}\,\overline{u}} = \frac{\rho'}{\overline{\rho}}\left(1 + \frac{1}{(\gamma-1)M^2}\right)$$

The pressure disturbances are introduced with as $p' = A_{noise}(2r-1)$. Fluctuations

in the remaining primitive flow variables are determined as:

$$\begin{pmatrix} \rho' \\ u_i' \\ T' \end{pmatrix} = \begin{pmatrix} \frac{1}{\overline{a}^2} \\ 1 \\ \frac{(\gamma-1)\overline{T}}{\overline{\rho}\,\overline{a}^2} \end{pmatrix} p'.$$

Because of the stochastic nature of the forcing function, there is a spectrum of amplitudes and so a forcing level is defined. Therefore, the forcing levels for the cases were defined using P_{RMS} =RMS($\frac{p'}{\overline{p}}$) where p' is the fluctuating value of pressure and $\overline{p}$ is the time-averaged value of pressure sampled. The fluctuating pressure levels of the input forcing were characterized by sampling various locations in the freestream lying on the forcing plane.

To gain qualitative insight into the primary vortex structures that could support flowfield disturbances, Q-criterion is calculated and defines a vortex as a connected fluid region with a positive second invariant in the divergence of velocity and requires the pressure to be lower than the ambient pressure in the vortex [98, 99]. An overview of various vortex identification methods can be found in the paper by Kolár [100]. As reported, the definition of Q-criterion states, $Q = \frac{1}{2}(\|\boldsymbol{\Omega}\|^2 - \|\boldsymbol{S}\|^2) > 0$, where $\boldsymbol{\Omega}$ and $\boldsymbol{S}$ are the anti-symmetric and symmetric components of the velocity gradient tensor. Figure 4.5 shows an isosurface for a single value of Q and colored by instantaneous local temperature revealing coherent structures. This reveals a range of length scales and the large-scale vortex is apparent near the centerline. Moving outboard, there are wave-like structures propagating in the flow direction and appear trapped between the wall and boundary layer edge located on both sides of the developing crossflow vortical structures. The structures originate upstream in the viscinity where second-mode was identified on BoLT in the past. Furthermore, the development of small-scale streamwise vortices produce a steady isosurface. Towards the end of the geometry, there is a formation of localized small-scale coherent structures leading to breakdown

of the lower forcing level case and located within the developing crossflow vortical structures. This is depicted by turbulent onset with the development of hairpin-shaped structures.

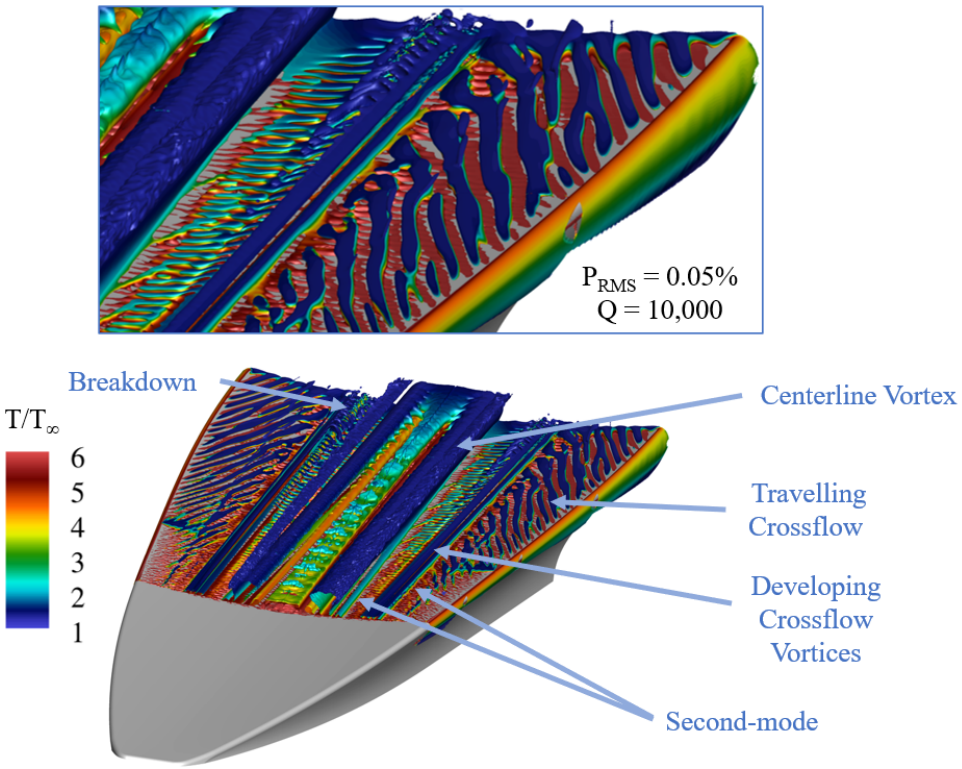

Figure 4.5: Identification of vortex structures based on Q-criterion with a single isosurface colored by local temperature.

Decomposing this flowfield in a manner consistent with the computational methodology is unclear due to the complexity of the flowfield and geometry. Therefore to help circumvent disturbance amplification, the time-averaged disturbance energy amplitude is computed. Because the data is collected from DNS, the simulation dataset includes the effects of linear and nonlinear flow processes. To quantify nonlinear disturbance growth, the compressible energy distribution was computed with a norm of the perturbation chosen to account for disturbance energy in a compressible flow. For the present work, the transfer of disturbance energy from a steady main stream was

selected based on the positive definite energy norm commonly used in performing stability analysis [101, 102] and first introduced by Chu [87]. This is an intrinsic energy norm for the study of boundary layer analysis since it is consistent with characterizing disturbance fluctuations by considering kinetic, acoustic, and internal energy contributions,

$$E_{CE} = \int_V \left(\frac{1}{2}\overline{\rho} u_i' u_i' + \frac{\overline{p}}{2}\left(\frac{\rho'}{\overline{\rho}}\right)^2 + \frac{\overline{E}_{int}}{2}\left(\frac{T'}{\overline{T}}\right)^2 \right) dV.$$

The overbar signifies the quantities associated with the baseflow, and the prime values are the disturbance quantities calculated by subtracting the baseflow value from the instantaneous value. The term inside the integral has units of energy per unit volume and the integral is over a single grid element. Because we have cell centered data using a finite volume method, the energy is computed within a cell by simply multiplying by the cell volume in the discrete form since the cell centered values obtained from using a finite volume method are the average value across a cell making it a second-order accurate approximation. The instantaneous total energy across a cell is computed at each instance in time and then the value is averaged in time. Figure 4.6 shows the compressible disturbance energy distribution for slices taken at separate streamwise locations. Notice that the maximum value grows over three orders of magnitude from x/L = 0.740 to x/L = 0.979, where L = 0.36925 m (from 25% scale of full-scale having 1.477 m length), near the stationary vortex structure revealing localized nonlinear disturbance energy growth. Instantaneous surface pressure perturbations show an imprint of boundary layer instabilities relative to the increase in disturbance energy off the wall. The same datasets used for modal analysis are used for this calculation.

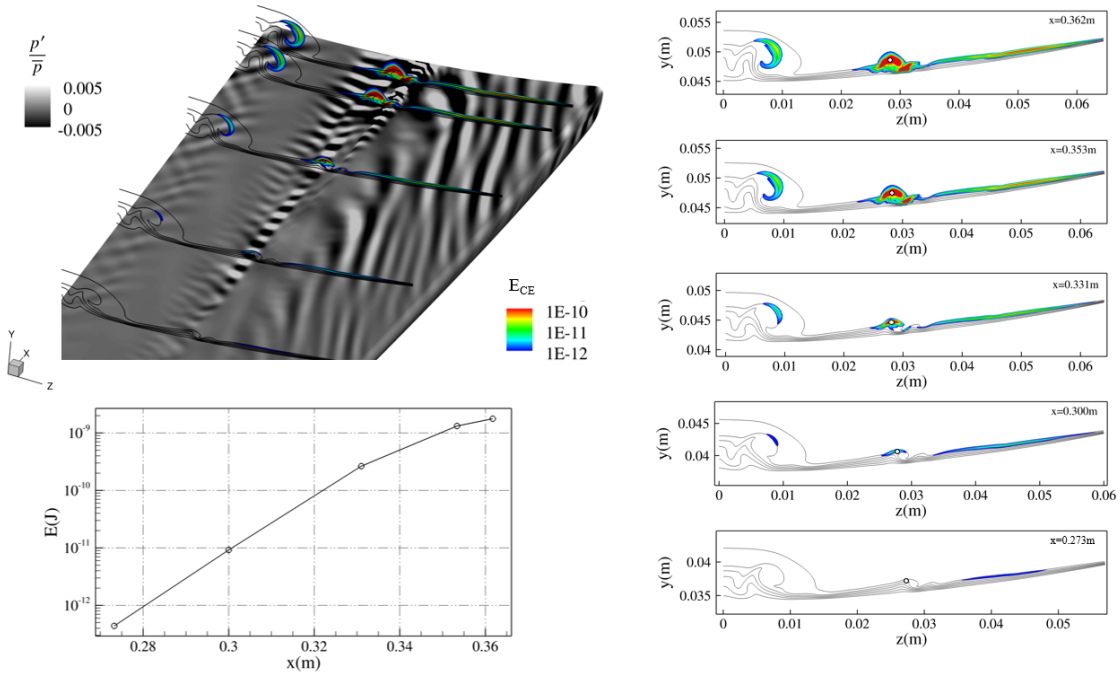

Figure 4.6: Disturbance compressible energy distribution for $P_{RMS} = 0.05\%$ forcing level. Top left shows slices taken at x/L = 0.740, 0.812, 0.896, 0.957, and 0.979 with contour lines corresponding to streamwise velocity and colored contours of the energy plotted on a log-scale. Bottom left are probed local maximum values near the primary stationary vortex structure with respect to the slices as shown on the right.

Table 4.3: Sampling Parameters

Simulation Timestep	20 ns
Number of Snapshots	668
Snapshot Spacing	0.3 μs
Sampling Frequency	3.3 MHz
Snapshot Sequence	200 μs
Single Period Wave	5 kHz

For the current work, it is not trivial to collect time-series data provided the geometry, grid size, and curvilinear mesh containing grid singularities. In order to simplify parsing data, snapshot data was collected by collecting cell centered data from cells that intersect a plane at a specified x-coordinate. Furthermore, to extract pertinent

flow processes using Dynamic Mode Decomposition (DMD) or Proper Orthogonal Decomposition (POD) based techniques, the sampling rate has to be sufficiently high frequency to resolve and capture relevant spatio-temporal information. Schmid [81] expresses that a sampling frequency of about three times the Nyquist cutoff ensures satisfactory results from DMD based on past experience. Since the current grid is estimated to resolve up to 500 kHz, the sampling frequency is 3.3 MHz or over three times the Nyquist cutoff of a 500 kHz wave. At each streamwise location, the snapshot sequence spans 200 μs corresponding to one period of a 5 kHz wave. This provides 668 snapshots in time with a snapshot spacing of 0.3 μs. The sampling parameters are summarized in Table 4.3.

4.3 Spatio-temporal Analysis

The data sets in this section span regions including nonlinear flow effects to demonstrate how well the modal analysis approaches used in this work are capable of identifying dominant modes. Additionally, some of the datasets selected for analysis in this work include strongly nonlinear flow behavior denoted as turbulent onset as identified by the small-scale coherent structures of Figure 4.13. As a consequence, regions which contain a broad frequency spectrum can make it very challenging in identifying dominant instabilities since modes may be associated with more than one instability represented at a single discrete frequency. Previously, Shrestha and Candler [103] performed a two-dimensional calculation on trip induced transition of boundary layer roughness elements using SPDMD [34] and the Chu energy norm for mode selection. DMD modes qualitatively represented transition mechanisms, but the linear mapping between consecutive snapshots was deemed inaccurate since the dataset included regions where the flow was fully turbulent or experienced nonlinear behavior. This was observed in the present work when including turbulent regions, but consistent modes

were still extracted when including regions experiencing nonlinear flow behavior as a part of the modal analysis dataset. The work by Knutson et al. [11] performed SPDMD on truncated snapshot data showing the dominant modes at a particular location. This is useful for isolating modes contributing to linear growth of boundary layer instabilities, but does not allow a direct comparison of DMD modes in the spanwise direction and at the same streamwise location. Therefore, snapshots encompassing the entire spanwise region from the centerline to the swept leading edge is meant to show that STDMD with the energy norm weighting is able to identify modes contributing to transition in the initial stages of breakdown without making the prior assumption as to where flow transition originates. This allows for a direct comparison to determine which mode has a more significant contribution to the flow dynamics in the presence of breakdown by ordering the modes in terms of DMD amplitudes. The following results show modes contributing to transition, and the dominant modes are identified to be associated with instabilities initiating breakdown at wind tunnel conditions.

4.3.1 STDMD Results: Modal Growth Mechanisms

STDMD Rank Threshold

To determine the proper rank threshold, the integrated disturbance energy norm, E, is computed as a function of time through a summation of all elements which make up a snapshot. The power spectral density (PSD) of the signal is computed where it was found that peaks values that do not drop below two orders of magnitude, relative to the highest peak value, identified modes having large DMD amplitudes with frequencies consistent with surface pressure PSD peaks. Therefore, the PSD of the energy norm is primarily used to dictate the number of modes to retain as determined by the rank threshold. The discrete Fourier transform is computed from the energy

norm signal where the peaks in the frequency spectrum corresponds to significant flow processes. This provides frequency ranges of the flow processes spanning the region in time where the highest peaks have frequencies consistent with the relevant modes identified by STDMD. However, the highest peak value, $|\hat{E}|$, does not necessarily correspond to a more physically significant STDMD mode as seen in Figure 4.7. The frequency spectrum only provides an estimate for expected mode frequencies by making a direct comparison to the extracted modes at various truncation levels. The proper truncation level was selected such that the same dominant modes are identified between various truncation levels where the frequencies resemble the frequency spectrum peaks of the energy norm. By computing the PSD and frequency spectrum of the energy norm, we are able to identify an estimate for the number of modes to retain while providing an estimate of expected mode frequencies. The relative DMD amplitudes are used to order the modes and the ordering is consistent with surface pressure PSD measurements from experiment and simulation.

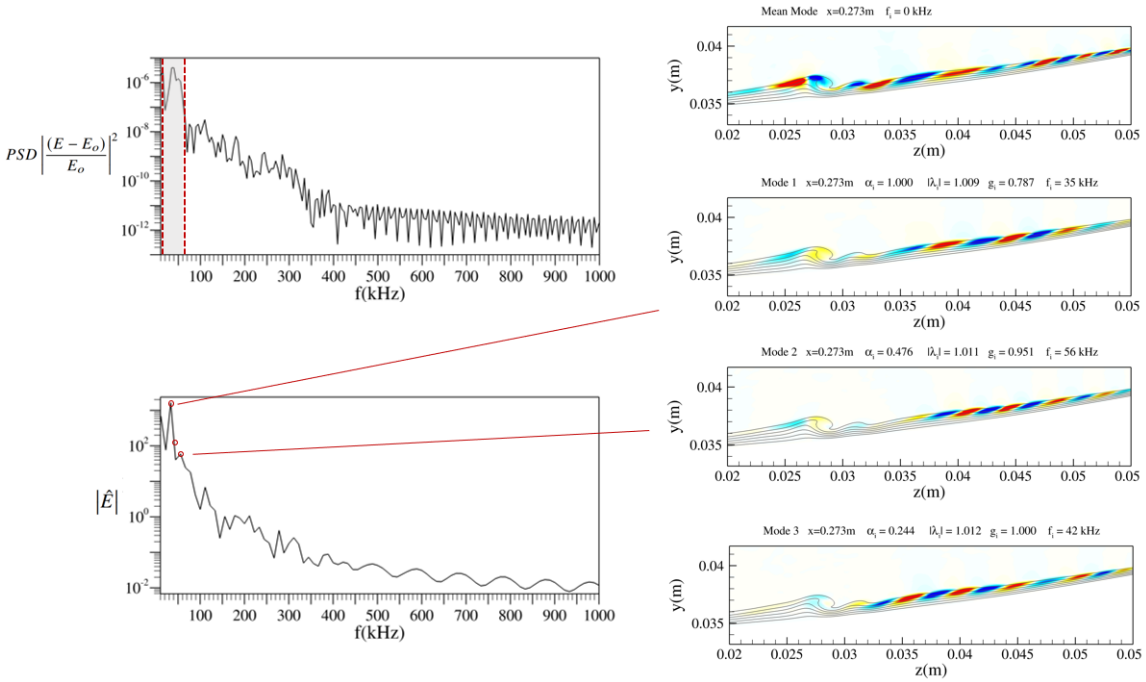

Figure 4.7: Mode identification used for selecting truncation level.
"o" denotes time averaging of, E, the energy norm integrated over all elements that construct a slice.

One should be aware that an under-truncation (i.e., high rank threshold) of the STDMD spectrum can lead to spurious modes which arise as numerical artifacts. This is thought to be a caused by over fitting the linear operator due to propagating broadband frequency content associated with the stochastic forcing function. To the contrary, an over-truncation (i.e., low rank threshold) of the spectrum will lead to modes not being retained that could have a significant contribution to the increase in local disturbance energy. It is important to retain all physically relevant modes since they have greater contribution to the increase in compressible energy and the flow dynamics.

Leading Boundary Layer Modes

Using the energy norm weighting and mode identification, dominant boundary layer modes are extracted at five streamwise locations using a forcing level of $P_{RMS} = 0.05\%$. For brevity, the first three dominants mode shapes of streamwise velocity perturbations are shown for the remaining four slice locations downstream. Since we have competing instabilities dependent on local boundary layer properties, there are modes which have varying spatial signatures meaning that particular modes may be contributing more to the local disturbance amplification than other modes at different locations. Therefore, the modes may exist but are not deemed to have a physically significant contribution to the flow dynamics as identified by STDMD at a particular location. All the dominant modes are shown away from the large-scale centerline vortex. This is due to the fact that the disturbance values are largest in the regions identified in Figure 4.6 even though the data of the centerline vortex is included in the modal analysis. Figure 4.8 shows that the leading DMD modes at x/L = 0.812 are primarily located outboard. The spatial structures are located on the left side of each figure and correspond to the real component of the eigenvectors computed from the linear operator. The magnitude of the real and imaginary components of the eigenvectors are plotted on the right side of each figure. The discrete values above each plot are computed from the eigenvalues where $|\lambda_i|$ is the magnitude of the corresponding eigenvalue. The frequencies are computed as $f_i = \angle\lambda_i/(2\pi\delta t)$ and the growth rates as $g_i = \log|\lambda_i|/\delta t$.

The STDMD mode shapes at x/L = 0.812 resemble the mode shapes extracted using SPDMD on BoLT by Knutson et al. [11], despite the dominant mode here has a frequency of 35 kHz. Additionally, the mode is consistent with traveling crossflow instability in terms of mode shape and frequencies compared to BoLT SPDMD results. In fact, all leading modes appear to be associated with traveling crossflow at this streamwise location. Interestingly, the third dominant mode has a higher frequency of

69 kHz and is primarily located near the developing crossflow vortices according to the magnitude of the eigenvectors plotted on the right. Furthermore, the frequencies of these modes are consistent with the local frequencies computed for traveling crossflow using PSE by Mullen and Reed [104]. The magnitude of the eigenvalues, $|\lambda_i|$, are all positive suggesting that all the modes at x/L = 0.812 have positive growth rates.

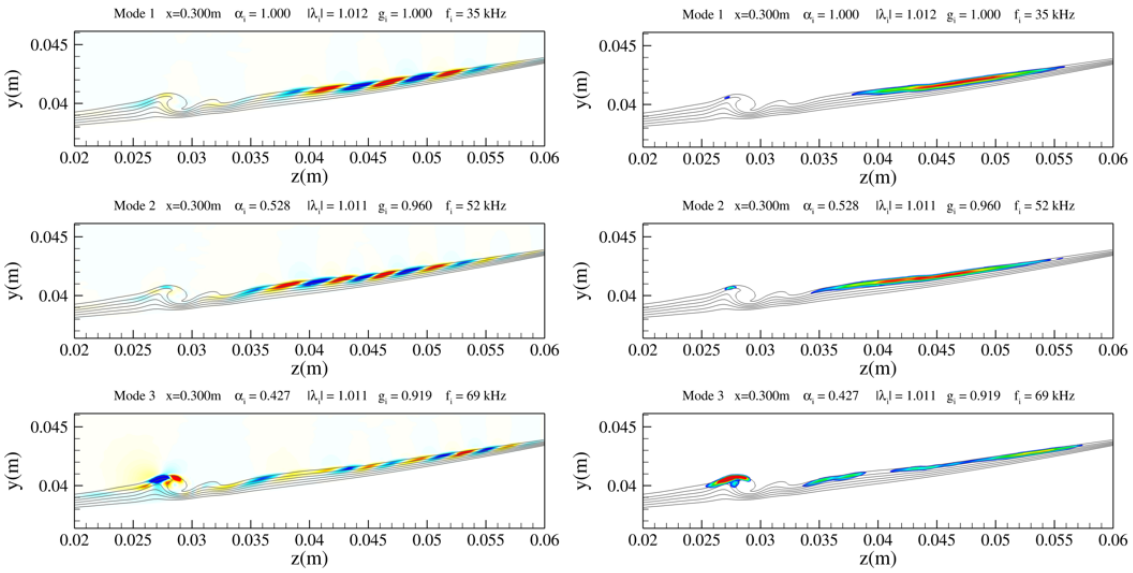

Figure 4.8: Leading STDMD modes of streamwise velocity extracted at x/L = 0.812. Real component of the eigenvectors with positive values denoted as red and negative values as blue (left). Magnitude of the eigenvectors (right) with the larger value represented with red (right).

The crossflow modes having frequencies in the range of 35 kHz and 52 kHz are also identified as leading modes downstream at x/L = 0.896. The mode shapes of the magnitudes reveal that the modes are primarily active closer to the swept edge. Notice that the magnitudes show these modes are not only active outboard but show small signatures near the developing crossflow vortices as well. This is due to the fact that a single DMD mode can represent multiple transition processes happening at close to the same discrete frequency. Therefore, this reveals that DMD modes associated with crossflow instabilities are beginning to have a more significant contribution on

the inboard side of the developing vortex structure. However, the mode with the largest contribution to the increase in disturbance fluctuation has a frequency of 176 kHz and is highly localized on the top portion of the developing crossflow vortex structure where velocity gradients are highest. It is at this location where disturbance are experiencing exponential energy growth as seen previously from Figure 4.6.

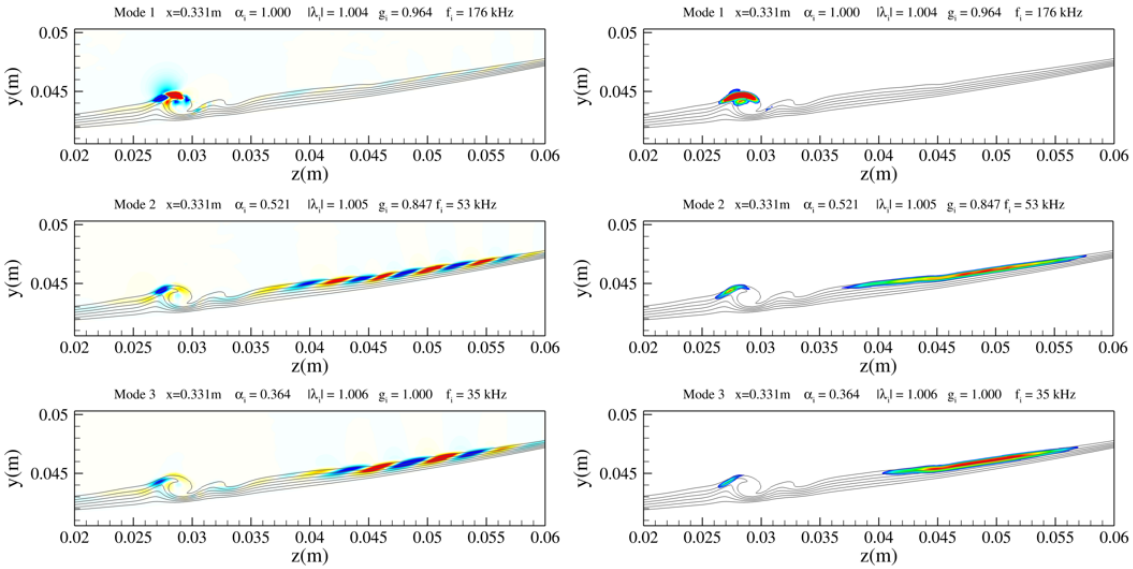

Figure 4.9: Leading STDMD modes of streamwise velocity extracted at x/L = 0.896.

Similar to upstream, a high frequency mode is identified to be the dominant mode at x/L = 0.957 and x/L = 0.979 with a frequency 185 kHz and 190 kHz, respectively. The spatial structures are slightly different than the dominant mode upstream but are all highly localized near the crest of the developing vortical structure. This suggests the high frequency mode is the dominant mode initiating breakdown. A range of discrete frequencies of this mode are most likely contributed by the fact that the analysis is performed on each streamwise location independently as well as the local flow properties vary in space. Depending on the forcing level, spatial location, and rank threshold, this mode was found to vary in frequency between 175 to 210 kHz and has been identified as the dominant mode beginning at approximately 90% of the

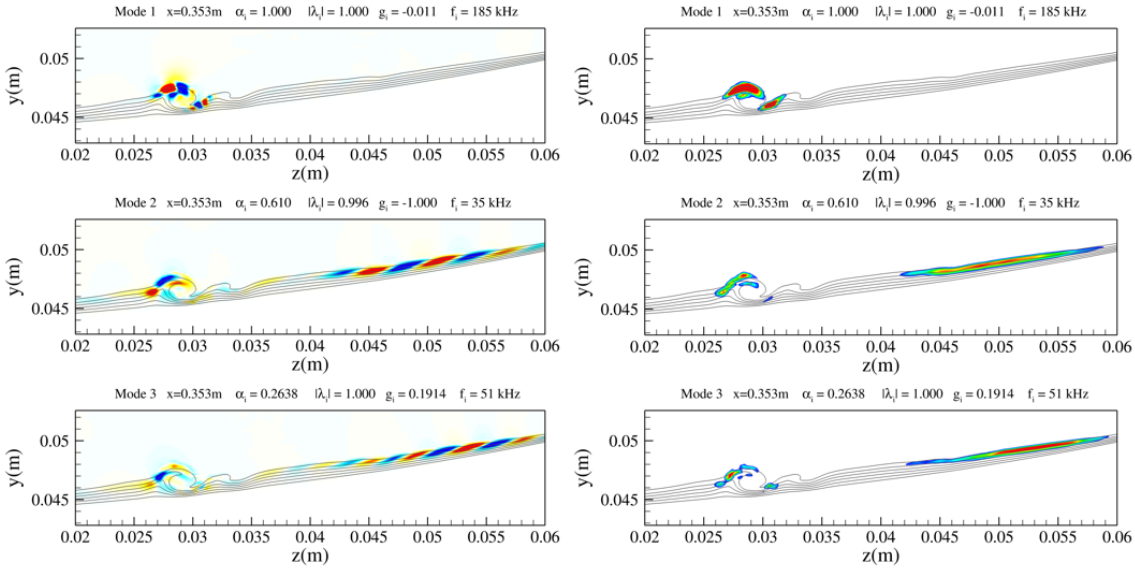

Figure 4.10: Leading STDMD modes of streamwise velocity extracted at x/L = 0.957.

geometry length. It is worth noting that modes primarily associated with crossflow instabilities are still identified as leading modes and have frequencies ranging from 30 to 60 kHz. Only the first couple modes associated with traveling crossflow are shown since they are the leading modes identified by the STDMD analysis. The modes are primarily located outboard near the swept edge. Additionally, signatures are present near the dominant mode due to the flow experiencing highly localized turbulent onset.

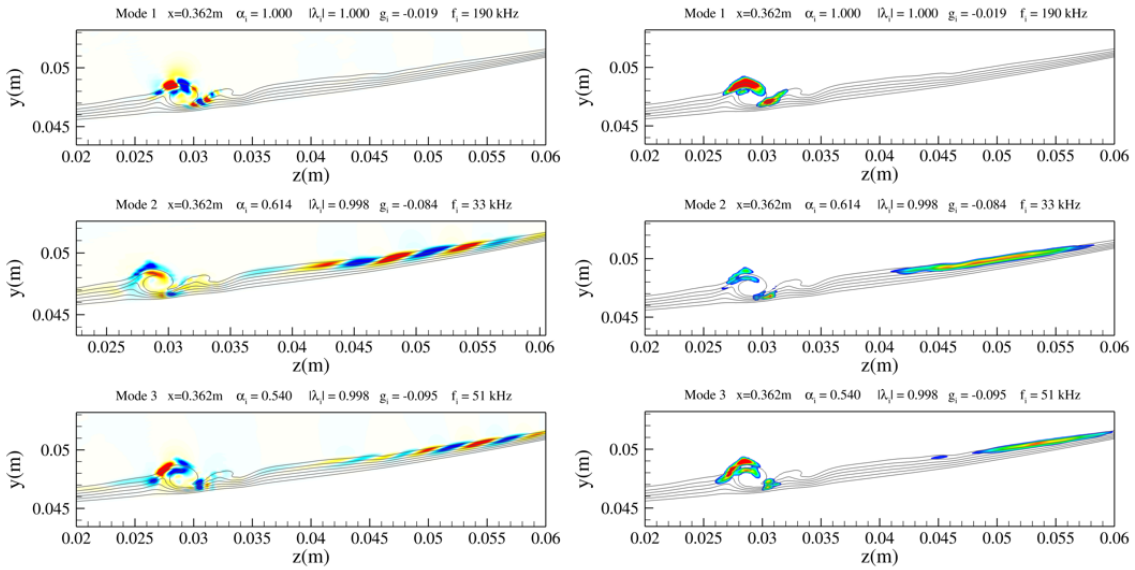

Figure 4.11: Leading STDMD modes of streamwise velocity extracted at x/L = 0.979.

Table 4.4: Local Wave Properties of Crossflow Modes

x/L	Mode	$f(kHz)$	$\phi(deg)$	$\lambda(mm)$	$\delta(mm)$	$u_e(m/s)$	λ/δ	$f\delta/u_e$	c_{ph}/u_e
0.740	1	35	66	1.1	0.84	753	1.3	0.039	0.05
	2	56	70	3.3	0.95	753	3.5	0.070	0.25
	3	42	70	3.3	1.14	761	2.9	0.063	0.18
0.812	1	35	73	5.0	0.90	758	5.5	0.042	0.23
	2	52	69	1.4	0.99	750	1.4	0.069	0.10
	3	69	72	1.6	0.73	753	2.2	0.067	0.15
0.896	2	53	67	3.9	1.02	755	3.8	0.072	0.28
	3	35	67	4.8	0.97	757	4.9	0.045	0.22
0.957	2	35	70	3.9	0.99	765	4.0	0.045	0.18
	3	51	67	4.4	1.08	745	4.1	0.074	0.30
0.979	2	35	72	1.8	1.15	753	1.6	0.050	0.08
	3	51	74	4.6	0.98	753	4.7	0.066	0.31

In order to characterize local wave properties of crossflow instabilities, the same methodology following Knutson et al. [11] was performed. The spatial structures active outboard of the developing crossflow vortices are used to obtain a spanwise wavelength, λ_ζ. The wave angle, ϕ, is defined as the angle between the boundary-layer edge velocity vector and the phase velocity vector. The wave angle is approximately 73° near the swept edge but varies spatially further inboard where the leading modes are identified. The wavelength, $\lambda = \lambda_\zeta \sin\phi$, is the distance between wave fronts in the direction of propagation. The STDMD mode frequency and wavelength obtained from the mode shape is used to approximate the local phase speed, $c_{ph} = f\lambda$. The phase speed is non-dimensionalized by the boundary layer edge velocity, u_e. The scaling of the wave properties are consistent with traveling crossflow instabilities and are a function of wave angle, wavelength, boundary layer thickness δ, and boundary layer edge velocity. All of which are flow quantities that vary spatially due to varying boundary layer properties and potential modal interactions. Therefore, the values of ϕ,λ_ζ, δ, and u_e were taken at the maximum magnitude of the streamwise velocity fluctuation of the STDMD modes.

4.3.2 STDMD: Breakdown to Turbulence

Secondary Instability: Crossflow

Perturbations in the region revealing exponential energy growth are comprised of multiple modes as seen in the previous section. Looking more closely at the high frequency mode contributing the most to the flow dynamics, we can plot the modes of the individual flow variables to gain a better understanding of local flow physics. Figure 4.12 shows fluctuations relative to the meanflow value for streamwise velocity to be correlated with density. The temperature perturbations are shown to be anti-correlated with respect to density since the positive and negative eigenvector

values are denoted as red and blue, respectively. On the inboard side of the larger developing vortical structure, the u- and w-velocity perturbations are positive and v-velocity perturbations are negative. The opposite effects are observed on the outboard side. This suggests the developing vortical structures are supporting large amplitude disturbances taking the form of strong vortical disturbances localized on top of the developing vortical structure. Furthermore, the fluctuations of w-velocity have a slightly larger amplitude than the v-velocity component. The w-velocity disturbance mode shapes associated with traveling crossflow have shown strong signatures along with the v-velocity disturbance mode shapes located primarily outside of the boundary layer edge. Therefore, the presence of the strong v-velocity disturbance signature suggests that this mode is may not be solely characterized by crossflow instabilities. Second Mack mode waves appear to be present in this region as identified by Figure 4.5 and later results support this as well. A modal interaction of second Mack mode and crossflow instabilities is likely but the analysis does not show conclusive evidence. Therefore, the presence of perturbations located on the crest and trough of the developing vortical structures induced by crossflow suggests that this mode is associated with the so called type-II secondary instability of crossflow.

In experiments, the pressure transducer denoted as P1 measured a PSD peak between 175 to 210 kHz and varies depending on Reynolds number located at x/L $\approx$ 0.957. Previous work showed the initial forcing amplitude can vary the PSD peak on the surface as well. The dominant mode identified by STDMD using a forcing level of $P_{RMS} = 0.05\%$ has a strong signature located above the approximate location of the sensor at 185 kHz. Even though the modes of the previous section correspond to streamwise velocity, the mode shapes of all the primitive flow variables show strong signatures highly localized in the same region. Therefore, the mode shapes are sufficient for comparison to wall pressure PSD peaks. The experimental PSD peak range is consistent with the frequency of the mode identified to have the strongest con-

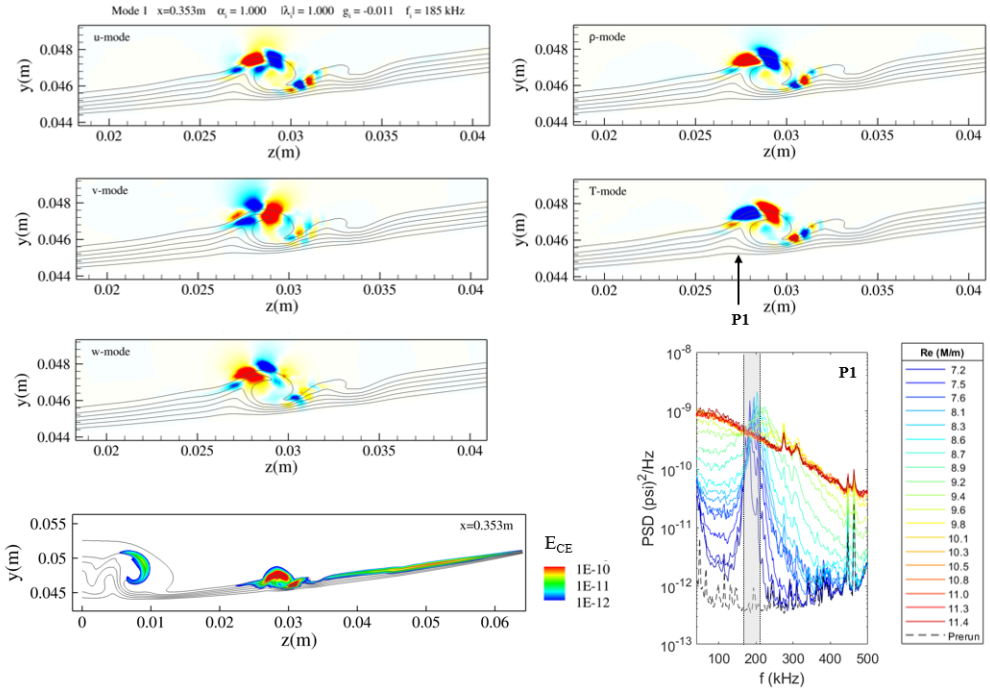

Figure 4.12: Mode shapes of three components of velocity, density, and temperature. Lower left is the time averaged compressible energy distribution plotted on a log-scale. The lower right shows a PSD peak measured by a surface pressure sensor where colored lines correspond to increasing Reynolds Number [15].

tribution on the flow dynamics. Therefore, this suggest the dominant DMD mode associated with secondary instability near developing crossflow vortices is the main source of exponential disturbance energy growth in the region experiencing breakdown in experiments.

Secondary Instability: Travelling Crossflow

Recall, Figure 4.5 depicted turbulent onset with the development of hairpin-shaped vortical structures. This becomes more apparent with the increase in forcing level as shown in Figure 4.13. Breakdown to the small-scale coherent structures represents regions of turbulent onset and the presence of such structures becomes more apparent when applying a larger initial disturbance amplitude spectrum. Additionally with the

increase in forcing level, secondary flow effects in the region of the oblique oriented vortex structures are observed and precedes the fully turbulent region seen by the $P_{RMS} = 0.5\%$ case. Therefore, qualitative comparison shows the turbulent front begins to march forward with an increasing forcing level using the same computational methodology. Even though receptivity is neglected, this reveals the importance of using a high-order, low-dissipation numerical method with an external forcing function to allow disturbances to grow in a physical manner representative of natural transition. This is attributed to the fact that the physical amplitude of the waves are heavily affected by the numerical damping of the numerical method and was explored in previous chapters. Therefore, this exploits that initial disturbance amplitude can directly impact instability excitation and is governed by the critical amplitude of local perturbations that causes the flow to transition.

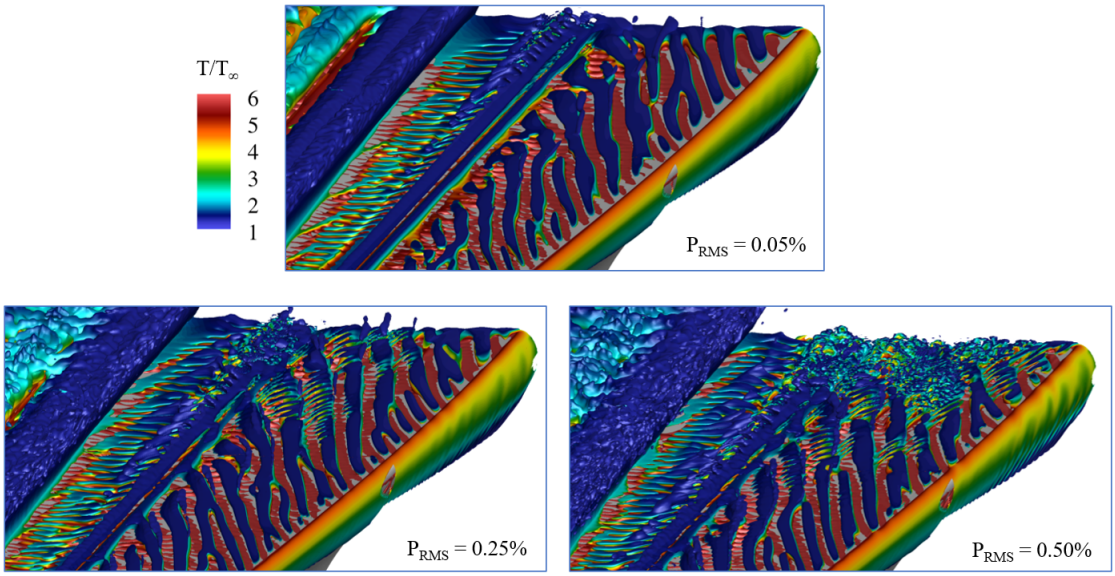

Figure 4.13: Comparison of Q-criterion isosurface colored by local temperature for varying forcing levels.

Figure 4.13 reveals that instabilities develop on top of the primary traveling crossflow structures which precedes the small-scale coherent structures. The flow effect is

apparent in both the $P_{RMS} = 0.25\%$ and $P_{RMS} = 0.5\%$ forcing level cases, with the higher forcing level cases initiating turbulent onset set further upstream. To gain more insight of this flow effect, truncated slice data was collected away from the localized turbulent region for the $P_{RMS} = 0.25\%$ case at x/L = 0.979 between z = 0.036 m and z = 0.063 m. The modes extracted varied from 12 to 61 kHz depending on the truncation level. The first and the third modes are shown in Figure 4.14 with the mode shapes of u-, v-, and w-velocity components. The magnitude of the eigenvectors of Mode 2 identified by STDMD is much lower than Mode 1 and Mode 3, and is located away from the location outboard of z = 0.045 m. For this reason, Mode 2 is not shown. Therefore, Mode 1 and Mode 3 both show strong signatures located between z = 0.036 m and z = 0.045 m and near the region experiencing a large increase in local disturbance energy.

The mode shapes for Mode 1 are consistent with the traveling crossflow modes shown previously but with a lower frequency of 27 kHz. As for Mode 3, the mode shape is significantly different with the spatial structure showing evidence of smaller wavelength structures and at a frequency of 60 kHz, approximately twice the frequency of Mode 1. The mode shapes for v- and w-velocity components show strong signatures and are localized above and below the spatial structures of Mode 1. This suggests secondary flow effects in a region dominated by travelling crossflow instabilities are developing on top of the primary waves representing travelling crossflow and precedes the turbulent onset closer to the swept edge. This is consistent with how high-level, acoustic environments excite travelling crossflow instabilities for non-axisymmetric geometries observed in conventional wind tunnels like what as been seen for HIFiRE-5 and BoLT in the past. In experiments of noisy wind tunnel experiments, the transition front of BoLT and BoLT-2 often results in a "saw-tooth" shaped surface heating pattern. This flow behavior of travelling crossflow seen here is a possible explanation in the case of high initial amplitude disturbance levels.

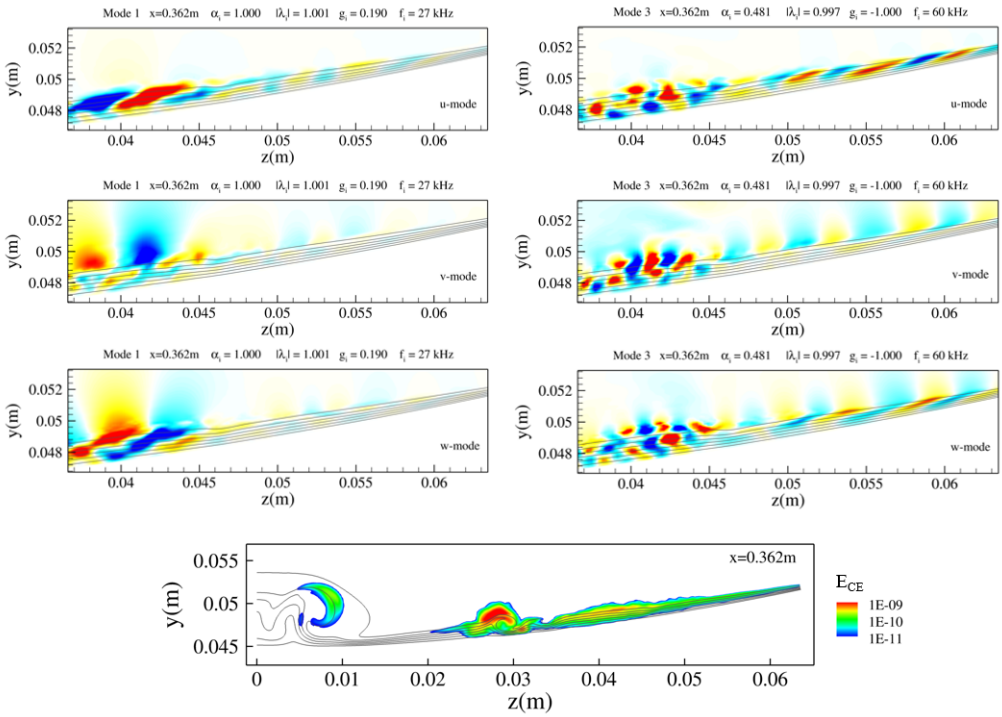

Figure 4.14: STDMD mode shapes of three components of velocity Mode 1 (left) and Mode 3 (right) located outboard of stationary crossflow vortices at x/L=0.979 with $P_{RMS} = 0.25\%$ forcing level. Time averaged compressible energy is plotted on a log-scale (bottom).

4.3.3 SPOD: Verification

Clearly, the modal methodology introduced using the STDMD algorithm with a compressible energy norm weighting is capable in accurately extracting DMD modes associated with boundary layer transition mechanisms from stochastically forced DNS datasets. However, this requires that the user has some intuition as to what physical flow processes are present or are expected such that accurate spatio-temporal modes are retained. To ensure this, the STDMD rank threshold can be tedious to explore for a general case even though the streaming algorithm is highly favorable for large datasets. Nonetheless, it is more appealing to have modal analysis tool that does not require as much time for the user to selectively identify the most dominate modes.

Therefore, spectral proper orthogonal decomposition (SPOD) is another modal analysis tool which was applied since it was used instead for extracting spatio-temporal modes of datasets at flight conditions. The leading modes from STDMD should in theory be the same as SPOD for this particular dataset since DMD modes can be thought of as statistically optimized SPOD modes and so the modes can be interpreted in the same way.

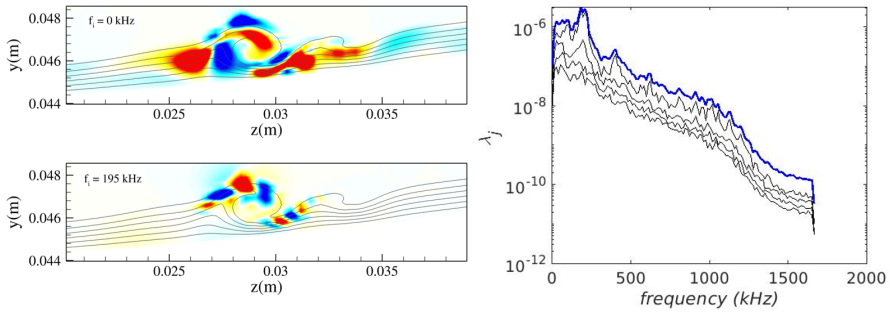

Figure 4.15: Leading SPOD mode at $f = 0$ kHz and $f = 195$ kHz. The 2D SPOD modes plotted correspond to fluctuations in streamwise velocity relative to the mean value. The right plot corresponds to the modal energy of the entire dataset.

To demonstrate this, the same dominant mode which was identified to initiate breakdown using STDMD is extracted using SPOD for the same dataset. Additionally, SPOD was performed on three-dimensional subdomains instead of computational planes as well. The modal energy spectrum of the three-dimensional dataset is shown on the right side of Figure 4.15. On the left, 4.15 shows the leading SPOD mode which contains the highest modal energy peak having a frequency of 195 kHz. Note that the perturbation values are relative to the baseflow value here revealing a zero frequency mode associated with excitation of stationary crossflow instability. Furthermore, the zero-frequency mode reveals three distinct regions of shear denoted by the interface between positive and negative eigen-mode values located within the developing vortical structure. This suggests that the leading non-zero frequency mode corresponds to the secondary type-II instability mode of crossflow since the SPOD

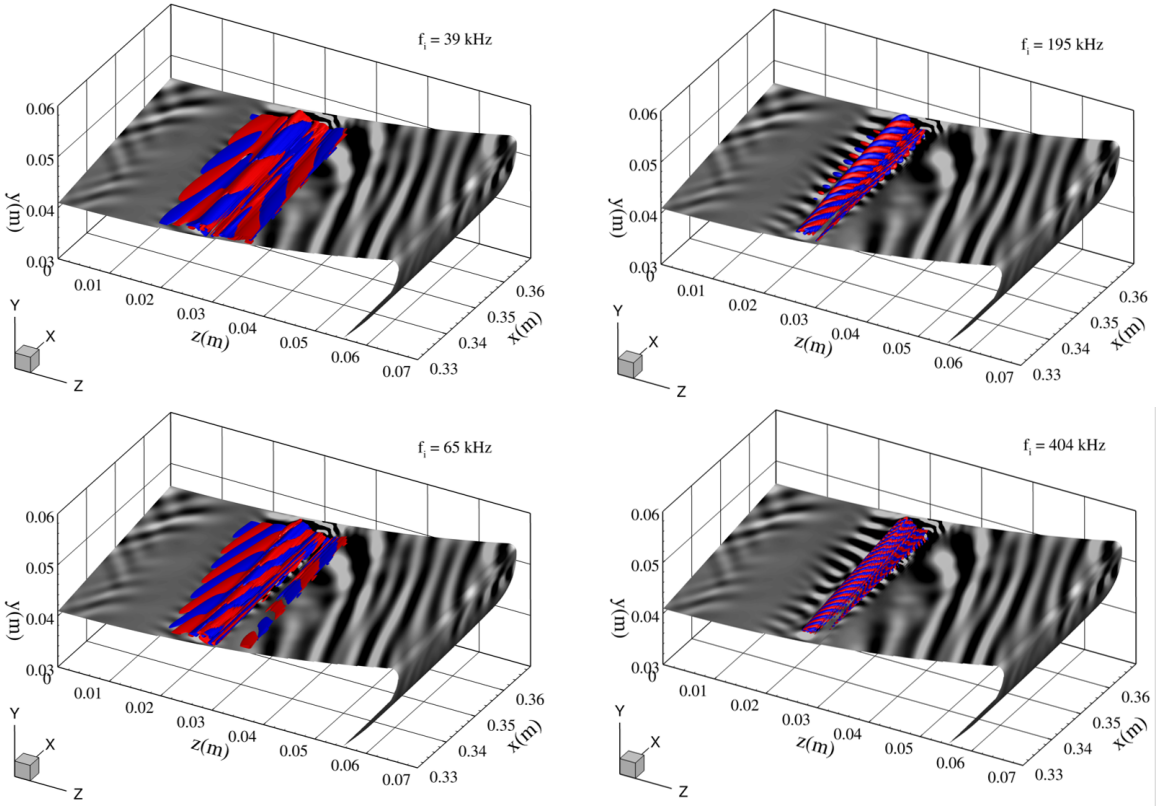

Figure 4.16: Three-dimensional SPOD mode shapes of the leading modes identified to have the largest peaks contributing to the modal energy spectrum. The isosurfaces correspond to streamwise velocity where the red is a positive value and the blue is negative with respect to the mean value. The grey scale shows surface pressure perturbations.

mode of the 195 kHz frequency shows the strongest signatures are located on top of the zero frequency mode where velocity gradients are highest.

The SPOD modes which have the largest modal energy peaks of the frequency spectrum are plotted as three-dimensional mode shapes in 4.16. Upon close inspection, the 195 kHz mode here reveals the excitation of a second Mack mode instability inboard of the developing vortical structure having close to the same frequency. Furthermore, a high frequency SPOD mode appears to show a subharmonic of the primary mode with a frequency of 404 kHz. Because the flow is experiencing breakdown

near the developing vortical structures, both STDMD and SPOD identify a significant modal signature at every discrete frequency near the localized regions since the frequency spectrum is becoming broadband locally. Nonetheless, both STDMD and SPOD do an excellent job in identifying the dominant mode associated with strongly nonlinear flow behavior in the presence of multiple types of instabilities that coexist. From experience, this identification becomes increasingly difficult if regions containing broadband turbulent flow structures are included in the datasets for modal analysis.

4.3.4 Comparison to Experiments

Surface Pressure Spectra

The surface pressure fluctuations were computed on the wall using the instantaneous pressure perturbations and are non-dimensionalized by the values from the baseflow solution. This can be found in Figure 4.17 where it is clear that the pressure perturbations grow when travelling downstream. For consistency, these plots share the same scale to observe the transition front containing significantly stronger pressure perturbations. Instantaneous pressure distributions show imprints of boundary layer instabilities onto the surface. From experience, the onset of transition within the BoLT-2 typically corresponds to pressure fluctuations relative to the baseflow value on the surface that are typically above 1% for the simulation setup shown. However, this is only an observation and should not be necessarily used to dictate the state of the boundary layer. This is because second Mack mode instabilities typically have a larger surface pressure signature since the fluctuations are closer to the wall than those induced by crossflow or vortical instabilities further away from the wall.

High-frequency pressure transducers were placed on the wind tunnel model near the region where surface pressure perturbations were highest and the locations are shown in Table 4.5. This is common practice for experiments where the frequency

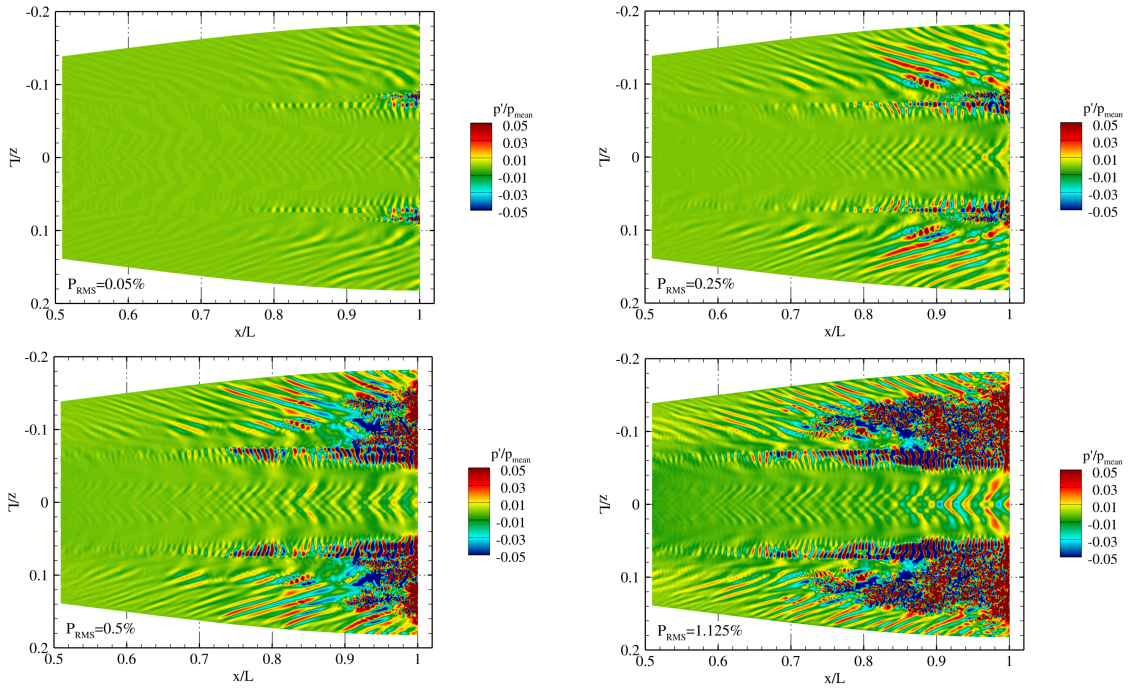

Figure 4.17: Surface pressure perturbations: instantaneous pressure normalized by baseflow pressure distribution

Table 4.5: Pressure sensor locations

Sensor	x/L	z/L
P1	0.957	0.073
P2	0.980	0.069
P3	0.980	0.043
P4	0.980	0.060

content on the surface can help identify at what condition and location evidence of instabilities are present. Therefore, the frequency content of the wall disturbance signal was collected in the simulations, and the power spectral density (PSD) was computed to make comparison to the frequency content of the pressure spectra measured in the experiments [15]. To be consistent with experiments, the PSD was computed using a Pwelch method. Figure 4.18 shows the comparison of the wall pressure disturbance signals and agreement with the frequency content measured in experiments is

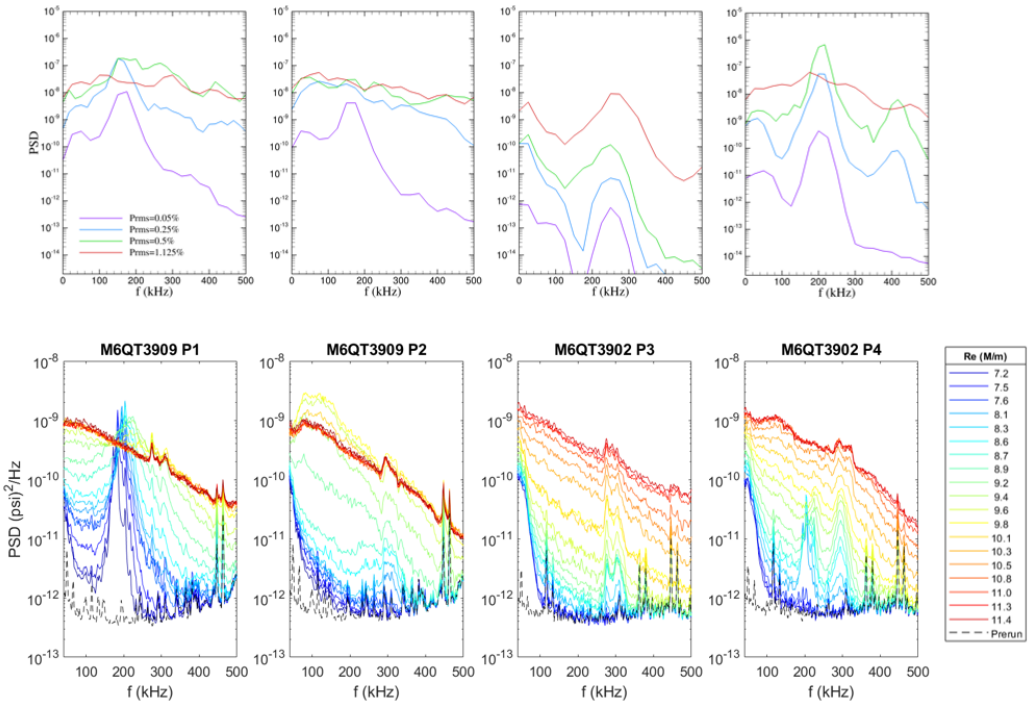

Figure 4.18: Comparison of wall pressure disturbance signal of increasing initial amplitude spectrum level of simulations at freestream conditions with $\mathrm{Re/m} = 10.8 \times 10^6$ (top) and increasing freestream unit Reynolds number of experiments [15] (bottom).

observed. Furthermore, increasing the forcing amplitude has similar trends to increasing Reynolds number of the experimental data. The pressure sensor location denoted by P1 was introduced previously and shows excellent agreement with a strong signal at 195kHz. Interestingly, this signal is apparent even at the low Reynolds number conditions of the experiment. A wide range of frequencies are reached with an increase in initial disturbance amplitude. The second pressure sensor, P2, experiences a similar frequency content as P1 where there is the strong signal at approximately 200 kHz. However, it reaches a broadband frequency range with a slight increase in forcing amplitude. As for P3, a weak signal slightly under 300 kHz is captured where energy content of the experimental pressure data experiences a similar trend. However, this is a region which experiences a small amount of amplification relative

to the other sensor locations. As for P4, a strong signal is captured at 200 kHz. An increase in the forcing amplitude produces a resonating signal at this location that is two times the frequency of the original signal captured and is consistent with the SPOD results shown previously.

Surface Heating

To quantify surface heating, a time averaged heat transfer coefficient was computed by collecting time-series data for heat flux which was then non-dimensionalized by the freestream conditions to obtain the Stanton number.

$$St = \frac{q_w}{\rho_\infty U_\infty c_p (T_0 - T_\infty)}$$

Elevated heating originates where the leading boundary layer modes were identified for the lower forcing level cases. By increasing the forcing amplitude further, the fluctuations seen in the heat flux of the instantaneous solution grow downstream. The instantaneous Stanton number distribution show progression upstream when increasing the initial amplitude level. The perturbations seen in the surface heat flux originate on both sides of the downwash of the developing vortex structure which results in thinning of the boundary layer. Observation of the instantaneous solution of the $P_{RMS} = 0.05\%$ case shows the perturbations are normal to the flow on the inboard side, and higher frequency perturbations on the outboard side appear when travelling downstream. With increasing the forcing level, the perturbations on the outboard side begin to interact with the oblique perturbations closer to the swept leading edge.

Figure 4.20 shows a qualitative heat flux comparison for the same 25% subscale 1.5 meter geometry. The time-averaged heat flux from simulation is taken from the $P_{RMS} = 0.25\%$ case. Recall, a smooth model is assumed for the computations where

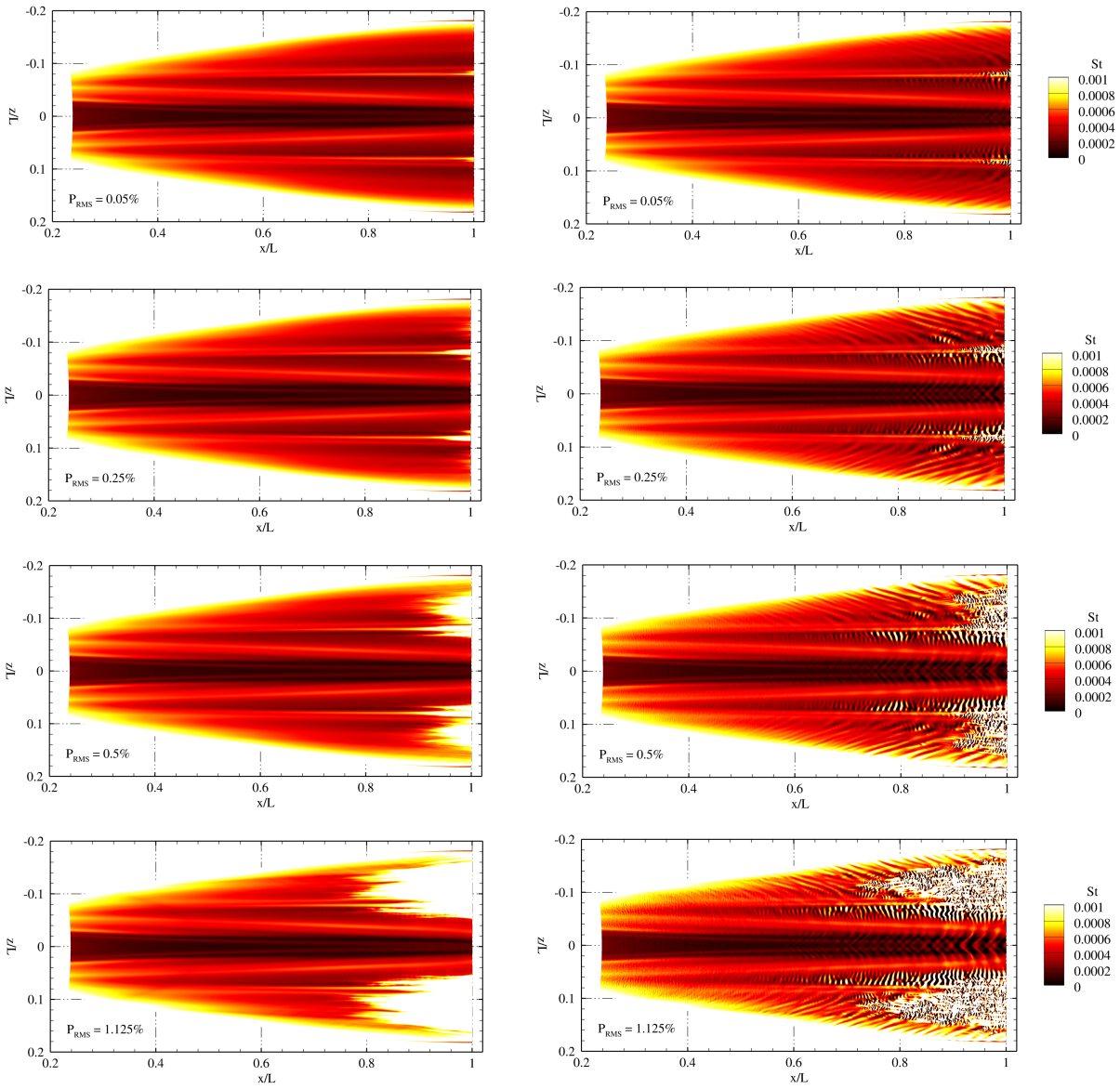

Figure 4.19: Stanton Number distribution with varying forcing level: time-averaged (left) and instantaneous (right).

the freestream condition corresponds to a unit Reynolds number of 10.8×10^6 at Mach 5.9. The thermal image is taken of the surfaced finished machined model at the same Mach number. However, notice that the localized heating is first observed around a unit Reynolds of 10×10^6 in experiments. In order to quantify the surface heat

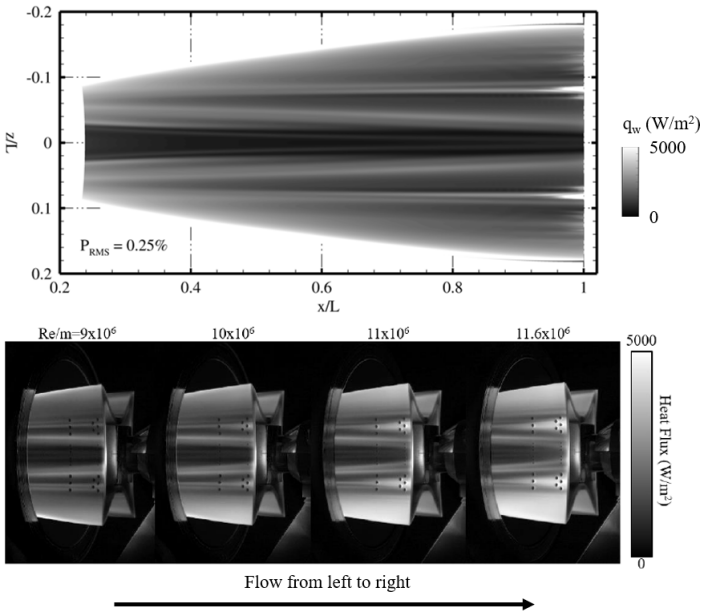

Figure 4.20: Qualitative surface heat flux comparison with same model from experiments. Note that the model compared to is the 25% scaled model of the 1.5 meter geometry from [15].

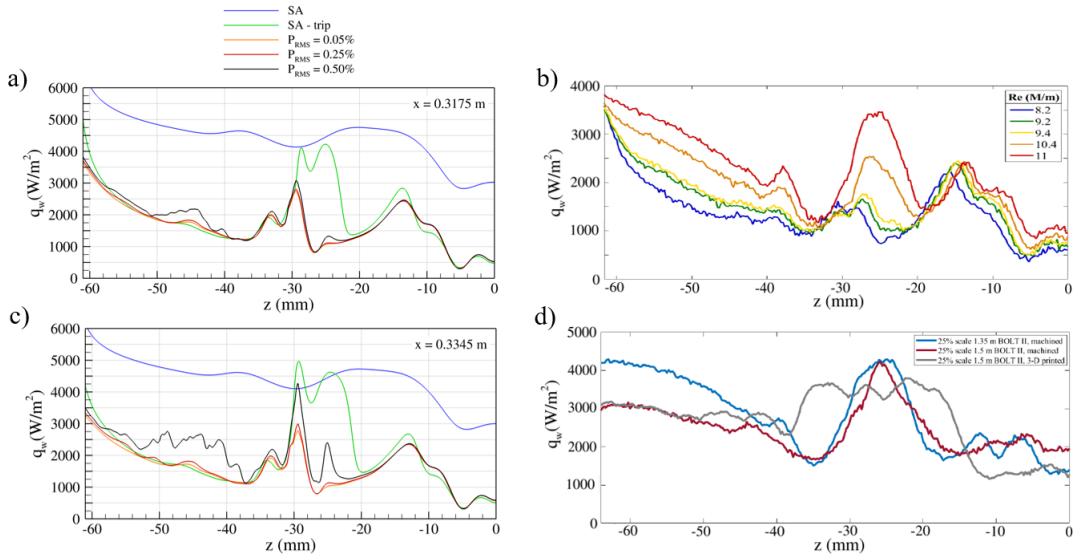

Figure 4.21: Quantitative surface heat flux comparison with 25% scaled version of 1.35 meter geometry from experiments [15] at 0.3175 m (top). Comparison of heat flux at 0.3375 m for three different experimental models (bottom).

flux, surface line extracts were taken at close to the same x-coordinate locations as extracted from the thermal images. Figure 4.21 depicts this where 4.21a) are surface heat flux line extractions located at x = 0.3175 m. A comparison with the Spallart-Almaras (SA) turbulence model, SA with a trip term, and using the various forcing levels for forced DNS are plotted together. The details of the turbulence modeling methodology can be found in [95]. 4.21b) shows the surface heat flux for the the 25% subscale version of the 1.35 m at various flow conditions. Comparison between the forcing level case of $P_{RMS} = 0.25\%$ from 4.21a) and unit Reynolds number of 10.4×10^6 from 4.21b) show the closest agreement. Very similar surface heat flux peaks are observed. However, note that the locations of the peaks are slightly different than the experimental data. It is unclear whether this is attributed to a slight yaw angle or projection angle from the three-dimensional wall to the IR camera lens. This is because it should be noted that the local grid spacing is much finer than the spacing of a single pixel from the image. Nonetheless, the peak heat flux values show excellent agreement with the experimentally measured values despite the locations being slightly different. As for the turbulence model solution, the fully active SA model significantly over-predicts the surface heat flux. This is seen in 4.21c) where the turbulence model over predicts the surface heat flux everywhere except where transitional heating exists. For this reason, the user specified trip version of the SA model was used and gives an overall improved approximation of the surface heat flux for this particular case. However, the DNS case using a forcing level of $P_{RMS} = 0.25\%$ proves to match closest with the heat flux peak values from experiments.

Flowfield Fluctuations

The local mass flux from DNS is interpolated onto planar slices for the 10.8×10^6/m conditions for the various forcing levels at x = 0.3175 m and are shown in Figure 4.22. For reference to experiments, the hot-film bridge voltage are represented as a 2-D

contour map for the Re = 10.4×10^6/m case at the same x-coordinate location. The hot-film bridge voltage was used to compute a mass flux using a mass flux correlation with calibration constants by Kostak-Teplicek [15]. From Figure 4.22b), the black line in the lower part of the contour plot represents the surface of the BoLT-2 model. As described by Kostak-Teplicek [15], the intersections of the grid represented by the black lines are the locations of measurements collected with the hot-film. Qualitative comparison reveals that the off-surface structures match well despite the streamwise locations and flow conditions being slightly different. Overall, the regions where the mass flux gradients sharpen with respect to increasing forcing level correspond to regions where the flow state is transitioning to turbulence and is consistent with experiments.

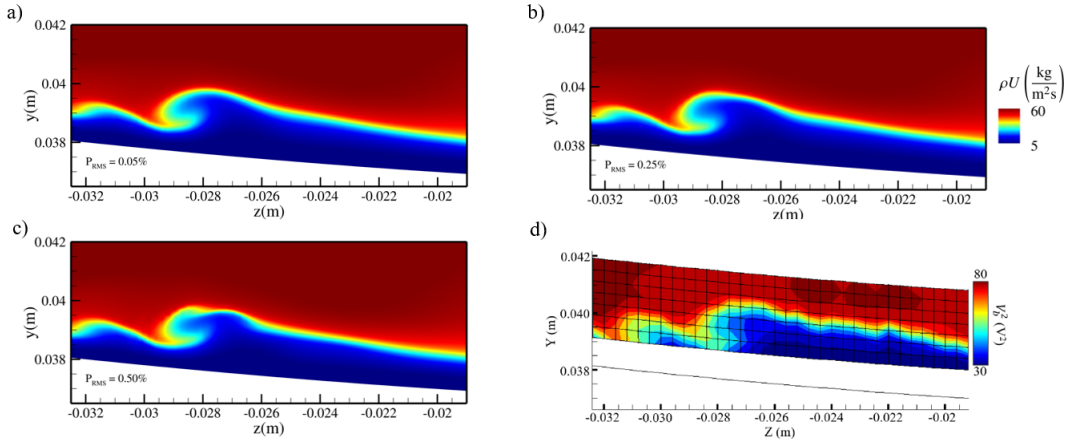

Figure 4.22: Mass flux at various forcing level cases with Re = 10.8×10^6/m freestream condition at x = 0.3175 m compared to experiment at the same location with Re = 10.4×10^6/m freestream condition [15].

The streamwise RMS fluctuations relative to the time-average value are plotted on a log-scale for the unit Reynolds of 10.8×10^6/m and forcing level of P_{RMS} = 0.25% are plotted in Figure 4.23a). For experiments, denoted by Figure 4.23b), the RMS value is calculated for reference from the bridge voltage fluctuations measured by the hot-film instrumentation located at x = 0.2925 m with the freestream unit

Reynolds number of 10.4×10^6/m. Qualitative comparison of Figure 4.23a) and 4.23b) shows that the largest fluctuations correspond to where flow is transitioning. The regions denoted by red for computations correspond to where second Mack mode and crossflow instabilities are supporting modal growth of local disturbances. Slight deviations with the experimental RMS voltage fluctuations are present and is likely because this is not necessarily a direct comparison of discrete streamwise velocity RMS values, and the RMS values are highly dependent on the forcing level used in computations. Nonetheless, the location and shape of where perturbations are most amplified are qualitatively similar between computations and experiment.

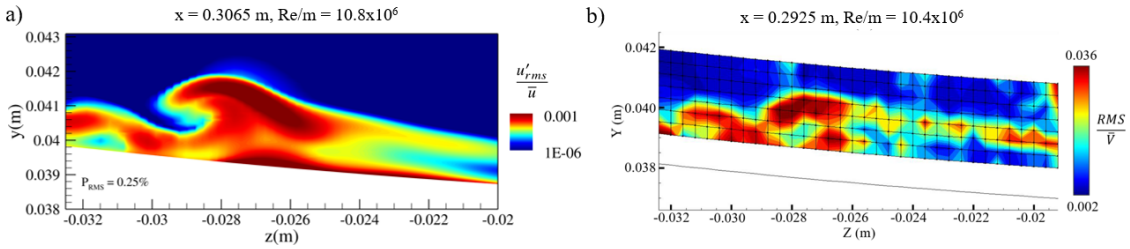

Figure 4.23: Streamwise velocity RMS fluctuations relative to the time-averaged value from simulation plotted on a log-scale using a forcing level of $P_{RMS} = 0.25\%$ and Re/m $= 10.8 \times 10^6$ at x = 0.3065 m. Measurements are the RMS normalized by the mean voltage obtain from hot-wire measurements at Re/m $= 10.4 \times 10^6$ and x = 0.2925 m [15].

4.4 Chapter Summary: Subscale Conditions

It was introduced that by following the proper numerical methodology, the forced DNS approach can be used to simulate natural transition of the BoLT-2 flowfield using a stochastic forcing function. Furthermore, high-fidelity solutions of the Navier-Stokes equations were obtained using a carefully generated grid with improved manual shock alignment and accurate resolution that are sufficient to capture high frequency flow processes. This is achieved using a combination of low-dissipation fluxes and a

shock capture method that tailors numerical dissipation at the bow shock and regions that are numerically unstable. Therefore, the proposed computational methodology is capable of simulating natural transition and predicting an accurate disturbance response within the BoLT-2 flowfield representative of breakdown.

Introducing disturbances meant to be representative of quiet wind tunnel noise has enabled the study of nonlinear disturbance growth using an approach consistent with experiments. STDMD with a compressible energy norm weighting and SPOD has been used to extract modes associated with boundary layer transition processes from forced DNS datasets obtained using a sufficient sampling rate. The leading modes identified using the modal analysis methodology has allowed for the identification of various crossflow modes with corresponding frequencies, wavelengths, and wave angles. The dominant mode appearing later in the transition process has been identified to have a much higher frequency due to secondary flow behavior of crossflow contributing to breakdown. Furthermore, modal interactions are present and involve disturbances, excited by second Mack mode and crossflow instabilities, being supported by developing vortical structures induced by crossflow. Note that the CFD in this work assumes a perfectly smooth model and zero angle of attack and sideslip for simplicity. Additionally, the modal analys performed extracted other modes associated with crossflow instabilities ranging between 50-80 kHz from the DNS at localized regions which matched with experimentally measured frequencies [15]. These modes were not shown for brevity and because they were not deemed to have a physically significant contribution to breakdown to turbulence in the simulations. Therefore, only the dominant modes associated with a significant contribution to the nonlinear stages of the transition process were shown in this work.

The frequencies of the most physically unstable instabilities of the simulations share excellent agreement with dominant frequencies present in experiment. However, note that the placement of the pressure sensor measurements in the experiment

are extremely sensitive to the location relative to the off-surface instabilities. This is because, in some cases a pressure sensor may not be located below instabilities because of the tolerances from machining or flow state deviations related to model orientation inside a wind tunnel. Furthermore, quantities calculated from measurements such as hot-wire voltage RMS derived values and 1D temperature measurement used for calculating the heat flux from IR thermography requires more uncertainty quantification. Therefore, some discrepancies with the experimentally obtained spectral data are observed and likely contributions are a finite amount of distributed roughness on the experimental model altering the flow state and more importantly the tunnel noise level is not well characterized. For this reason, various forcing levels were simulated which show agreement with experiments. Additionally, the uncertainty related to the actual tunnel disturbance environment could cause potentially new frequency spectra to be present in measurements that the DNS may not realize or modal analysis may not deem as dominant off-surface modes. Therefore, the disturbance source and surface roughness should be further quantified in experiments and imposed as a boundary condition for instabilities of simulations to make direct comparisons with wind tunnel data to reduce uncertainty when making comparisons in the future. Nonetheless, the most physically unstable instabilities contributing to breakdown are well represented in experiments and resolved in simulations.

For computations, stochastic forcing of the DNS solution accounts for all possible eigenvalue solutions allowing for the boundary layer to select a response representative of natural transition to identify the most unstable flow processes. Future work should aim at addressing more realistic forcing functions to account for realistic receptivity mechanisms. For this reason, the receptivity process was neglected by introducing disturbances post-shock to focus on quantifying the physical mechanisms of the BoLT-2 flow state contributing to breakdown. This has allowed for the verification of a numerical methodology capable of identifying the most unstable boundary layer

modes of the physical flow state which is needed for predictive stability analysis of transition in flight.

Chapter 5

BoLT-2 Simulation and Analysis at Flight Conditions

5.1 Steady Flow State

Wind tunnel setup to flight setup: Viscous Effects

To first understand how the flow state varies from geometry scaling and ground test conditions to flight conditions, various flow conditions were simulated for the 25% scaled and full-scale geometries. For ease of computation and analysis, the nose tip portion of the geometry was simulated to understand how the crossflow inflection point in the boundary layer upstream influences the developing vortical structures downstream. For direct comparison, quantities are non-dimensionalized by their respective simulation values and geometric length scales. The unit Reynolds number for the conditions is chosen to be close to the maximum Reynolds number condition under quiet flow conditions in the Mach 6 Quiet Tunnel (M6QT) at Texas A&M University. The flight conditions here are selected from points along the projected nominal flight trajectory before the flight test was conducted and not from the actual flight trajectory. In the actual flight trajectory, the vehicle experienced Mach Numbers just over 6. Nonetheless, the flight condition of interest was chosen to have the

same unit Reynolds number to help interpret how the viscous effects may alter the flow state.

Definition	Value
Nose radius, r_f	5 mm
Characteristic length, L_f	1.0 m
Truncated length, $L_{f,t}$	0.1 m

Table 5.1: Flight Configuration

Definition	Value
Nose radius, r_s	1.25 mm
Characteristic length, L_s	0.25 m
Truncated length, $L_{s,t}$	0.025 m

Table 5.2: 25% Subscale Configuration

Condition	M_∞	U_∞ (m/s)	ρ_∞ (kg/m^3)	T_∞ (K)	T_{wall} (K)	Re (m^{-1})
Subscale (1)	5.9	870.3	0.0418	52.15	300	10.3×10^6
Nominal Flight (2)	5.6	1645.3	0.0895	216.96	300	10.3×10^6
Nominal Flight (3)	5.5	1658.4	0.0231	230.85	300	2.57×10^6

Table 5.3: Freestream Conditions

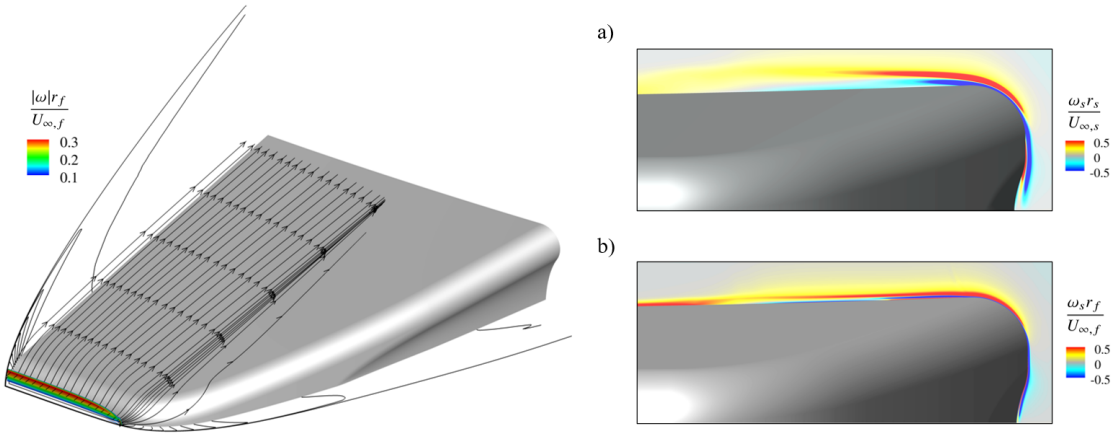

Figure 5.1: Left shows streamlines originating from regions with high vorticity magnitude for the flight configuration. Normalized streamwise vorticity is show on the right for a) the subscale configuration at condition 1 and b) flight configuration at condition 2.

To first demonstrate the effects of higher Reynolds numbers relative to lower Reynolds numbers observed in previous work, the baseflow state is computed using

the conditions from Table 5.3. Recall, the inviscid flow state described by Thome et al. [94] showed that the distribution of vorticity on the top surface contains two distinct regions with highly localized vorticity magnitude near the centerline and close to the swept leading edge. Figure 5.1 shows how the vorticity magnitude is distributed post-shock where the streamwise vorticity component (not shown) is largest closer to the centerline and partially contributes to the centerline roll-up downstream. Another vorticity contribution to the centerline roll-up originates where the surface of the two-dimensional cylindrical nose tip revolves to a swept leading edge. Furthermore, the left plot of Figure 5.1 shows streamlines near the wall, originating from the post-shock region with the highest shock curvature. The local pressure gradients alter the path and the streamwise vorticity is negative as denoted in the bottom, right. Note that local boundary layer edge streamlines have positive streamwise vorticity near the swept leading edge but are not shown. Furthermore, Figure 5.1a) and 5.1b) reveal an inflection point, characteristic of crossflow, located at the positive and negative interface of the streamwise vorticity distributions. The streamwise vorticity distribution for the flight configuration is more compressed near the wall due to the thinner boundary layer relative to the subscale configuration. This is important to keep in mind since the vorticity distribution and crossflow inflection point have a significant influence on the boundary layer state downstream.

In order to quantify viscous effects, a normalized skin friction coefficient is calculated for comparison since scaled geometries and flow conditions are directly compared. The purpose of this is to help elucidate the difference in viscous effects of the subscale configuration at wind tunnel conditions and the full scale configuration at flight conditions. The combination of flow conditions and geometry scaling have a significant influence on crossflow and this directly affects the skin friction. Therefore, the magnitude of the wall shear stress is calculated and non-dimensionalized by the corresponding freestream values. Next, the skin friction coefficient is normal-

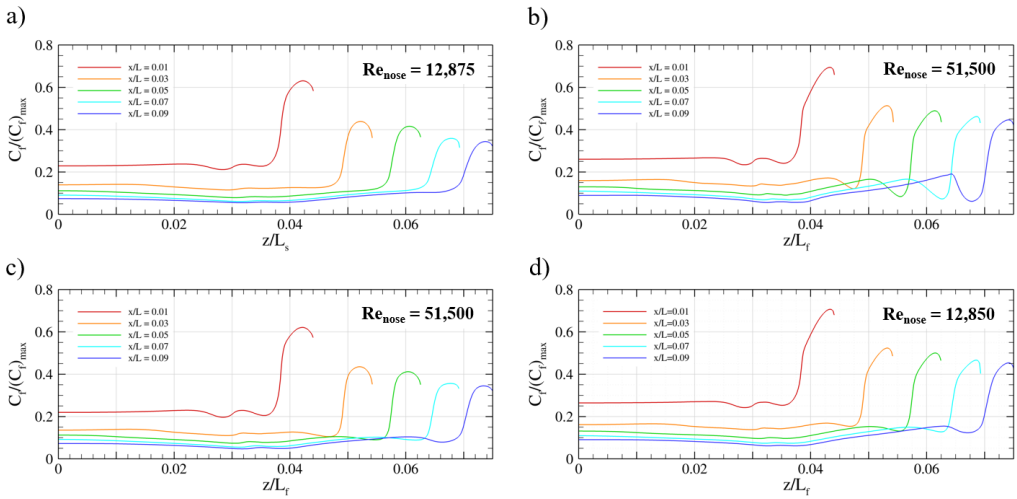

Figure 5.2: Normalized skin friction coefficients: a) subscale configuration at condition 1, b) flight configuration at condition 2, c) flight configuration at condition 1, and d) flight configuration at condition 3.

ized by the maximum skin friction coefficient on the wall and is located where the two-dimensional cylindrical nose tip revolves to a swept leading edge for all cases. The normalized skin friction allows for a direct comparison of the surface profiles. Figure 5.2 shows the normalized skin friction coefficients where 5.2a) and 5.2c) are the same flow condition for the 25% subscale geometry and full-scale geometry, respectively. By scaling down the geometry, the trends of the normalized skin friction profiles of 5.2a) demonstrate that the flow state is representative of a slightly lower Reynolds number compared to 5.2c) which has a different nose tip Reynolds numbers.

5.2b), 5.2c), and 5.2d) are the full-scale geometry but at different freestream conditions. By observation, a comparison of the normalized skin friction profiles of 5.2c) and 5.2d) shows agreement and suggests that the boundary layer state using a wind tunnel condition (condition 1) scales approximately with the Reynolds number of a flight condition (condition 3) by a factor of 4. This is for the same geometry and isothermal wall temperature, despite having different freestream unit Reynolds numbers and total freestream enthalpies. A comparison of 5.2b) and 5.2c) exemplifies

that the trends of the surface profiles are independent of nose tip Reynolds number. The same trends in the normalized skin friction are also observed in the normalized heat transfer coefficient. Figure 5.3 reveals how the heat transfer coefficient on the surface compares between the targeted cases, 5.3a) and 5.3b). Therefore, the normalized skin friction and heat transfer coefficient profiles reveal how wall quantities change with respect to viscous effects induced by the near wall crossflow inflection point. Note that the nose tip solution in 5.2a) and 5.3a) is representative of the wind tunnel condition investigated in the previous chapter.

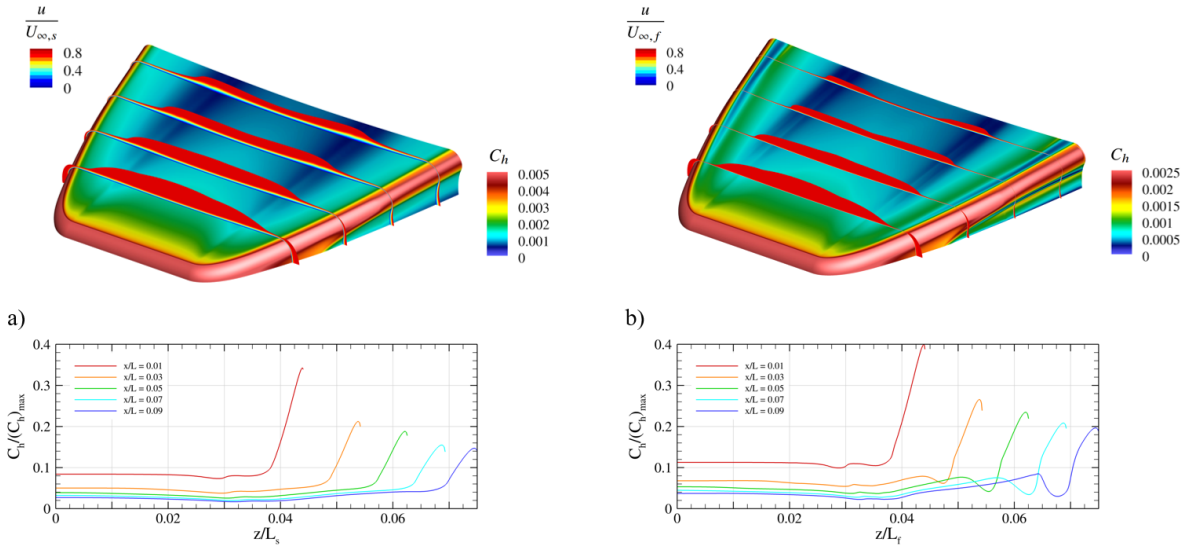

Figure 5.3: Steady-state flowfields of a) subscale configuration at condition 1 and b) flight configuration at condition 2. Streamwise velocity is normalized by the freestream value and the wall contours are the local heat transfer coefficients. Spanwise slices of the normalized heat transfer coefficients are below.

5.1.1 Baseflow State at Flight Condition

The viscous effects from the last section are governed by varying pressure gradients and contribute to the developing vortex structures downstream which are able to support various types of instabilities. At subscale wind tunnel conditions, the boundary

M_∞	U_∞ (m/s)	ρ_∞ (kg/m^3)	T_∞ (K)	T_{wall} (K)	Re/m (m^{-1})
6.09	1773.22	0.067	211.0	330	8.6×10^6

Table 5.4: BoLT-2 flight condition from actual flight trajectory. The isothermal wall temperature of this table is approximately the average temperature across thermocouple measurements at the end of the geometry. (Private Communication: Dr. Rodney Bowersox, TAMU)

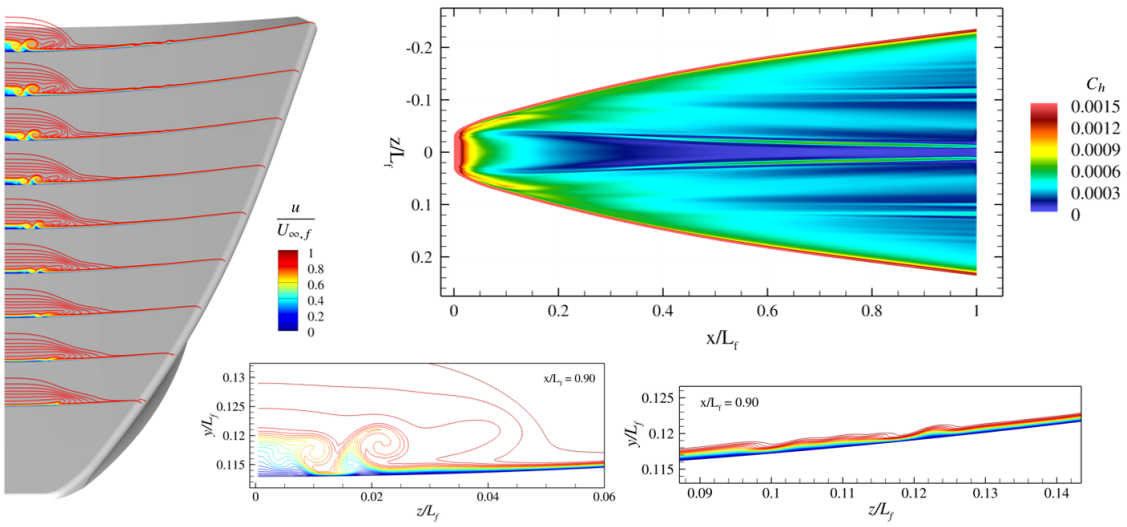

Figure 5.4: Streamwise velocity (left) and heat flux coefficient (right) of the flight configuration for an actual flight condition where the boundary layer was expected to be in a transitional state. The laminar, steady-state solution shown was obtained with first-order DPLR time integration [65].

layer rolls-up between the centerline and swept leading edge. For a longer geometry, as seen from last chapter, developing vortical structures are present which lead to secondary flow behavior which causes transition to turbulence. As for the full scale geometry at a flight condition, Figure 5.4 illustrates how the developing roll-up between the centerline and swept leading edge is significantly different with respective to the subscale setup of last chapter and has close to the same Mach number and unit Reynolds number. The most apparent difference is observed near the large-scale counter rotating vortex structures close to the centerline at which secondary roll-up

produces a vary thin boundary thickness. Based on the current literature, it is unclear how the secondary roll-up near the centerline may drive transition and so analysis later in this chapter investigates this.

5.2 Three-dimensional Perturbation Growth

Before introducing disturbances, a steady-steady solution is converged and is defined as the baseflow state. After the baseflow state is obtained, small amplitude disturbances in the primitive variables are introduced using a sustained, broadband stochastic forcing approach similar to what was used previously. However, now the disturbances are introduced pre-shock. The purpose of this is so that the post-shock flow state produces three dimensional acoustic, entropic, and vortical waves characteristic to the flow state. This is visualized in Figure 5.5 showing temperature mode shapes in the entropy layer which contain very small amplitudes relative to perturbations in the boundary layer. Therefore, this depicts how temperature is affected by three-dimensional waves produced by propagating the disturbances through the shock. This can be thought of the effect that acoustic, vortical, and entropic modes have on temperature at discrete frequencies and represented by single modes obtained with SPOD. The majority of the disturbance energy is contained in the low-frequency range from 5 kHz to 60 kHz, even though high-frequency modes of relatively small amplitude are present as well. Similar global modes have been observed using Input-Output (IO) analysis on cone geometries which take the form of low- and high-frequency mechanisms [105].

The perturbations in the primitive variables are a function of a non-dimensional random number, $r_i \epsilon (-1, 1)$, obtained with a pseudo-random number generator that is computed at each time step. The amplitude, A, is non-dimensionalized and scaled using the Chu [87] energy norm so that the disturbance energy is very low relative

to the total freestream energy. E_d is the non-dimensionalized disturbance energy, and is set such that the local disturbance energy cannot exceed 0.15% of the total freestream energy. The fluctuations in the five perturbations variables are set such that each value does not exceed 0.3% of the corresponding freestream value. This results in an amplitude, A, of 0.5 being specified. The disturbance forcing approach follows Melander et al. [72],

$$(u_r, v_r, w_r, T_r, \rho_r) = r_i \epsilon(-1, 1)$$

$$E_d = \left[{u_r}^2 + {v_r}^2 + {w_r}^2 + {T_r}^2 \frac{1}{\gamma(\gamma-1){M_\infty}^2} + {\rho_r}^2 \frac{1}{\gamma {M_\infty}^2} \right]^{1/2}$$

$$(u', v', w', T', \rho') = A(u_r, v_r, w_r, t_r, \rho_r) \frac{1}{E_d} \mathrm{diag}(|\tilde{\mathrm{U}}|, |\tilde{\mathrm{U}}|, |\tilde{\mathrm{U}}|, \bar{\mathrm{T}}, \bar{\rho}) \tag{5.1}$$

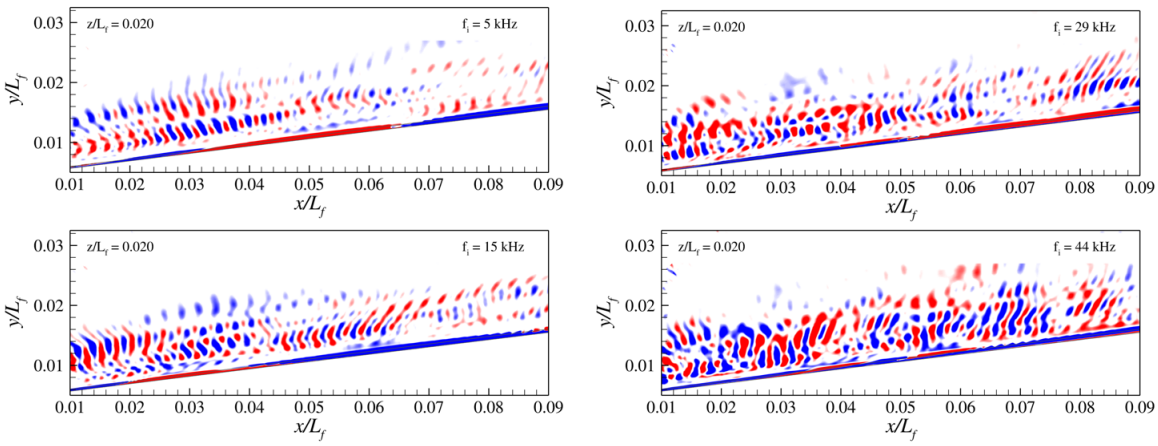

Figure 5.5: Temperature SPOD mode shapes of low-frequency modes in the entropy layer.

5.2.1 Data Collection and Sampling

Because of the size of the grids, the required data storage is prohibitively expensive if the entire solution were stored as a single snapshot for time-series data. Furthermore, it was found that by performing modal analysis on larger datasets make it more challenging to identify relevant modes associated with highly localized amplification due to boundary layer instabilities. Therefore, data was collected by storing cell centered data from cells that intersect specified x- and z-locations and are equally spaced in time. For visualization, the cell centered values were interpolated onto two-dimensional planes in space. The introduced modal analysis approach can be used to extract three-dimensional modes shapes as demonstrated in the last chapter. However, data storage is computationally expensive due to the size of the grid and required sampling. For very large datasets, the amount of memory storage required to post-process was prohibitively expense which limited the analysis to local regions experiencing the largest increase in disturbance energy.

Definition	
Simulation time step	10 ns
Number of Snapshots	2000
Snapshot Spacing	0.2 μs
Sampling Frequency	5.0 MHz
Snapshot Sequence	400 μs
Single Period Wave	2.5 kHz

Table 5.5: High-frequency Sampling

Definition	
Simulation time step	50 ns
Number of Snapshots	1000
Snapshot Spacing	2.0 μs
Sampling Frequency	500 kHz
Snapshot Sequence	2000 μs
Single Period Wave	0.5 kHz

Table 5.6: Low-frequency Sampling

In order to extract pertinent modal information using SPOD, the sampling has to be sufficiently high frequency and long duration to resolve and capture spatio-temporal information. The sampling parameters for low and high sampling rates are summarized in Table 5.5 and Table 5.6, respectively. Note that the sampling parameters are slightly different since different simulation time steps were used and computational resources had to be accounted for. To post-process the solutions and

save time series data for the entire domain, the storage space and potentially the analysis approach would have to change considerably if analysis were performed on the entire domain at once. This undertaking is outside the scope of this work, and therefore data collection and analysis is only conducted on individual slice datasets treated independently for the nose tip simulations. This is consistent with last chapter where modal analysis was performed on individual datasets treated independently as well. As for the downstream SPOD analysis, multiple slice datasets were considered to show how the modes are correlated in space and time.

5.2.2 Grid Resolution and Sampling Convergence

Recall, meshes in this work have grid alignment with the bow shock curvature. This is very important when passing disturbances through shocks since large variations in grid spacing and poor shock alignment can produce a significant amount of dispersion error. Therefore, grid tailoring is applied to ensure the grid is aligned with the bow shock. This is achieved by first computing the maximum of the pressure gradient in the wall-normal direction to locate the bow shock on an initial mesh, redistribute the grid points extending from the wall to the inflow, smooth along grid connected lines, and converge the solution on the tailored grid. If this is not accounted for, the numerical error in some cases can initiate transition aphysically when using high order, low dissipation numerical schemes. Furthermore, it is important that the grid has sufficient resolution to resolve relevant frequency content and to respect the wave damping characteristics of the numerical method used in the external forcing simulations. The grids in this work were create to resolve desired frequencies that correspond to boundary layer instabilities with the highest amplification from PSE at close to the same condition [104]. The necessary grid resolution to properly capture turbulent length scales is estimated to be an order of magnitude greater resulting in grid and connectivity data storage requirements to be prohibitively large. Therefore,

total grid size is restricted and limited by the current data structure capabilities within US3D and is an active area of code development.

The grid used for this chapter encompasses a quarter domain and extends the full length of the geometry resulting in a total of 600 million cells. The target grid spacing located at $x/L = 1.0$ near the centerline is slightly under-resolved in the spanwise direction, since the streamwise grid spacing is approximately one-fourth of the spanwise grid spacing at the end of the domain. The nose tip grids for both the 25% subscale and flight configurations have the same cell spacing distributions in every direction except the wall normal direction. To be clear, the same topology is used for the subscale configuration but the domain is scaled down to 25% of the full-scale size. The spacing of the first cell off the wall is adjusted for each configuration such that the $y+$ remains below 0.1 in the regions of interest. Recent grid estimates show that a $y+ < 0.1$ is sufficient to resolve the viscous stresses near the wall for most DNS calculations [106]. To demonstrate that the grids and sampling are converged for unsteady forcing simulations and spectral analysis, the full length grid is truncated to 28% of the domain length. This is chosen since the baseline grid has half the number of points distributed at the leading edge, half the spanwise grid resolution, and assumes a symmetry plane along the centerline. At the time of this writing, a grid convergence study cannot be carried on the full domain size since it would be prohibitively large with the current data structure capabilities.

Freestream forcing is applied to the truncated domain and the grid dimensions for the flight configuration are in Table 5.7. Time-series data is then collected at $z/L_f = 0.0755$ using the simulations and sampling parameters from Table 5.5 to capture a broader range of frequencies. This is due to the fact that past stability analysis for this geometry estimates modal growth for second- Mack mode frequencies just over 800 kHz along the streamwise location selected. By performing SPOD on the collected time-series, a significant peak in the modal energies at a frequency of 820 kHz is

	Baseline (Quarter Domain)	Fine (Half Domain)
Streamwise Extent (L)	0.28 m	0.1 m
Total cell count	141×10^6	139×10^6
Leading edge points	40	110
Streamwise (ξ) points	1440	620
$\Delta\xi_(x/L = 0.1)$	0.19 mm	0.19 mm
Spanwise (ζ) points	410	1030
$\Delta\zeta(x/L = 0.1)$	0.28 mm	0.18 mm
Wall-normal (η) points	250	250
y^+_{max}	0.4	0.4
$y^+(x/L = 0.1)$	0.05	0.05

Table 5.7: Grid Metrics: nose tip configurations

present. The density perturbation mode shape shown in Figure 5.6 corresponds to a second-mode disturbance where the leading SPOD mode contributes to 90% of the local disturbance energy at the discrete frequency and spatial location. Additionally, SPOD modes shown in later sections are consistent with the modes extracted in the spanwise direction for both grids. This suggests that the baseline grid is sufficient for capturing desired spectral content. To ensure grid convergence, the fine grids were used for modal analysis at the leading edge nose tip. The sampling duration for the nose tip datasets was checked for convergence by sampling for longer duration. It was determined that the same modal energy peaks remained the same, and the values were relatively much higher than the peak of the sampling duration cutoff frequency.

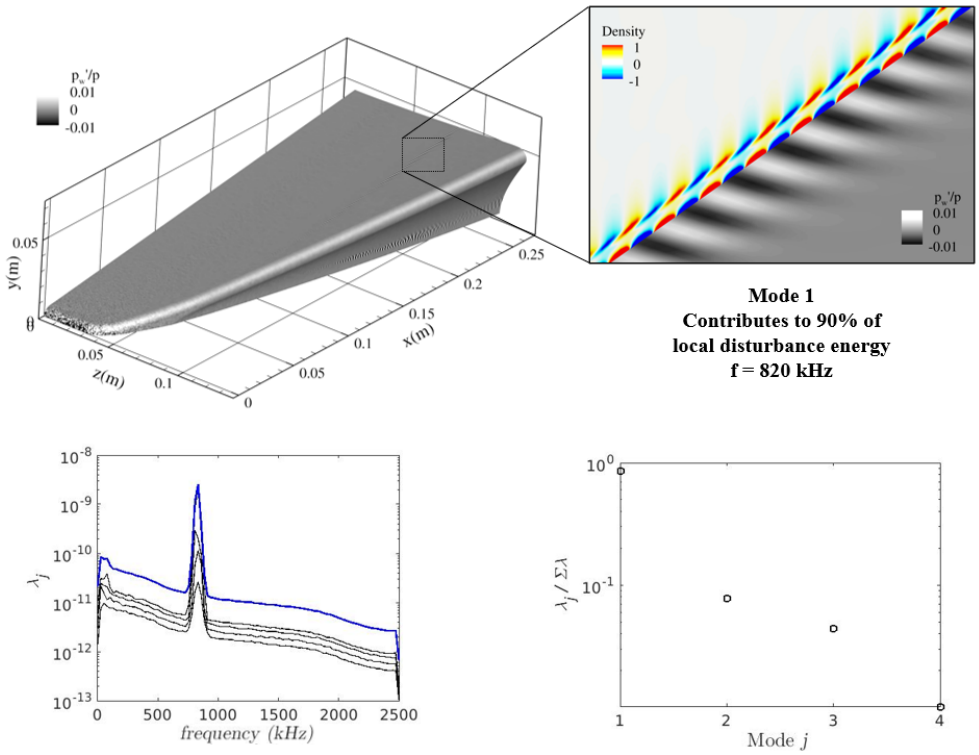

Figure 5.6: Leading SPOD mode shape for data collected at $z/L_f = 0.0755$ of the baseline mesh corresponds to second-mode disturbance and is consistent with PSE estimates in terms of frequency, wavelength, and relative disturbance amplification.

5.3 Transition at Flight Conditions: Freestream Disturbances

5.3.1 Transient Growth Mechanisms

By forcing the flow-state using the numerical approach, streamwise structures develop near the nose tip of the geometry along with excitation of boundary layer instabilities later downstream. As mentioned by Bitter and Shepherd [107], it is common for non-modal growth mechanisms to exhibit the "lift-up" effect [108] and takes the form of streamwise vortices and is similar to the structures near the leading edge. The source that is most likely to excite transient growth mechanisms has been thought

to be roughness since surface roughness acts as a steady forcing source. This is due to the fact that the optimal growth for reattachment streaks within a hypersonic boundary layer occurs for zero frequency temporal wavenumbers with a spanwise spatial wavenumber [109]. Vortical structures within a hypersonic boundary layer of a compression ramp extracted with Input-Output take the form of streamwise streaks and the streamwise velocity perturbations are associated with large, localized peaks in surface heating. A similar response was found for the nose tip of a cone configuration by Melander et al. [72]. This is a possible explanation for the developing streamwise structures contained within the centerline roll-up on the BoLT-2 geometry when utilizing a sustained, stochastic freestream forcing function as an input to the DNS. Therefore, this section seeks to investigate this effect on BoLT-2.

Using the methodology introduced, snapshots were taken at the same non-dimensional locations of the 25% scaled configuration as the full scale configuration. SPOD modes shapes of streamwise velocity perturbations are plotted in Figure 5.7 taken at $x/L_s = 0.025$ and 0.050. The spectrum containing the majority of the disturbance energy gain is around 5 kHz. Therefore, at both streamwise locations, Figure 5.7 shows a strong signature in the power spectral density (blue line) and modal energy spectrum of each SPOD mode (black lines) at 5 kHz where the SPOD mode shapes are also plotted. With SPOD, the data matrix is split into blocks and the windowed Fourier Transform is calculated and stored. This means there are a set of resolvent modes containing a portion of the modal energy at each discrete frequency depending on the window-length and sampling parameters. At $x/L_s = 0.050$, the leading SPOD mode with a frequency of 5 kHz contributes to 52% of the modal energy with a mean spanwise wavelength, λ_ζ, of 0.84 mm. The same modal contribution is contained in the streamwise direction at $z/L_s = 0.020$ with a mean streamwise wavelength, λ_ξ, of 5.3 mm. This is shown in Figure 5.8 along with high frequency modes having modal energy peaks at 65 kHz and 150 kHz. The 150 kHz mode has a relatively high PSD

signature with the first SPOD mode having a 53% modal energy contribution. The low frequency mechanisms are slowly varying in space and time and closely resemble the shape of stationary crossflow structures induced by roughness [70]. Whereas the high frequency mode of 150 kHz identified in the streamwise direction are consistent with expected wavelengths for high frequency travelling crossflow instability obtained with PSE [104] near the swept leading edge.

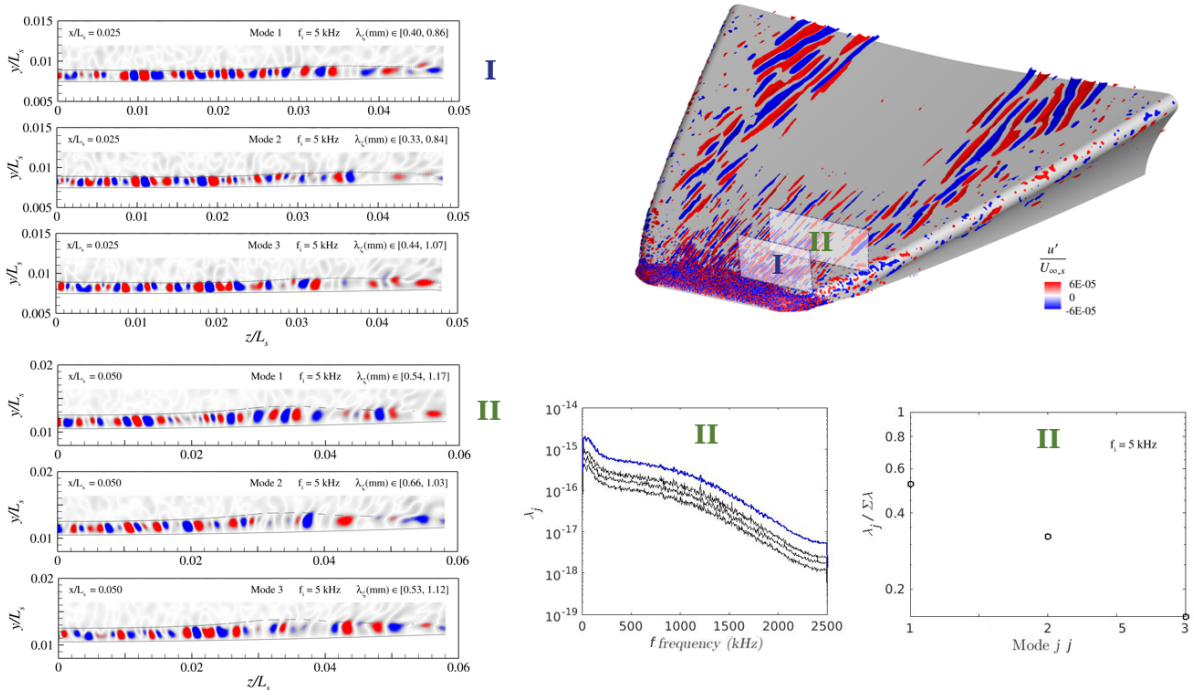

Figure 5.7: Leading SPOD Modes for dominant frequency of the subscale configuration at $x/L_s = 0.025$ and $x/L_s = 0.050$ and the spanwise wavelength defined as λ_ζ.

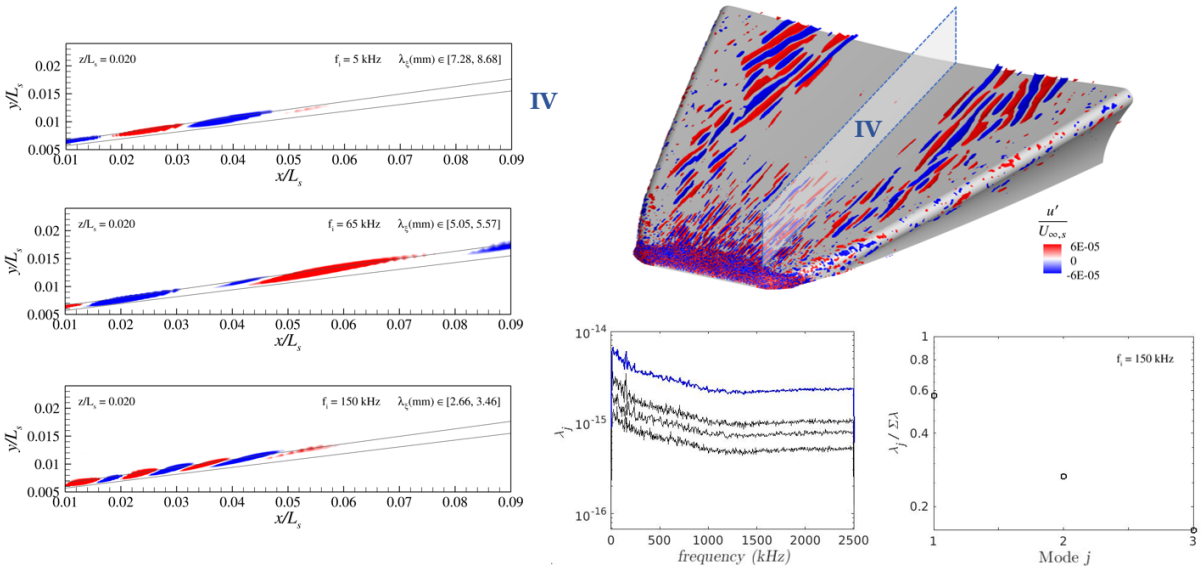

Figure 5.8: Leading SPOD Modes of the subscale configuration at $z/L_s = 0.02$ and the streamwise wavelength defined as λ_ξ.

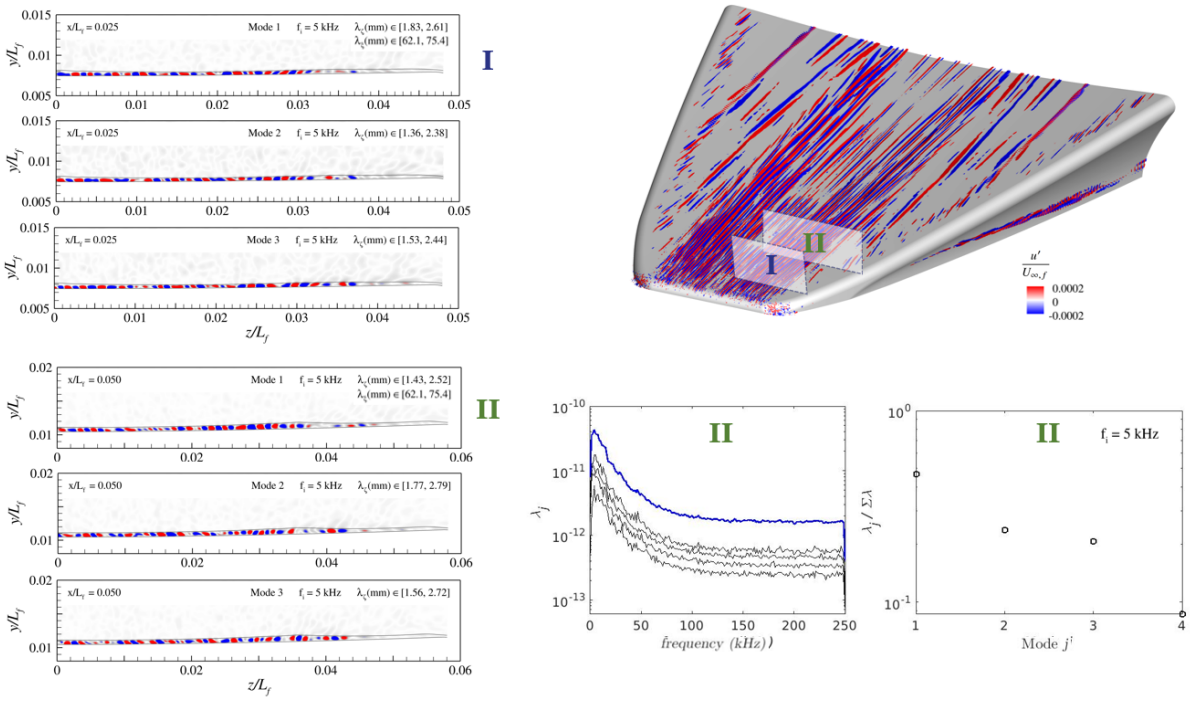

Figure 5.9: Leading SPOD Modes of the flight configuration at $x/L_f = 0.025$ and $x/L_f = 0.050$

The flight configuration has a similar modal energy spectrum as the subscale configuration since the majority of the modal energy is contained within the 4 kHz to 6 kHz frequency range. However, due to the thin boundary layer, the structures are contained within a shorter distance off the wall. The mean spanwise wavelength of the low-frequency structures range from 2.0 mm to 3.1 mm from $x/L_f = 0.025$ and 0.050, respectively. Whereas, the local spanwise wavelength scales with the local boundary layer thickness near the centerline by $\lambda_\zeta/\delta \sim 4$ for the flight configuration compared to $\lambda_\zeta/\delta \sim 2$ for the subscale configuration.

The amplification of disturbances by the low-frequency structures of the flight configuration is much greater than that of the subscale configuration. This suggests that the streamwise structures could potentially contribute to early transition at higher Reynolds numbers and can be influenced by the freestream environment or other external perturbation sources (i.e. roughness or surface protuberance). Therefore, surface roughness was briefly investigated by utilizing a probability density function to generate distributed roughness. Each wall node was perturbed using a random number, between (-1,1), and multiplied by a maximum amplitude. The displacement was smoothed along grid connected lines, similar to the approach used by Dinzl and Candler [26]. Previous work by Thome et al. [70] showed that different heating patterns are observed on the BoLT configuration using different roughness wavenumber distributions. However, a non-biased wavenumber distribution allows for an exploratory look at the flowfield response without filtering out potentially relevant disturbances. In this work, it was found that similar structures containing zero frequency temporal wavenumbers were excited using a maximum node displacement of 2 μm with a Gaussian distribution probability density function. The same streamwise structures were observed near the leading edge which contained zero temporal frequencies. This suggests steady forcing induced by roughness can seed non-modal growth instabilities near the nose tip of BoLT-2. At the current condition, the perturbation values are

small suggesting it is unlikely to trip early transition at the flow conditions simulated.

5.3.2 Modal Growth Mechanisms

Due to the receptivity mechanisms, modal growth of instabilities becomes present further downstream. When considering the subscale configuration, the local disturbance amplitudes induced by the low-frequency structures start to decay near the centerline when travelling downstream. While crossflow instabilities begin to show strong signatures in the frequency spectrum ranging from 20 kHz to 40 kHz. Additionally, there is a presence of signatures lower than 20 kHz within the centerline roll-up ($x/L_s \, \epsilon \, [0, 0.04]$). However, the local disturbance energy is much higher closer to the swept leading edge between $x/L_s \, \epsilon \, [0.04, 0.1]$. It is in this region where SPOD mode shapes representative of travelling crossflow instabilities are prominent for the subscale configuration.

Contrary to the subscale configuration, the flight configuration shows strong signatures in the modal energy spectrum of the low-frequency modes and are contained within the centerline roll-up at approximately 20 kHz. Also, the spectrum shows strong signatures at 820 kHz, 1000 kHz, and 1660 kHz, and the resolvent modes of the respective frequencies are primarily located closer the the swept leading edge. The streamwise SPOD mode shape for the 820 kHz mode was shown previously and represents a second Mack mode instability. The modal energy contribution is 99.8% for the first SPOD mode based on the spanwise collected dataset. Furthermore, the PSD peak is the highest at 820 kHz suggesting second-mode amplification is more profound for the flight configuration. The SPOD mode at 1000 kHz appears to represent second-mode disturbance amplification with a spanwise wavelength. Whereas, the 1660 kHz mode appears to be a secondary harmonic of the primary 820 kHz disturbance. At $x/L_f = 0.25$,$z/L_f = 0.0755$, the 820 kHz second-mode disturbance has a wavelength of $\lambda_\xi = 1.56$ mm which is approximately twice the boundary layer

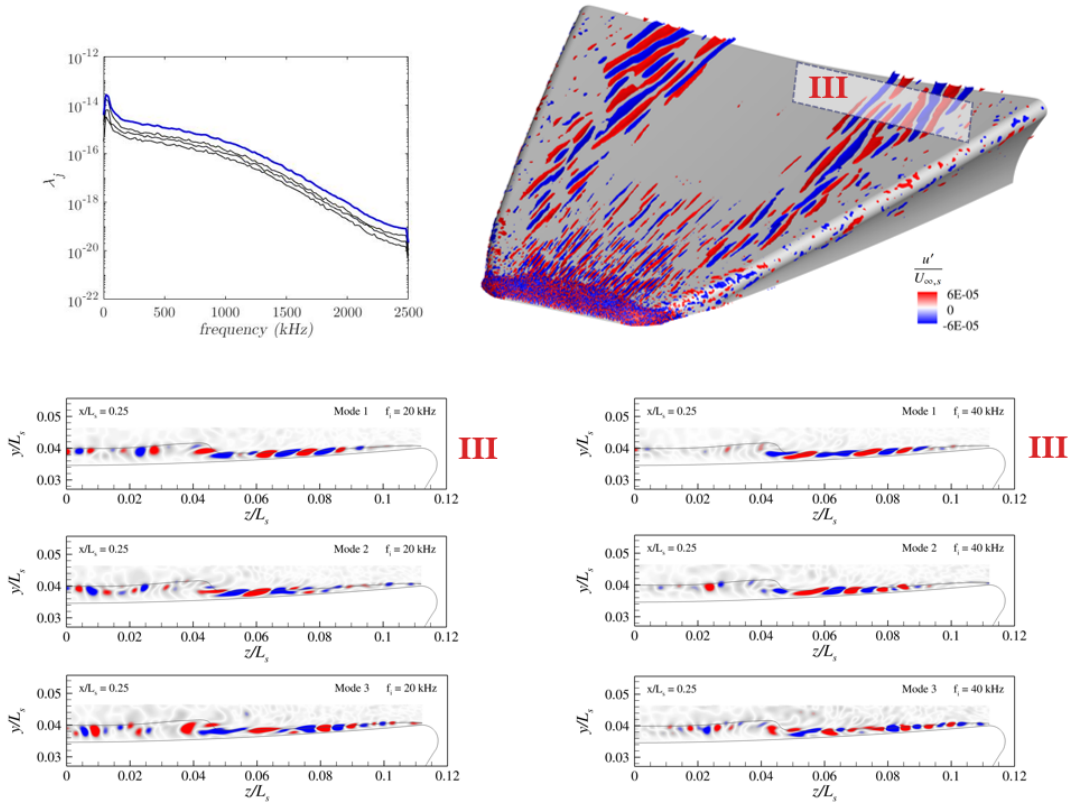

Figure 5.10: Leading SPOD Modes of the subscale configuration at $x/L_s = 0.25$

thickness resulting in a phase speed of $c_{ph} = 1275$ m/s. The frequency scales with the local boundary layer properties as $f \sim 0.4\frac{u_e}{\delta}$ for the flight configuration.

The local scaling for second-mode frequencies based on Stetson [110] hypothesizes that second-mode frequencies scale with the boundary layer edge velocity and the local boundary layer thickness as $f \approx 0.4\frac{u_e}{\delta}$. This was first shown to be consistent for frequencies calculated on BoLT by Knutson et al. [11]. Therefore, using the local edge velocity in this case of 1502.8 m/s and local boundary layer thickness of 0.739 mm estimates that the local frequency for second-mode would be approximately 814 kHz for this case. This frequency corresponding to second-mode instability scale with the local flow properties on BoLT-2 similar to the second-mode frequency estimate for hypersonic boundary layers introduced by Stetson and is consistent with Knutson

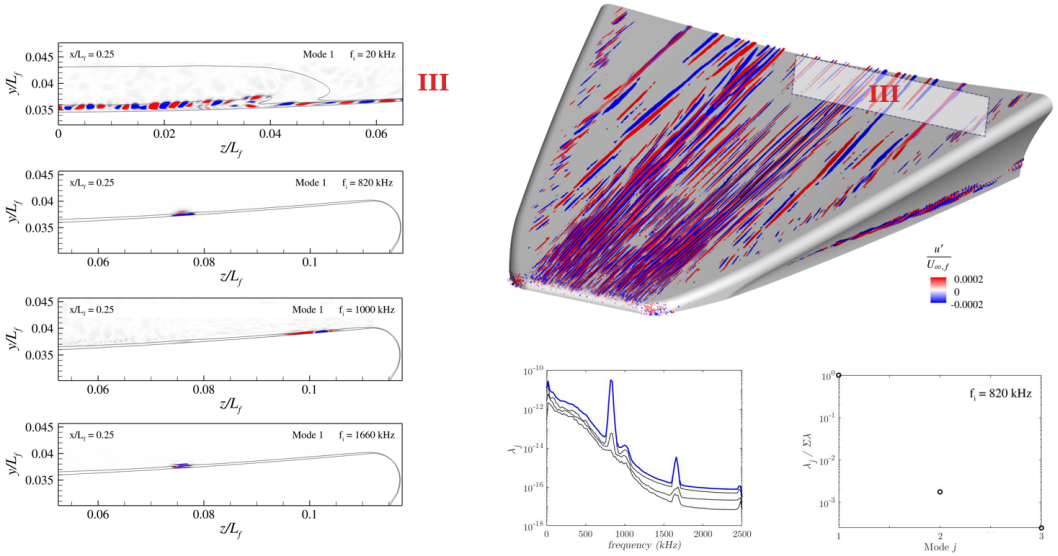

Figure 5.11: Leading SPOD Modes of the flight configuration at $x/L_f = 0.25$

et al. [11].

5.3.3 Unstable Transition Mechanisms

As mentioned previously, the grid spacing near the end of the domain is larger than what is required to properly resolve the turbulent length scales. However, the grid and numerical method is still able to resolve relevant instabilities within the boundary layer. Most noticeable are instabilities found within the strong shears layers of the vortical structures near the centerline, and distinct structures associated with multiple types of instabilities between the centerline and swept leading edge. This is visualized in Figure 5.12 with a single isosurface plotted of Q-criterion and colored by streamwise velocity on the left. An instantaneous surface pressure perturbation distribution relative to the time-averaged wall value is plotted on a grey scale on the right. The largest magnitude in pressure perturbations is located near the centerline at which downstream of $x/L_f \approx 0.75$ the centerline vortical structures become unsteady. The sampling duration is $T_f u_\tau/\delta_i > 18$ and sampling frequency is $T_s u_\tau/\delta_i < 0.025$; where

T_f is the time accumulated to collect statistics, T_s is the time between snapshots, δ_i is the maximum boundary layer thickness, and u_τ is the local friction velocity at δ_i. In this work, the introduced sampling parameters is adequate for extracting meaningful SPOD modes.

In the following sections, SPOD modes are extracted from flow state perturbations relative to the time-averaged values to identify the relevant modes contributing to transition. Therefore, current downstream analysis is meant to act as a starting point to shed light on the types of instabilities contributing to transition at a flight condition near regions of highest disturbance amplification using the introduced numerical methodology.

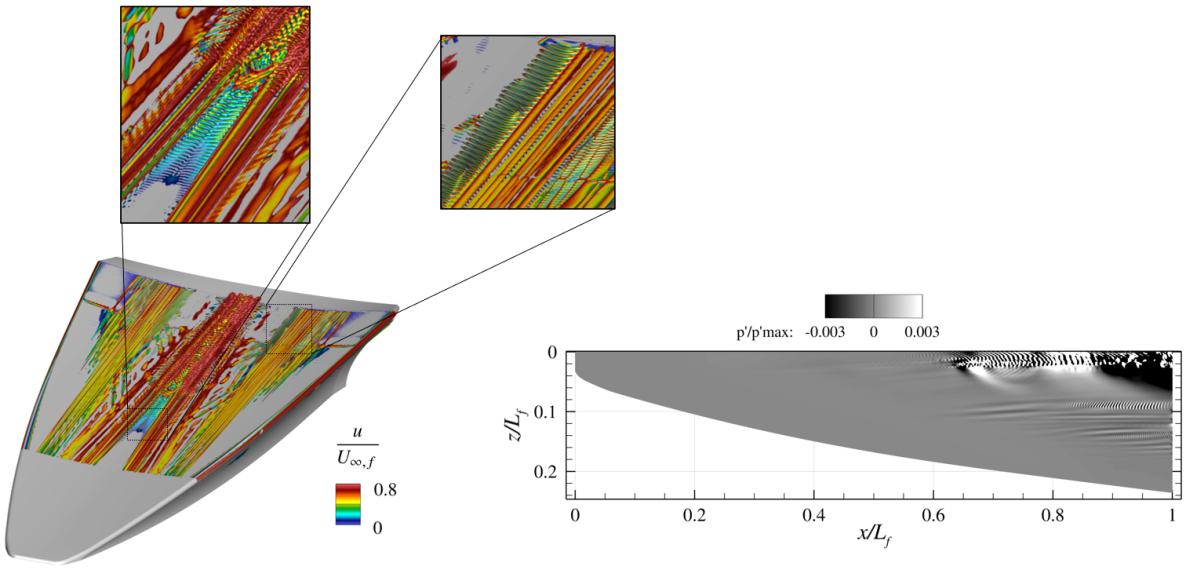

Figure 5.12: Q-criterion isosurface colored by normalized streamwise velocity (left). Instantaneous wall pressure fluctuations are normalized by the maximum pressure fluctuation on the wall (right).

Mixed Mode Region

The so called "mixed-mode" region in this work refers to the region away from the large-scale vortical structures and swept leading edge. The region contains distinct

structures corresponding to both highly amplified acoustic waves and crossflow instabilities. Five separate slice datasets were collected at $x/L_f = 0.77$, 0.88, 0.93 and $z/L_f = 0.089$, 0.135 then truncated within $x/L_f \in [0.77, 0.93]$ and $z/L_f \in [0.08, 0.16]$ to isolate the region. If the centerline region is included for the analysis, peaks in the modal energy spectrum associated with dominant instabilities is more challenging to identify since the overall modal energy across the entire frequency spectrum is increased. This is attributed to breakdown occurring near the centerline downstream as will be shown in the following section. SPOD is then performed on all slices to capture how the dominant modes are correlated in space and time. Figure 5.13 shows peaks in the modal energy spectrum in the low frequency range between 11 kHz to 46 kHz and high frequency range between 295 kHz to 310 kHz.

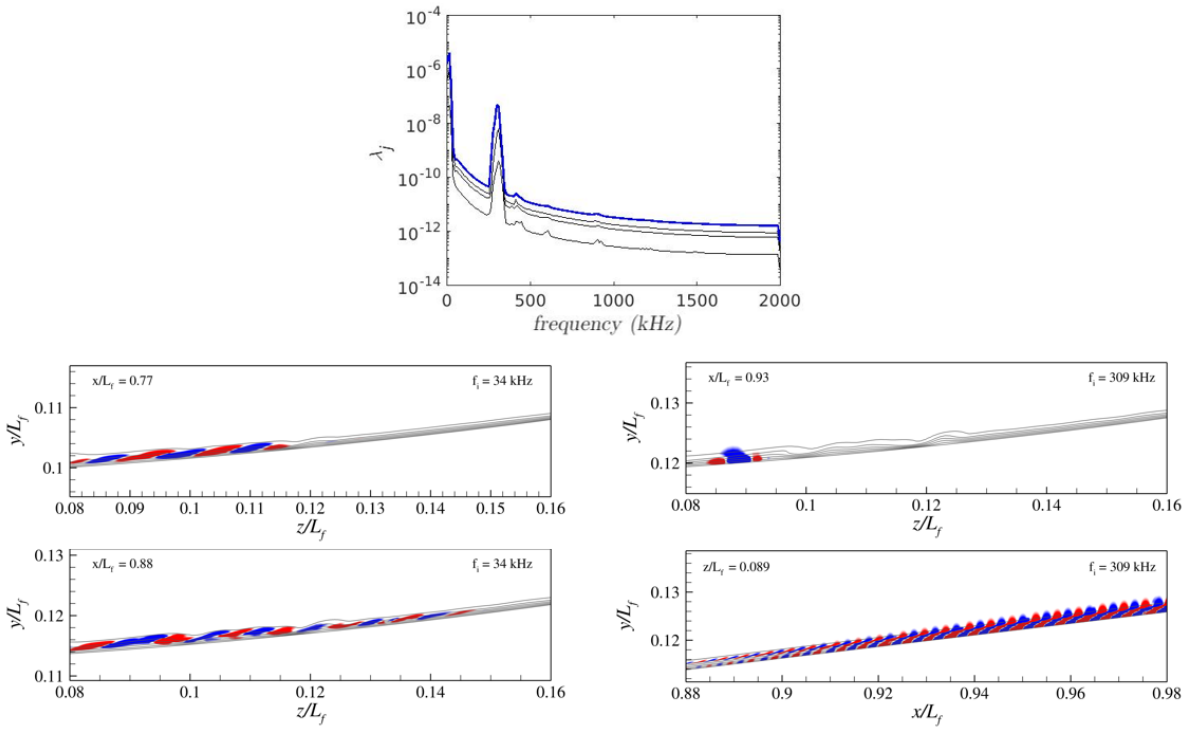

Figure 5.13: Dominant SPOD modes of the flight configuration between $x/L_f \in [0.77, 0.93]$ and $z/L_f \in [0.08, 0.16]$. Contour lines correspond to the time-averaged streamwise velocity of the dataset.

The value of 11 kHz in the modal energy spectrum is a peak at the sampling duration cutoff. This mode is deemed to be insignificant since the mode shape contains very low signatures and is located away from where transition occurs. This was determined by comparing the location of the mode shape with respect to regions containing the highest modal energy which is not shown. For this section, the low frequency peak values primarily range between 23 kHz and 46 kHz which is a typical range for travelling crossflow frequencies on this geometry. This is because travelling crossflow has a strong presence across the entire vehicle surface and so appears to have a larger modal energy peak. Figure 5.13 shows a travelling crossflow SPOD mode of 34 kHz on the left and is similar to DMD mode shapes of travelling crossflow [11, 111]. This mode is primarily located in the region of highest local disturbance energy of the mixed-mode region even though the surface pressure perturbations have lower perturbations relative to a highly localized region at $z/L_f = 0.089$. The highly localized exponential growth in surface pressure perturbations corresponds to the high frequency SPOD mode of 309 kHz. This mode has similar features of second Mack mode instability and scales as $f\frac{\delta}{u_e} \approx 0.35$ (at $x/L_f = 0.93$ and $z/L_f = 0.089$) using the streamwise wavelength of $\lambda_\zeta = 4.38$ mm. The mode shape is used to calculate the spanwise wavelength of $\lambda_\xi = 6.72$ mm where the wave angle is 32.7. The mode shapes suggests there is a modal interaction since the disturbances amplified by second Mack mode instabilities in the region are oblique and coexist with a strong crossflow presence. This suggests second Mack mode instabilities have significant amplification for BoLT-2 at higher Reynolds numbers. Whereas at relatively lower Reynolds number conditions, the flow state tends to favor the amplification of crossflow instabilities.

Vortical Mode Region

The vortical mode region in this work is referred to as the region containing the centerline roll-up illustrated by the bottom, left plot of Figure5.4. The vortical structures

have been shown to support vortical instabilities in the past for the subscale BoLT geometry [11] and is therefore named for consistency. Similar to the previous section, five separate slice datasets were collected but now at $x/L_f = 0.55, 0.66, 0.77$ and $z/L_f = 0.012, 0.0235$ then truncated within $x/L_f \in [0.55, 0.77]$ and $z/L_f \in [0, 0.06]$. For brevity, modes shown contain the highest energy gain and are located in the region where the largest flow perturbations are present. This is the most unstable

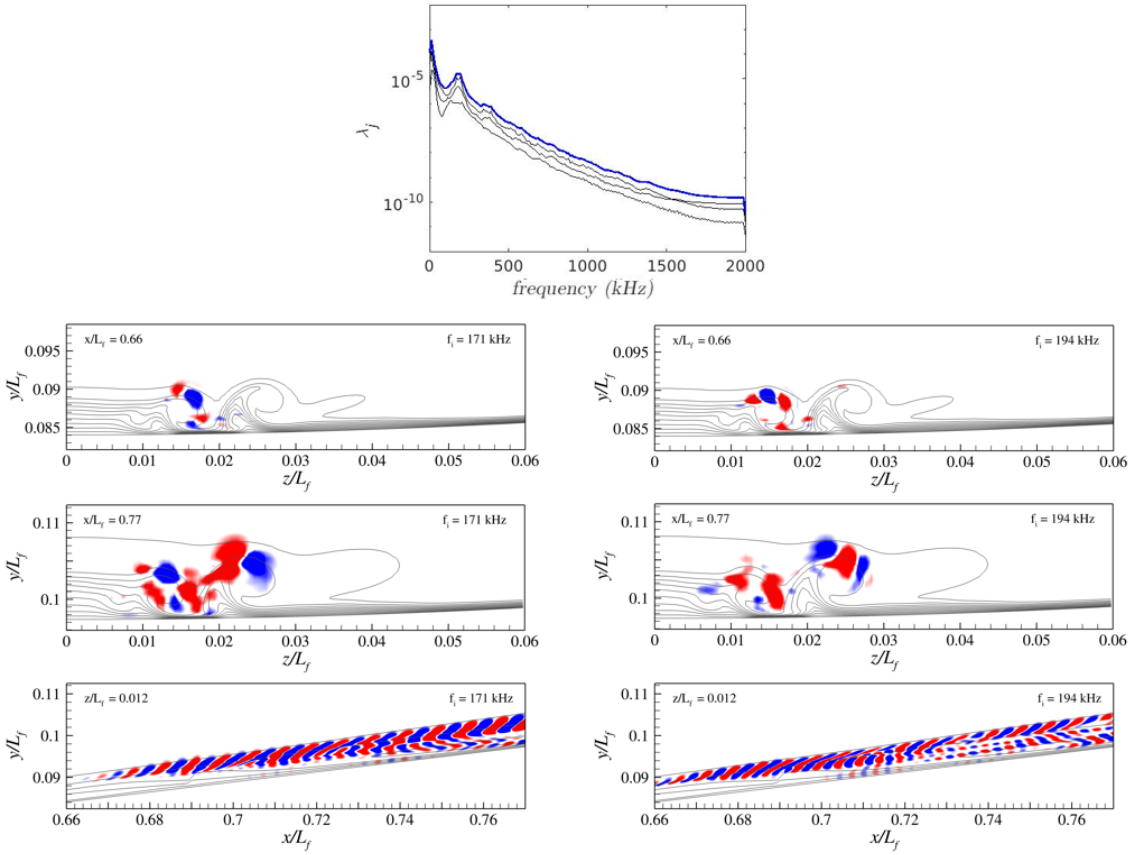

Figure 5.14: Dominant SPOD modes of the flight configuration between $x/L_f \in [0.55, 0.77]$ and $z/L_f \in [0, 0.06]$. Contour lines correspond to the time-averaged streamwise velocity of the dataset.

region within the boundary layer where breakdown to turbulence is initiated with the current numerical forcing approach. The centerline region is primarily dominated by high frequency vortical modes between 170 kHz and 200 kHz originating on the top

portion of the primary vortex structure closest to the centerline. Significant exponential disturbance growth is observed at which the vortical structures become unsteady and eventually the structures breakdown further downstream. Upstream of breakdown, a 171 kHz mode is located on the right side portion of the vortical structure closest to the centerline. Whereas, a 194 kHz is on the top portion of the same vortical structure. The SPOD mode shapes are similar to the DMD mode shapes associated with secondary flow behavior of developing vortex structures of the subscale BoLT-2 geometry [111]. The vortical instabilities investigated for both cases are similar to the excitation of secondary instability mechanisms of crossflow vortices of a swept wing [28]. For the flight condition, breakdown within the centerline vortical structures begins to augments surface heating. This is illustrated in Figure5.15 where a comparison between 5.15a) and 5.15b) reveals an increase in surface heating. Most notably when comparing the peak values as seen downstream denoted by the black line at x = 0.947 m and spanwise locations of 0.012 m and 0.128 m. This suggests the start of nonlinear onset originating from the dominant instability modes obtained with the current initial amplitude spectrum used for forcing.

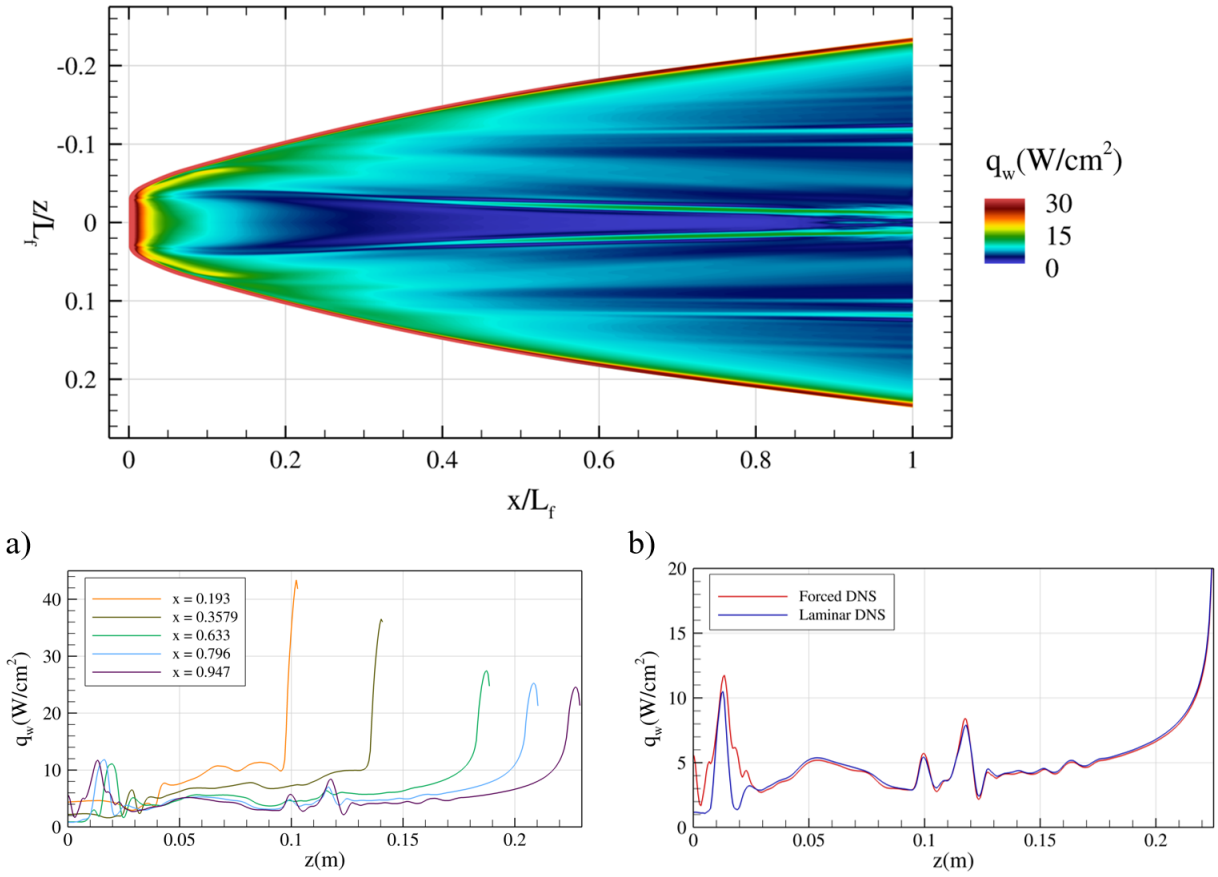

Figure 5.15: Time-averaged surface heat flux sampled for a one-half convective flow through time along with a) line extractions at various streamwise locations plotted for the time-avg solution and b) line extraction comparison of the time-averaged solution of the forced DNS case plotted against the laminar solution at x/L = 0.947.

5.4 Potential Disturbance Source in Flight: Particulate-Induced Transition

One challenging aspect that remains to be an open research question is what causes transition in flight? Previously, it was introduced in Chapter 3 that potential sources of environmental disturbances include distributed surface roughness, freestream turbulence, and particulates in the atmosphere. It is unclear if it is solely one source or

the coexistence of all these sources that have some degree of contribution to transition in flight. Thome et al. [70] showed that various surface roughness distributions and variable wall temperatures can excite boundary layer instabilities in different ways relative to the smooth model solution on BoLT. Furthermore, it was demonstrated earlier in this chapter that stochastic freestream disturbances that are meant to mimic the effects of freestream turbulence can cause transition on BoLT-2. This leads to the next logical questions which is whether or not particulates in the atmostphere exist, and if so can they produce disturbances that cause transition? To help answer the first part of this question, ballooning campaigns were conducted during the week of the BoLT-2 flight experiment to quantify atmospheric particulate size distribution prior to and after the flight test. This is illustrated in Figure 5.16 showing particle sizes and number densities obtained from optical-particle-counters the day of and after the BoLT-2 flight test. Interestingly, the particle size distributions vary significantly from day to day and whether the data was collected on the ascent or descent. This implies that the trajectory that a vehicle is actually flown may have significantly different particle sizes and number densities.

In order to help answer the question whether it is possible for particulates to initiate transition on BoLT-2 in simulation, a case is performed at a single freestream condition and for a single particle size distribution. This is chosen to be at on the conservative flow condition such that the Reynolds number is relatively low so that the boundary layer state is physically more stable and number densities of particulates are low. This is meant to simplify the parameter space to investigate if the disturbances produced by particulates are amplified by instabilities on BoLT-2 when transition onset begins in flight and not necessarily where transitional or turbulent heating transfer rates were measured. Based on the data, a simulation was chosen to be conducted at conditions corresponding to an altitude of approximately 29.3 km during the descent of the trajectory at 398.75 seconds. The simulation conditions are

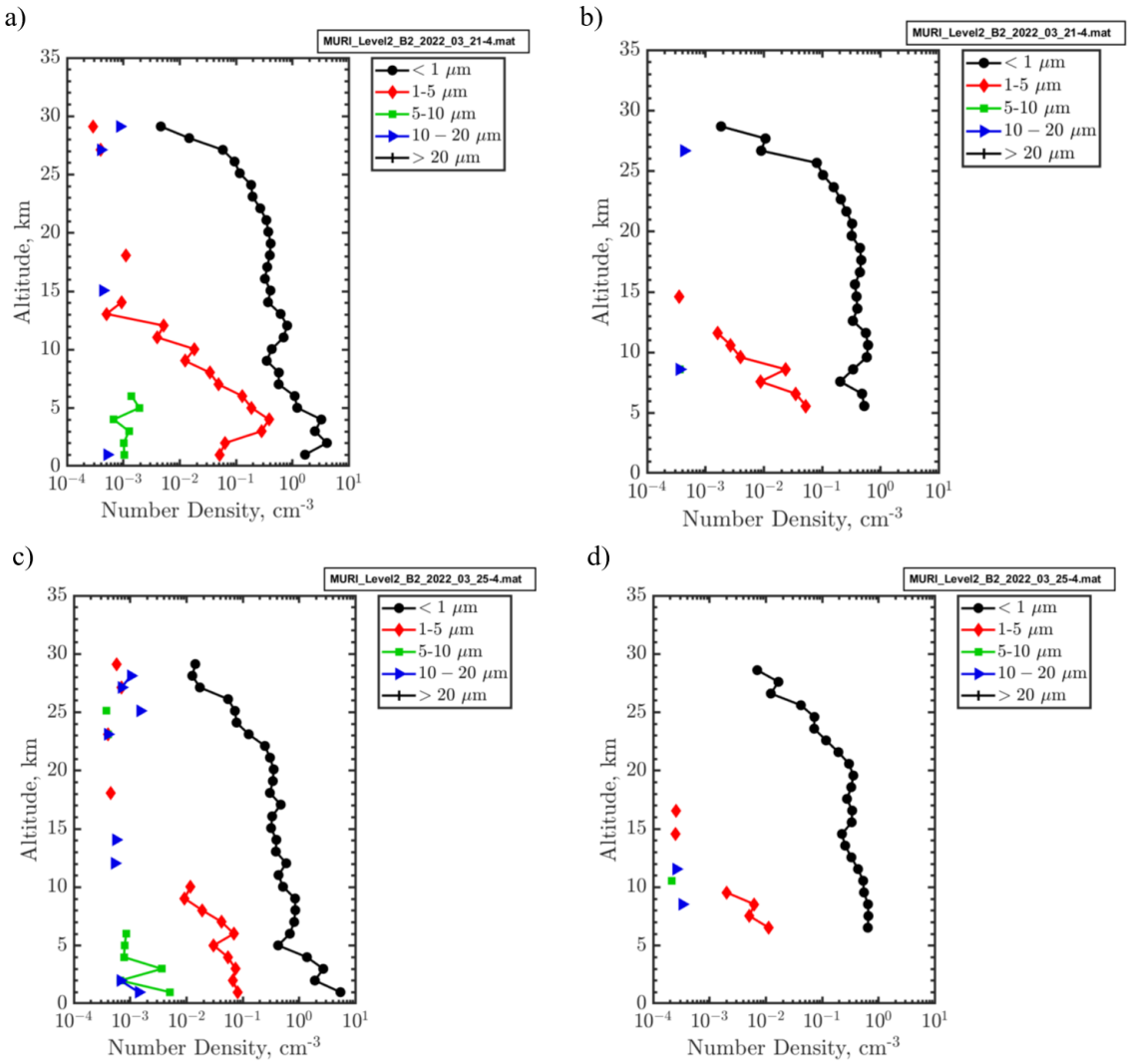

Figure 5.16: Particle size distributions constructed from atmospheric particulate measurements obtained from optical-particle-counters. a) ascent on 3-21-2022, b) descent on 3-21-2022, c) ascent on 3-25-2022, and d) descent on 3-25-2022. (Private Communication: Joseph Habeck, UMN).

summarized in the Table 5.8 and an isothermal wall is assumed to have a temperature of 330 K.

Particulates are introduced into the flowfield with a US3D plugin developed by Anthony Knutson at the University of Minnesota. The plugin utilizes Lagrangian

M_∞	U_∞ (m/s)	ρ_∞ (kg/m^3)	T_∞ (K)	T_{wall} (K)	Re/m (m^{-1})
5.93	1751.5	0.0204	216.95	330	2.51×10^6

Table 5.8: Flight Condition

particle tracking to propagate particulates through the domain while storing particle trajectories in memory. Particulates are assumed to be sulfuric acid (H_2SO_4) droplets and are introduced using a sampling size bin that is specified by the user. Based on the conditions from Table Table 5.8 and the particle data from Figure 5.16, particles imposed are sampled from a single size bin corresponding to the data where sizes range from 10 to 20 micrometers. Note that these are the largest particles which were measured close to 29 km from Figure 5.16. The number density of the size bin is set to 1000 particles per cubic meter (10^{-3} cm^{-3}). Note that measurements contain multiple particle sizes and number densities meaning that many small particles may exist in flight. However, for simplicity, the actual particle diameter of the simulations is set to range between 10 and 20 micrometers which is consistent with the largest particle size measurements. The drag model introduced by Henderson [112] is assumed along with the an inelastic wall collision model.

The simulation was run for three convective flow through times using a time step of 25 nanoseconds to ensure that the particle CFL number remained below 1. Where one convective flow through time is defined as a single particle, at a constant velocity equal to the freestream velocity, were to travel the length of the computational domain. The numerical method used is the exact same as what was used previously in this chapter for the freestream stochastic forcing case. In this case, the particles produce shocklets after propagating through the bow shock. Post-shock, the particles generate a spectrum of acoustic waves which then enter the boundary layer even if the particles do not impinge on the surface. Figure 5.18 shows surface pressure perturbations relative to the initial solution after consecutive flow through times starting from

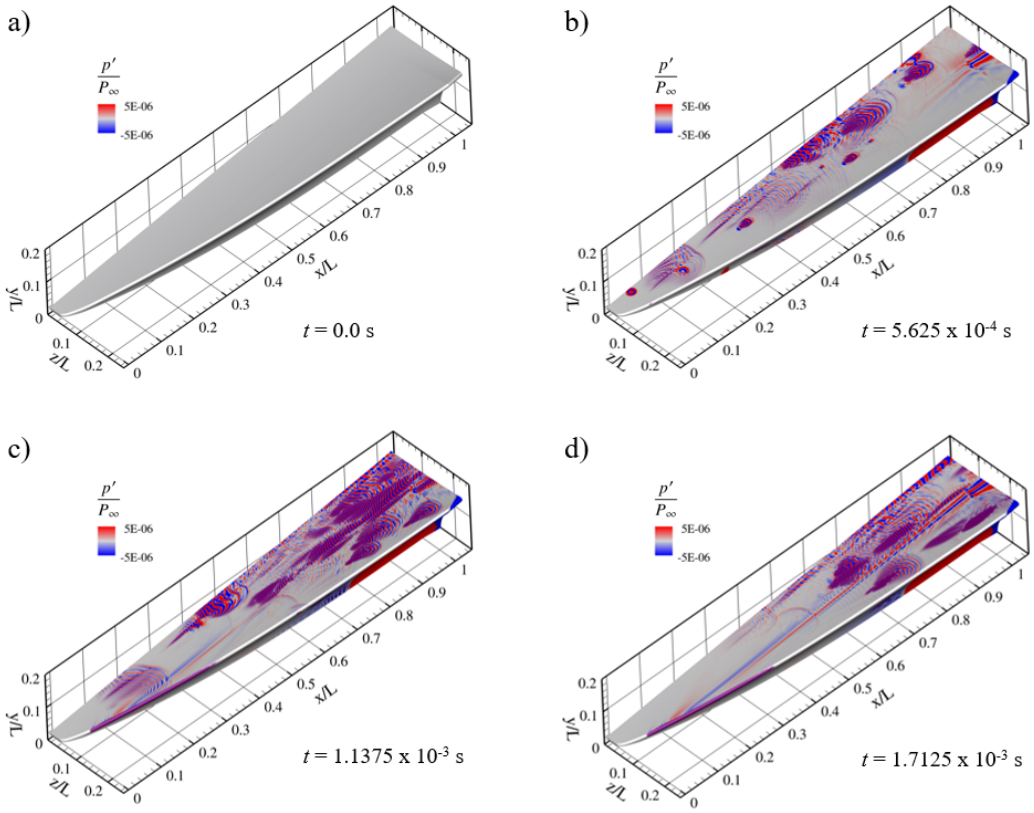

Figure 5.17: Surface pressure perturbations of instantaneous pressure with the laminar baseflow pressure value subtracted from the solution and normalized by the freestream pressure.

the initial solution state. This reveals that the particles generate wavepacket-like perturbations which propagate in all relative directions. The high-frequency waves appear to excite second-mode, crossflow, and vortical instabilities where the largest perturbations are present in the mixed-mode region which is consistent with Knutson et al. [11] which is a case that produces a very similar boundary layer state comparable to this flight condition due to scaling and geometry. Notice that high frequency oscillations develop at the swept leading edge upstream as seen in Figure 5.18c) and are thought to be numerically generated. Another case was performed where the oscillations were present, but it was found that the oscillation did not have a

significant contribution to excitation of instabilities downstream. It is unclear why this occurs but future work should aim to address this. For this case, a particle is in close contact with the swept leading edge at which transition is sustained through excitation of stationary crossflow instability taking the form of streamwise streaks on the surface occurring after a time of 5.625×10^{-4} s and before a time of 1.1375×10^{-3} s. Later downstream, transition is sustained such that particles are continuously introduced into the domain at which small amplitude perturbations excite second-mode, crossflow, and vortical instabilities.

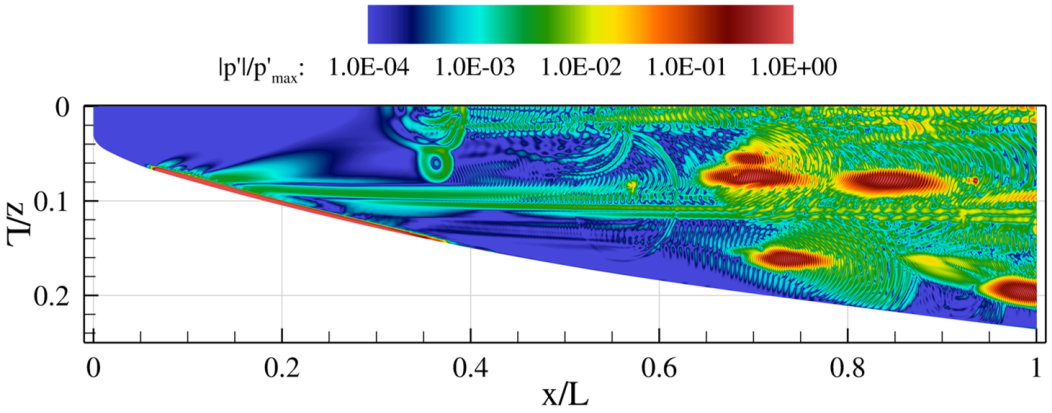

Figure 5.18: Surface pressure perturbations of instantaneous value relative to the laminar baseflow pressure value and normalized by the maximum pressure perturbation on the wall. The quantities are plotted on a log-scale at $t = 1.7125 \times 10^{-3}$ seconds.

Figure 5.18 reveals the relative amplification of the waves generated by the particles and reach over 4 orders of magnitude located where particles pass through the most physically unstable regions. This plot is of the instantaneous solution and has the same interpretation as the relative disturbance amplification of Figure 3.2. The maximum wall pressure perturbation value here is about 0.03% relative to the baseflow wall value. Experience has found that breakdown typically produces a significant increase in surface wall heating when surface pressure perturbations reach over 1% relative to the baseflow value on BoLT-2 depending on the flow conditions

and location.

The excitation of the various instabilities of the BoLT-2 flowfield suggests that particulate-induced transition is present in simulations and data suggests that it is possible in flight. Again, the simulations assumed a single particle size that is higher than what was measured based on the instrumentation. It is unclear how much of an effect imposing more particle sizes to the simulation and how much the transition process is affected. Future work should aim to address this where this case is only meant to shed light on the matter and how it may have a significant impact at higher Reynolds numbers under hypersonic flight conditions.

5.5 Chapter Summary: Flight Conditions

Boundary layer instabilities associated with distinct transition mechanisms of the BoLT-2 flowfield were identified using SPOD and ranked by their modal energy signatures. This was intended to quantify how the disturbances of the receptivity process may contribute to the later stages of the transition process at flight conditions where the boundary layer is likely to be in a transitional state. This was achieved by performing high-fidelity computations of the Navier-Stokes equations using a low-dissipation numerical method within US3D. Furthermore, we introduced disturbances using a stochastic forcing function at the freestream to allow for a boundary layer response revealing modal and non-modal growth mechanisms that exist within the BoLT-2 flowfield. The most notable SPOD modes near the nose tip are associated with low frequency, non-modal growth mechanisms contained within the centerline rollup of the boundary layer for both the subscale and flight configurations. The perturbations were found to be much larger for the full-scale configuration at flight conditions, suggesting the non-modal growth mechanisms could potentially contribute to early transition at high Reynolds numbers.

Modal growth mechanisms were identified slightly further downstream of the nose tip. The subscale configuration contained leading SPOD modes associated with travelling crossflow instability, while the flight configuration had dominant SPOD modes corresponding to Mack's second mode instability. This suggests second-mode disturbances are increasingly susceptible to amplification on the BoLT-2 geometry with higher Reynolds numbers at hypersonic conditions. Additionally, leading modes contributing to transition downstream within the centerline vortical structures and mixed-mode region were identified. It was found that high-frequency disturbances in the range between 170 kHz and 200 kHz initiate breakdown near the centerline and are primarily localized near shear layers of streamwise vortex stuctures. While breakdown was not observed in the mixed-mode region using the current methodology, we were still able to identify crossflow and second-mode instabilities that contribute to a large increase in local disturbance energy.

Chapter 6

Summary & Conclusion

6.1 Summary

This thesis introduced a general framework to be used for performing direct numerical simulations with a focus on simulating and analyzing boundary layer instabilities contributing to breakdown to turbulence. The work aimed to characterize, understand, and potentially predict how transition to turbulence could occur on BoLT-2. Using a state-of-the-art compressible gas unstructured CFD code called US3D, the underlying flow physics relevant to boundary layer instabilities were replicated by the numerical code with a comparison to linear stability theory by demonstrating the accuracy of the numerical methodology for amplification of disturbances by high frequency boundary layer instabilities of a cone. The importance of high-order, low dissipation numerical methods was discussed and demonstrated along with the significance of accurate shock capturing and intuitive control of numerical dissipation related to performing accurate, high fidelity computations. After establishing this, forcing functions were investigated and obtained a numerical response representative of the natural transition process inherent to the physically unstable modes characteristic to the boundary layer state of BoLT-2. While the study of receptivity and defining freestream forcing environments is subject to debate, the results demonstrate

that a response representative of the flow state is realized while quantifying a noise level to help account for the initial amplitude spectrum meant to mimic the effects of stochastic acoustic, entropic, and vortical waves. A similar methodology was also applied to a flight condition which has shown agreement with experimental measurements. The modal analysis was applied to forced DNS datasets to quantify potentially relevant modes contributing to breakdown to turbulence at various flow conditions in order to characterize the nonlinear stages of transition on BoLT-2. The forced DNS framework demonstrates that even without making any *a priori* assumptions on the perturbation form, the dominant mechanisms within the later stages of transition processes in high-speed compressible boundary layer flows are identified.

6.2 Conclusion

The work in this thesis contributes to the understanding and importance of high-order, low-dissipation numerical methods for simulating unsteady, three-dimensional hypersonic flows containing boundary layer instabilities and transition to turbulence. For high-order spatial accuracy, a well designed shock sensor is essential for obtaining accurate boundary layer breakdown calculations. Accurately simulating the amplification of initially low-amplitude disturbances requires a numerical method that can obtain a solution with a numerical noise level that is significantly lower than the amplitude of the physical disturbances. On the contrary, the numerical stability has to be maintained such that the level of numerical dissipation does not overwhelm the attenuation of physical instabilities and numerically dampen disturbances introduced into the flowfield. The test cases of this thesis supports this and were used to prove the performance of a compression-based shock sensor and the capability of controlling numerical dissipation for high-order spatial accuracy was demonstrated. Furthermore, it was demonstrated that first-order time integration damps out prop-

agating disturbance amplitudes and high frequency instabilities. The purpose of this was to show the necessity of a high-order time integration method to reduce the numerical dissipation associated with temporal damping when advancing in time with implicit schemes. Higher-order time accuracy was achieved by applying a Newton's method allowing for accurate simulation of disturbance amplification of instabilities.

The results in Chapters 4 investigated the nonlinear evolution of the transition process on BoLT-2 at subscale wind tunnel conditions by simulating the entire transition process. Modal analysis tools were used to extract dominant modes associated with second Mack mode, crossflow, and vortical instabilities. This provides new insight into how dominant instabilities contributes to the relevant growth and decay of perturbations into the flowfield with excellent agreement with experimental measurements. Breakdown was successfully simulated and caused by strongly nonlinear interactions between secondary instabilities of crossflow originating within developing vortical structures. This proves the need for numerical methods and a computational framework that accounts for the effects of perturbation amplification and how it relates to the baseflow state. The numerical methodology was verified by simulating transition to turbulence to ensure that the code and analysis faithfully reproduced relevant flow structures contributing to higher heat transfer rates. In order to understand how the methodology translates to flight, the results of Chapter 5 reveal how the boundary layer flow state is altered by viscous effects. Additionally, a flight condition representing transition in flight was investigated. This was meant to demonstrate the predictive capabilities and how a different transition scenario is likely present in flight. Breakdown was observed within the centerline vortical structures due to instabilities within the secondary roll-up at a much higher Reynolds number condition. This implies that transition on BoLT-2 in flight occurs at much higher Reynolds numbers than what is observed in ground test facilities.

The current work provides insight of transition to turbulence within the BoLT-2

flowfield and instabilities that may be present in flight. However, future work regarding disturbances sources should be investigated for improved prediction of transition in flight. The work in this thesis primarily focused on the nonlinear stages of transition and more attention is required towards the receptivity mechanisms resulting from initial perturbations that may influence the entire transition process. Freestream turbulence and particulate-induced transition have both been shown to be potential sources of transition in flight and would represent a more realistic disturbance environment. Nevertheless, the current approach is able to investigate the stability of unsteady, three-dimensional flow structures and identify potentially relevant instability mechanisms contributing to transition in flight. It was demonstrated that particle-induced transition is possible in simulations and a potential disturbance source in flight. Future efforts related to quantifying atmospheric flight environments could help to improve the understanding of transition in flight. Furthermore, both roughness [70] and variable wall temperature [71] can have a significant impact on the boundary layer state and future work should extend the parameter space for improved transition prediction. Furthermore, real-gas effects related to thermochemical nonequilibrium and gas-surface interactions are also known to alter disturbance amplification leading to turbulent boundary layers. Therefore, future work should aim towards investigating how thermochemical nonequilibrium effects have on the development of turbulent flow structures since the structures can augment surface heating of hypersonic flight vehicles at extreme conditions.

References

[1] Anderson, J. D., "Hypersonic and High Temperature Gas Dynamics," *AIAA Education Series*, Third Edition, 2006.

[2] Curran, E. T., and Murthy, S. N. B., "Scramjet Propulsion," *Progress in Aeronautics and Astronautics*, Vol. 189, Second Edition, AIAA, 2001.

[3] Niu, Q., Yuan, Z., Chen, B., and Dong, S., "Infrared radiation characteristics of a hypersonic vehicle under time-varying angles of attack," *Chinese Journal of Aeronautics*, Vol. 32, No. 4, 2019, pp. 861, 874. doi:10.1016/j.cja.2019.01.003.

[4] Longo, J. M. A., Hannemann, K., and Hannemann, V., "The Challenge of Modeling High Speed Flows," *Chinese Journal of Aeronautics*, Vol. 32, No. 4, 2007.

[5] Gao, F., and Chen, F. L., "Numerical Study on Internal Flow Field Dynamics Performance of Scramjet," *MATEC Web Conf.*, Vol. 288, 2019.

[6] Anderson, B. P., Campbell, C. H., Saucedo, L. A., Kinder, G. R., and Berger, K. T., "Boundary Layer Transition Flight Experiment Overview and In-Situ Measurements," *48th AIAA Aerospace Sciences Meeting*, AIAA 2010-0420, 2010.

[7] Candler, G. V., and Campbell, C. H., "Hypersonic Navier-Stokes Comparisons to Orbiter Flight Data," *48th AIAA Aerospace Sciences Meeting*, AIAA 2010-0455, 2010.

[8] Reda, D. C., "Boundary-Layer Transition Experiments on Sharp, Slender Cones in Supersonic Free Flight," *AIAA Journal*, Vol. 17, No. 8, 1979, pp. 803, 810.

[9] Wheaton, B. M., Butler, C. S., McKiernan, G. R., and Berridge, D. C., "Initial Results from the BOLT Flight Experiment," *AIAA Paper 2022-0345*, 2022.

[10] Thome, J., Dwivedi, D., Anubhav, Nichols, J. W., and Candler, G. V., "Direct numerical simulation of BoLT hypersonic flight vehicle," *2018 Fluid Dynamics Conference*, 2018, p. 2894.

[11] Knutson, A. L., Thome, J. S., and Candler, G. V., "Numerical Simulation of Instabilities in the Boundary-Layer Transition Experiment Flowfield," *Journal of Spacecraft and Rockets*, 2020, pp. 1–10.

[12] Kostak, H. E., Bowersox, R. D., McKiernan, G. R., Thome, J., Candler, G. V., and King, R. A., "Freestream Disturbance Effects on Boundary Layer Instability and Transition on the AFOSR BOLT Geometry," *AIAA Paper*, 2019.

[13] Kostak, H. E., and Bowersox, R. D. W., "Hypersonic boundary layer off-body and surface measurements on the AFOSR BoLT geometry," *AIAA Paper*, 2020, pp. 2020–1043.

[14] Li, F., Choudhari, M., and Paredes, P., "Transition Analysis for Isolated Trips on BOLT-II Wind Tunnel and Flight Configurations," *AIAA AVIATION Forum*, 2021.

[15] Kostak-Teplicek, H. E., "Stability and Breakdown Measurements on the AFRL/AFOSR Boundary Layer Turbulent (BOLT II) Flight Geometry," Ph.D. thesis, Texas A&M University, 2022.

[16] Morkovin, M. V., "On the many faces of transition," *In Viscous Drag Reduction*, 1969, pp. 1–31.

[17] Zhong, X., and Wang, X., "Direct Numerical Simulation on the Receptivity, Instability, and Transition of Hypersonic Boundary Layers," *Annual Review of Fluid Mechanics*, Vol. 44, 2012, pp. 527–561. doi:10.1146/annurev-fluid-120710-101208.

[18] Hader, C., and Fasel, H., "Towards simulating natural transition in hypersonic boundary layers via random inflow disturbances," *J. Fluid Mech.*, Vol. 847, 2018, pp. 2018–386.

[19] McKenzie, J. F., and Westphal, K. O., "Interaction of Linear Waves with Oblique Shock Waves," *The Physics of Fluids*, Vol. 11, 1968, pp. 2350–2362.

[20] Mack, L. M., "Boundary-layer stability theory," *Technical Report 900-277 Rev. A*, 1969.

[21] Fedorov, A., "Transition and stability of high-speed boundary layers," *Annual Review of Fluid Mechanics*, Vol. 43, 2011, pp. 79–95.

[22] Li, F., Choudhari, M., Chang, C.-L., and White, J., "Secondary Instability of Second Mode Disturbances in Hypersonic Boundary Layers," *RTO AVT-200 RSM-030 Specialists' Meeting on Hypersonic Laminar-Turbulent Transition*, 2012.

[23] Saric, W. S., Reed, H. L., and White, E. B., "Stability and transition of three-dimensional boundary layers," *Annual Review of Fluid Mechanics*, Vol. 35, No. 1, 2003, pp. 413–440. doi:10.1146/annurev.fluid.35.101101.161045.

[24] Gronvall, J. E., Johnson, H. B., and Candler, G. V., "Hypersonic three-dimensional boundary layer transition on a cone at angle of attack," *AIAA Paper*, Vol. 3561, 2011.

[25] Choudhari, M., Li, F., and Paredes, P., "Nonlinear Evolution and Breakdown of Azimuthally Compact Crossflow Vortex Pattern over a Yawed Cone," *AIAA Paper*, 2018.

[26] Dinzl, D. J., and Candler, G. V., "Direct simulation of hypersonic crossflow instability on an elliptic cone," *AIAA Journal*, Vol. 55, No. 6, 2017, pp. 1769–1782.

[27] Dinzl, D. J., "Analysis of Stationary Crossflow Instability on HIFiRE-5 Using Direct Numerical Simulation," Ph.D. thesis, University of Minnesota, 2016.

[28] Chen, D. S. C. X. Y. X., J., and Xu, G., "Stationary cross-flow breakdown in a high-speed swept-wing boundary layer," *Physics of Fluids*, Vol. 33, 024108, 2021.

[29] Wassermann, P., and Kloker, M., "Mechanisms and passive control of cross-flow-vortex-induced transition in a three-dimensional boundary layer," *Journal of Fluid Mechanics*, (456):49-84, 2002.

[30] Malik, M. R., Li, F., Choudhari, M. M., and Chang, C.-L., "Secondary instability of crossflow vortices and swept-wing boundary-layer transition," *Journal of Fluid Mechanics*, (399):85-115, 1999.

[31] Chen, X., Dong, S., Tu, G., Yuan, X., and Chen, J., "Boundary layer transition and linear modal instabilities of hypersonic flow over a lifting body," *Journal of Fluid Mechanics*, (938):A8, 2022.

[32] Taira, K., Brunton, S. L., Dawson, S. T., Rowley, C. W., Colonius, T., McKeon, B. J., Schmidt, O. T., Gordeyev, S., Theofilis, V., and Ukeiley, L. S., "Modal Analysis of Fluid Flows: An Overview," *AIAA Journal*, Vol. 55, No. 12, 2017, pp. 4013, 4041.

[33] Taira, K., Hemati, M. S., Brunton, S. L., Sun, Y., Duraisamy, K., Bagheri, S., Dawson, S., and Yeh, C., "Modal Analysis of Fluid Flows: Applications and Outlook," *AIAA Journal*, Vol. 58, No. 3, 2020, pp. 998, 1022.

[34] Jovanovic, M. R., Schmid, P. J., and Nichols, J. W., "Sparsity-Promoting Dynamic Mode Decomposition," *Physics of Fluids*, Vol. 26, No. 2, 2014.

[35] Subbareddy, P., "Stable Low-Dissipation Schemes for Turbulent Compressible Flows," Ph.D. thesis, University of Minnesota, 2007.

[36] MacCormack, R. W., "Numerical Computation of Compressible and Viscous Flow," *American Institute of Aeronautics and Astronautics, Inc.*, 2014.

[37] Candler, G., Subbareddy, P., and Nompelis, I., "CFD methods for hypersonic flows and aerothermodynamics," *Hypersonic Nonequilibrium Flows: Fundamentals and Recent Advances*, 2015, pp. 203–237.

[38] MacCormack, R. W., and Candler, G. V., "The solution of the Navier-Stokes equations using Gauss-Seidel line relaxation," *Computer & Fluids*, 17(1): 135-150, 1989.

[39] MacCormack, R. W., "The Carbuncle CFD Problem," *Journal of Aerospace Information Systems*, Vol. 10, No. 5, 2013.

[40] Van Leer, B., "Towards the ultimate conservative difference scheme. V. a second-order sequel to Godunov's method," *Journal of Computational Physics*, 32(1):101-136, 1979.

[41] Yee, H. C., "A class of high resolution explicit and implicit shock-capturing methods," *Technical Report TM-101088, NASA*, 1989.

[42] Roe, P. L., "Characteristic-based schemes for the euler equations," *Annual review of fluid mechanics*, 18(1):337-365, 1986.

[43] Sweby, P. K., "High resolution schemes using flux limiters for hyperbolic conservation laws," *SIAM journal on numerical analysis*, 21(5):995-1011, 1984.

[44] Subbareddy, P. K., and Candler, G. V., "A fully discrete, kinetic energy consistent finite-volume scheme for compressible flows," *Journal of Computational Physics*, Vol. 228, No. 5, 2009, pp. 1347–1364.

[45] Subbareddy, P. K., Bartkowicz, M. D., and Candler, G. V., "Direct numerical simulation of high-speed transition due to an isolated roughness element," *Journal of Fluid Mechanics*, Vol. 748, 2014, pp. 848–878.

[46] Bartkowicz, M. D., "Numerical Simulations of Hypersonic Boundary Layer Transition," Ph.D. thesis, University of Minnesota, 2012.

[47] Subbareddy, P., and Candler, G., "DNS of Transition to Turbulence in a Mach 6 Boundary Layer," *AIAA 2012-3106*, 2012.

[48] Kovasznay, L. S. G., "Turbulence in supersonic flow," *Journal of the Aeronautical Sciences*, Vol. 20, No. 10, 1953, pp. 657–682.

[49] Harten, A., "The artificial compression method for computation of shocks and contact discontinuities: III. self-adjusting hybrid schemes," *Mathematics of Computation*, 32(142): 363-389. 1978.

[50] Jameson, A., Schmidt, W., and Turkel, E., "Numerical solution of the Euler equations by finite volume methods using Runge Kutta time stepping schemes," *AIAA-81-1259*, 1981.

[51] Pirozzoli, S., "Numerical methods for high-speed flows," *Annual Review of Fluid Mechanics*, 43:163-194, 2011.

[52] Ducros, F., Ferrand, V., Nicoud, F., Weber, C., Darracq, D., Gacherieu, C., and Poinsot, T., "Large-eddy simulation of the shock/turbulence interaction," *Journal of Computational Physics*, 152(2):517-549, 1999.

[53] Larsson, J., Vicquelin, R., and Bermejo-Moreno, I., "Large eddy simulations of the HyShot II scramjet," *Center for Turbulence Research Annual Briefs*, 2011.

[54] Quinlan, J., McDaniel, J., and Baurle, R., "Simulation of a Wall-Bounded Flow using a Hybrid LES/RAS Approach with Turbulence Recycling," *AIAA Paper 2012-3285*, 2012.

[55] Knutson, A., GS, S., and Candler, G., "Direct numerical simulation of Mach 6 flow over a cone with a highly swept fin," *AIAA Paper 2018-0379*, 2018.

[56] Hendrickson, T., Kartha, A., and Candler, G., "An Improved Ducros Sensor for the Simulation of Compressible Flows with Shocks," *AIAA Paper 2018-3710*, 2018.

[57] AMROCexamples, *http://amroc.sourceforge.net/examples/euler/2d/html/shbubble$_n$.htm*, 2004.

[58] Kurganov, A., and Tadmor, E., "Solution of two-dimensional Riemann problems for gas dynamics without Riemann problem solvers," *Numer. Methods Partial Differential Eq.*, (18): 584-608. 2002. https://doi.org/10.1002/num.10025.

[59] Schwing, A. M., "Parallel Adaptive Mesh Refinement for High-Order Finite-Volume Schemes in Computational Fluid Dynamics," Ph.D. thesis, University of Minnesota, 2015.

[60] Knutson, A. L., Johnson, H. B., and Candler, G. V., "Adaptive Mesh Refinement in US3D," *AIAA Paper 2021-1783*, 2021.

[61] Drayna, T. W., "Design and Optimization of Hypersonic Inward-Turning Inlets," Ph.D. thesis, University of Minnesota, 2011.

[62] Candler, G. V., "The computation of weakly ionized hypersonic flows in thermo-chemical nonequilibrium," Ph.D. thesis, Stanford University, 1988.

[63] Candler, G. V., "Computation of hypersonic low-density flows with thermochemical nonequilibrium," Ph.D. thesis, Stanford University, 1990.

[64] Wright, M. J., Candler, G. V., and Prampolini, M., "Data-parallel lower-upper relaxation method for the Navier-Stokes equations," *AIAA Journal*, 34(7): 1371-1377, 1996.

[65] Wright, M. J., Candler, G. V., and Bose, D., "Data-parallel line relaxation method for the Navier-Stokes equations," *AIAA Journal*, 36(9): 1603-1609, 1998.

[66] Wright, M. J., "A family of data-parallel relaxation methods for the Navier-Stokes equations," Ph.D. thesis, Stanford University, 1997.

[67] Pulliam, T., "Time accuracy and the use of implicit methods," *NASA*, 2004.

[68] Howard, M. A., "Finite element modeling and optimization of high-speed aerothermoelastic systems," Ph.D. thesis, University of Colorado, Boulder, 2010.

[69] Knutson, A. L., "Numerical Simulation of Instabilities in Three-Dimensional Hypervelocity Boundary Layers," Ph.D. thesis, University of Minnesota, 2020.

[70] Thome, J., Reinert, J., and Candler, G., "Effect of steady forcing mechanisms on BoLT geometry for flight conditions," *AIAA Paper*, 2020-1042, 2020.

[71] Reinert, J. D., "Conjugate Heat Transfer Simulations for Hypersonic Vehicles," Ph.D. thesis, University of Minnesota, 2020.

[72] Melander, L. J., Dwivedi, A., and Candler, G. V., "Nose Bluntness Effects on the Amplification of External Disturbances in Hypersonic Flows," *AIAA Paper*, 2022-0948, 2022.

[73] Bushnell, D., "Notes on initial disturbance fileds for the transition problem," *Instability and transition*, 1990.

[74] Browne, O. M., Al Hasnine, S. M., Russo, V., and Brehm, C., "Fully-Resolved Particulate-Induced Transition for High-Speed Boundary-Layers with an Immersed Boundary Method," *AIAA Paper*, 2020-1795, 2020.

[75] Habeck, J. B., Hogan, C. J., Flaten, J. A., and Candler, G. V., "Development of a calibration system for measuring aerosol particles in the stratosphere," *AIAA Paper*, 2022-1582, 2022.

[76] Liu, Y., Schuabb, M., Duan, L., Paredes, P., and Choudhari, M. M., "Interaction of a Tunnel-like Acoustic Disturbance Field with a Blunt Cone Boundary Layer at Mach 8," *AIAA AVIATION Paper*, 2022-3250, 2022.

[77] Tufts, M. W., Borg, M. P., Bisek, J., Nicholas, and Kimmel, R. L., "High-Fidelity Simulation of HIFiRE-5 Boundary-Layer Transition," *AIAA AVIATION Paper*, 2020-3025, 2020.

[78] Hader, C., and Fasel, H. F., "Direct Numerical Simulations of Hypersonic Boundary-Layer Transition for a Flared Cone: Fundamental Breakdown," *Journal of Fluid Mechanics*, Vol. 869, 2019, pp. 341–384.

[79] Johnson, H. B., Seipp, T. G., and Candler, G. V., "Numerical study of hypersonic reacting boundary layer transition on cones," *Physics of Fluids*, Vol. 10, 1998, pp. 2676–2685.

[80] Melander, L. J., and Candler, G. V., "Investigation of Atmospheric Turbulence and Shock Interaction for a Hypersonic Sphere-Cone," *AIAA Scitech Paper*, 2021-1325, 2021.

[81] Schmid, P., "Dynamic Mode Decomposition of Numerical and Experimental Data," *Journal of Fluid Mechanics*, Vol. 656, 2010.

[82] Tu, J. H., Rowley, C. W., Luchtenburg, D. M., Brunton, S. L., and Kutz, J. N., "On Dynamic Mode Decomposition: Theory and Applications," *Journal of Computational Dynamics*, Vol. 1, No. 2, 2014, pp. 391–421.

[83] Hemati, M. S., Williams, M. O., and Rowley, C. W., "Dynamic mode decomposition for large and streaming datasets," *Physics of Fluids 26, 111701*, 2014.

[84] Hemati, M., Deem, E., Williams, M., Rowley, C., and Cattafesta, L., "Improving Separation Control with Noise-Robust Variants of Dynamic Mode Decomposition," *AIAA Paper 2016-1103*, 2016.

[85] Hemati, M. S., Rowley, C. W., Deem, E. A., and Cattafesta, L. N., "De-Biasing the Dynamic Mode Decomposition for Applied Koopman Spectral Analysis of Noisy Datasets," *Theoretical and Computational Fluid Dynamics*, Vol. 31, No. 4, 2017, pp. 349, 368.

[86] DMDTools, *http://z.umn.edu/dmdtools/*, 2015.

[87] Chu, B.-T., "On the Energy Transfer to Small Disturbances in Fluid Flow (Part I)," *Acta Mechanica*, Vol. 1, No. 3, 1965.

[88] Dwivedi, A., "Global input-output analysis of flow instabilities in high-speed compressible flows," Ph.D. thesis, University of Minnesota, 2020.

[89] Hoffman, W., "Iterative algorithms for Gram-Schmidt orthogonalization," *Computing*, 41, 335–348 (1989).

[90] Lumley, J. L., "Stochastic tools in turbulence," *Courier Corporation*, 2007.

[91] Towne, A., Schmidt, O. T., and Colonius, T., "Spectral proper orthogonal decomposition and its relationship to dynamic mode decomposition and resolvent analysis," *J. Fluid Mech.*, Vol. 847, 2018.

[92] Schmidt, O. T., and Colonius, T., "Guide to Spectral Proper Orthogonal Decomposition," *AIAA Journal*, Vol. 847, No. 3, 2020.

[93] Schmidt, O., *https://github.com/SpectralPOD/spod$_m$atlab*, 2019.

[94] Thome, J., Knutson, A., and Candler, G. V., "Boundary layer instabilities on BoLT subscale geometry," *AIAA Paper 2019-0092*, 2019.

[95] Johnston, Z. M., and Candler, G. V., "Hypersonic simulations of the BoLT-2 subscale geometry," *AIAA Scitech Paper*, 2021-0366, 2021.

[96] Huntley, M. B., "Transition on Elliptic Cones at Mach 8," Ph.D. thesis, Princeton University, 2000.

[97] Smits, A. J., and Dussauge, J.-P., "Turbulent Shear Layers in Supersonic Flow," *Springer,New York*, 2006.

[98] Hunt, J. C. R., Wray, A. A., and Moin, P., "Eddies, Streams, and Convergence Zones in Turbulent Flows," *Center for Turbulence Research Paper CTR-S88*, 1988, pp. 193–208.

[99] Chong, M. S., Perry, A. E., and Cantwell, B. J., "A general classification of three-dimensional flow fields," *Physics of Fluids A: Fluid Dynamics 2*, 765 (1990); doi: 10.1063/1.857730.

[100] Kolár, V., "Vortex identification: New requirements and limitations," *The Physics of Fluids*, Vol. 28, 2007, pp. 638–652.

[101] Hanifi, A., Schmid, P., and Henningson, D., "Transient growth in compressible boundary layer flow," *Physics of Fluids*, Vol. 8, No. 3, 1996.

[102] George, K. J., and Sujith, R. I., "On Chu's disturbance energy," *Journal of Sound and Vibration*, Vol. 330, 2011.

[103] Shrestha, P., and Candler, G., "Direct Numerical Simulation of Trip Induced Transition," *AIAA AVIATION*, 2016.

[104] Mullen, D., and Reed, H. L., "Analyis of the BOLT II - Holden Mission Flight and Wind Tunnel Geometries," *AIAA Paper 2021-0852*, 2021.

[105] Cook, D. A., and Nichols, J. W., "Free-stream receptivity of a hypersonic blunt cone using input–output analysis and a shock-kinematic boundary condition," *Theoretical and Computational Fluid Dynamics*, Vol. 36, 2022.

[106] Pirozzoli, S., and Orlandi, P., "Natural grid stretching for DNS of wall-bounded flow," *Journal of Computational Physics*, Vol. 439, 2021.

[107] Bitter, N., and Shepherd, J., "Transient Growth in Hypersonic Boundary Layers," *7th AIAA Theoretical Fluid Mechanics Conference*, 2014.

[108] Landahl, M., "Dynamics of boundary layer turbulence and the mechanism of drag reduction," *Physics of Fluids*, Vol. 20, No. 10, 1977.

[109] Dwivedi, S. G. S. N. J. W. C. G. V., A., and Jovanovic, M. R., "Reattachment streaks in hypersonic compression ramp flow: an input-output analysis," *J. Fluid Mech.*, Vol. 880, 2019.

[110] Stetson, K. F., "Hypersonic Boundary-Layer Transition," *Advances in Hypersonics*, Springer, New York, pp. 324-417, 1992.

[111] Johnston, Z. M., Hemati, M. S., and Candler, G. V., "Modal Analysis of Instabilities in the BoLT-2 Flowfield," *AIAA Scitech Paper*, 2022-0348, 2022.

[112] Henderson, R., "Details of the drag curve near the onset of vortex shedding," *Physics of Fluids*, Vol. 7, No. 9, 1995.